INSTITUTE FOR THEORETICAL PHYSICS

MASTER'S THESIS

Tight-binding theory of spin-orbit coupling in graphynes

Author:
Guido van Miert

Supervisors:
Prof. Dr. Cristiane Morais Smith
Dr. Vladimir Juričić

August 7, 2014

ABSTRACT

Graphynes represent an emerging family of two-dimensional carbon allotropes that recently attracted much interest due to the tunability of the Dirac cones in the band structure. We explore the effects of spin-orbit couplings, both Rashba and intrinsic ones, in these systems. First, we develop a general method to address spin-orbit couplings within tight-binding theory. We then apply this method to describe the effects of spin-orbit couplings in α, β, and γ-graphyne. We show how spin-orbit couplings can lead to various effects related to both topological and non-topological properties of their band structures. In α-graphyne, as in graphene, the Rashba spin-orbit coupling splits each Dirac cone into four, whereas the intrinsic spin-orbit coupling opens a topological gap. In β-graphyne, intrinsic spin-orbit coupling yields high- and tunable Chern-number bands, which may host both topological and Chern insulators, in the presence and absence of time-reversal symmetry, respectively. On the other hand, Rashba spin-orbit coupling can be used to control the position and the number of Dirac cones in the Brillouin zone. Finally, the Rashba spin-orbit coupling can close the band gap in γ-graphyne.

CONTENTS

1. INTRODUCTION

During the last decade, graphene has attracted enormous attention, and has provided a new paradigm for studying pseudo-relativistic fermions in condensed-matter systems [1]. The peculiar Dirac-like structure of its low-energy quasiparticles arises due to the lattice and time-reversal symmetries. The honeycomb lattice, see Fig. 1.1(a), which consists of two equivalent interpenetrating triangular lattices, gives rise to the touching of the valence and conduction bands at two inequivalent K and K' points at the corners of the hexagonal Brillouin zone (BZ), which are related by time-reversal symmetry. Furthermore, graphene is a platform for the first proposed time-reversal invariant topological insulator [2]. However, this proposal has not been realized experimentally due to a weak spin-orbit coupling (SOC). Since then, achieving strong SOC in Dirac materials has been one of the goals that motivated the search for alternatives to graphene. Promising candidates for realizing strong SOC in Dirac materials have been recently proposed. Those include self-assembled honeycomb arrays of PbSe semiconducting nanocrystals [3], as well as patterned quantum dots [4] and molecular graphene [5]. Yet another interesting class of Dirac materials in this respect consists of graphynes. Graphynes represent a class of two-dimensional carbon allotropes, which differ from graphene by the presence of triple bonds ($-$C $\equiv$ C$-$) into their lattice structure. Figs. 1.1(b), (c), and (d) display the lattice structure of α, β, and γ graphyne, respectively. They were first introduced by Baughman in 1987 [6], and since then their structural, electronic, and mechanical properties have been extensively studied [7, 8, 9, 10, 11]. They have not been synthesized yet, in contrast to the structurally similar graphdiyne, which has been recently fabricated, see also Fig. 1.2[12]. Graphynes have recently attracted much interest, especially
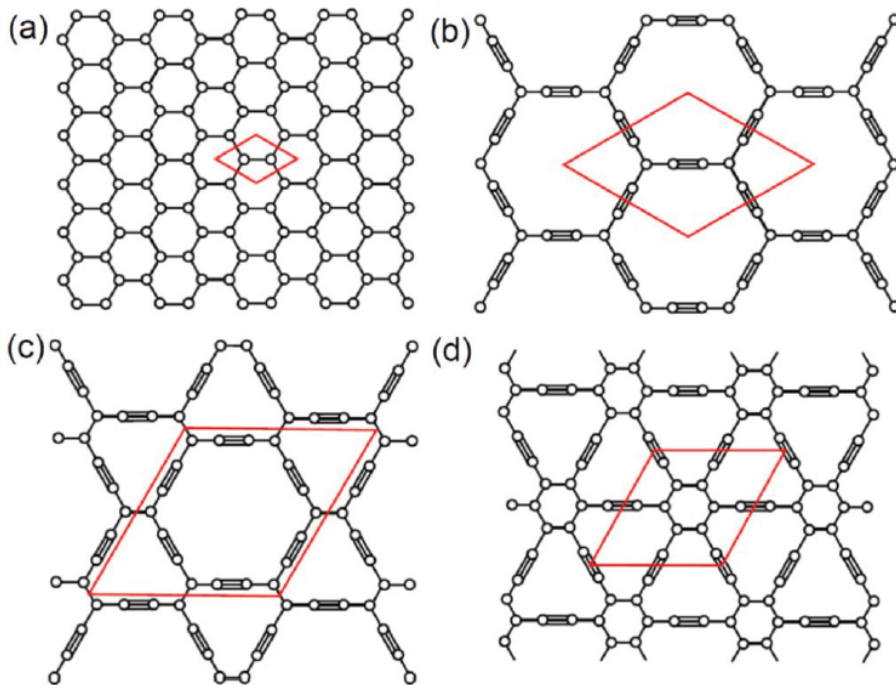

Fig. 1.1: Lattice structure of graphene, α, β, and γ-graphyne. Figure extracted from Ref. [16].
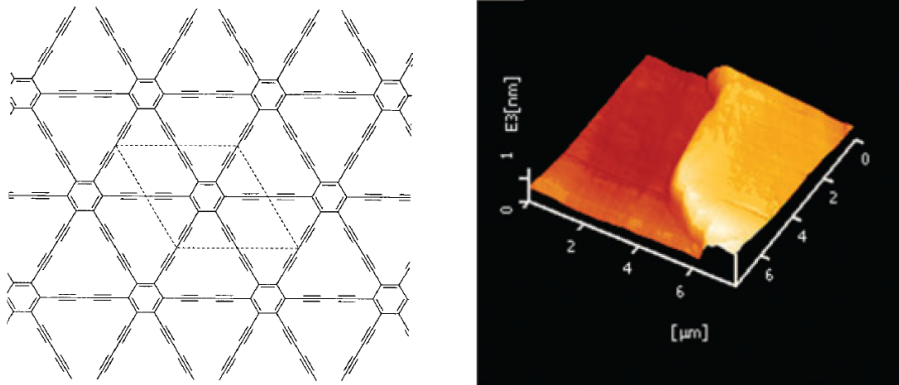
Fig. 1.2: Left: Lattice structure of graphdiyne, figure extracted from Ref. [7]. Right: Image of graphdiyne film obtained via atomic force microscopy; extracted from Ref. [12].

because they exhibit Dirac-like properties. In particular, it has been shown by using *ab initio* and tight-binding (TB) methods [13] that α graphyne features Dirac cones at the high-symmetry K and K' points of the BZ, whereas in β graphyne they occur along the high-symmetry $\Gamma - M$ line. On the other hand, γ graphyne is gapped. A criterion for the existence of the Dirac cones has been provided within simple TB models [14]. Furthermore, the possibility of manipulation of the Dirac cones by chemical reactions has been discussed [15]. The control of the electronic properties with adatoms has been considered in Refs. [16, 17, 18, 19, 20], which is particularly important in light of inducing topological properties in graphyne-based electronic band structures. However, this family of carbon allotropes has not only been praised for its electronic or topological properties. For example, due to presence of variously sized pores they may also be used to separate gases. Along the same lines, it is shown using simulations that graphynes may serve as the ultimate membrane to remove salt ions from water. A few other applications include the ability of graphynes to store H_2 or to use them in Li ion batteries [21].

Topologically nontrivial properties of a material, from a practical perspective, critically depend on the strength of the spin-orbit interaction. On the other hand, graphynes are based on carbon and, as such, are expected to feature a weak SOC, as it is the case in graphene, for instance. The effect of intrinsic SOC in these systems has been recently investigated using *ab initio* methods [33]. Furthermore, the above-mentioned possibility of controlling the electronic properties of graphynes with adatoms puts forward a way of manipulating SOC in these systems by using adatoms of heavy elements, such as Bi and Sn, for instance. Before doing so, however, a general framework for addressing SOC in graphynes has to be developed. This is precisely the aim of this thesis.

This thesis is organized as follows. In Chapter 2 we discuss the properties of graphene and along the way introduce some rather basic concepts in condensed matter physics that will be used in this thesis. Then, in Chapter 3 we introduce α, β, and γ-graphyne and show how their low-energy properties can be studied using TB theory. Moreover, we briefly review how one is able to obtain a simpler description of these graphynes by an effective theory. In Chapter 4 we consider SOC, and provide a method to implement SOC in a TB model. Subsequently, we consider in Chapter 5 the effects of SOC on the electronic band structure in graphynes. Specifically, we show how Rashba SOC can lead to various Lifshitz transitions, whereas the intrinsic SOC leads to non-trivial topological properties of the electron bands in graphynes. We provide our conclusions in Chapter 6.

2. PRELIMINARIES: GRAPHENE

In this chapter we study some basic properties of graphene. First of all, we show how we may obtain the band structure using TB theory. It turns out that in graphene the low-energy quasi-particles are effectively described as massless Dirac Fermions. However, if one breaks time-reversal or inversion symmetry a gap is generated, which acts as a mass for relativistic Dirac particles. Finally, we shortly discuss how SOC can transform graphene into a topological insulator.

2.1 Lattice structure

Graphene is a two-dimensional carbon allotrope where the atoms are arranged in a honeycomb lattice. Before we address this honeycomb geometry from a mathematical point of view, we first would like to understand how this particular geometry arises. Carbon, being a member of group fourteen in the periodic table, has four valence electrons. These four valence electrons all reside in the second shell, which hosts one s orbital and three p-orbitals. These latter can be further distinguished as being p_x, p_y, or p_z orbitals, see also Fig. 2.1. The s, p_x, and p_y orbitals form now three in plane directed sp^2 hybrid orbitals that have mutual angles of 120 degrees. Each of the bonds in graphene is formed by the overlap between two of these hybrid orbitals, see Fig. 2.2. In graphene these sp^2 hybrid orbitals form very strong bonds, which are responsible for the honeycomb geometry. The remaining p_z-orbitals give rise to the electronic properties of graphene. Throughout this thesis we will be mainly concerned with the p_z-orbitals and assume the geometry due to the s, p_x, and p_y orbitals as given.

We now move on to describe the honeycomb geometry mathematically. The simplest ordered patterns correspond to Bravais lattices. In two dimensions a Bravais lattice is defined as the set of points L generated by two lattice vectors $\mathbf{a}_1$ and $\mathbf{a}_2$

$$\mathbf{L} = n_1 \mathbf{a}_1 + n_2 \mathbf{a}_2, \tag{2.1}$$

with n_1 and n_2 are both integers. However, it can easily be seen that the honeycomb lattice of graphene does not correspond to a Bravais lattice, but it is actually the union of two Bravais lattices. To see this we need to distinguish between the carbon atoms based on the positions of their nearest-neighbor (NN) carbon atoms. To a carbon atom that has NN located to the right (left), upper left (right), and lower left (right), we assign the type A (B), see also Fig. 2.3. The positions of the carbon atoms of one
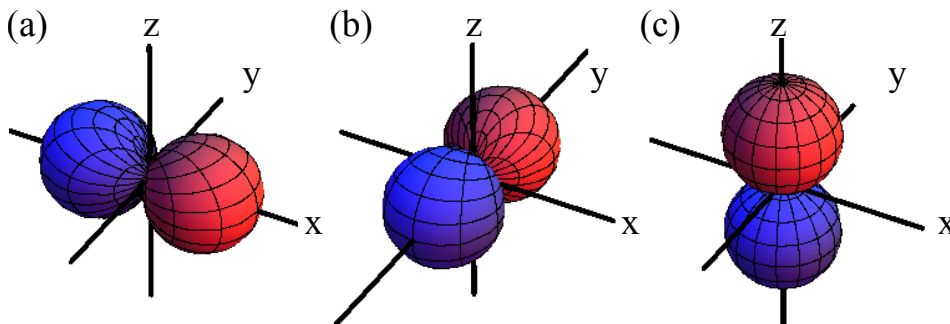

Fig. 2.1: Visualization of the p_x, p_y, and p_z-orbitals, shown in panels (a), (b), and (c) respectively. In this figure the blue(red) part corresponds to positive (negative) value of the wave function.
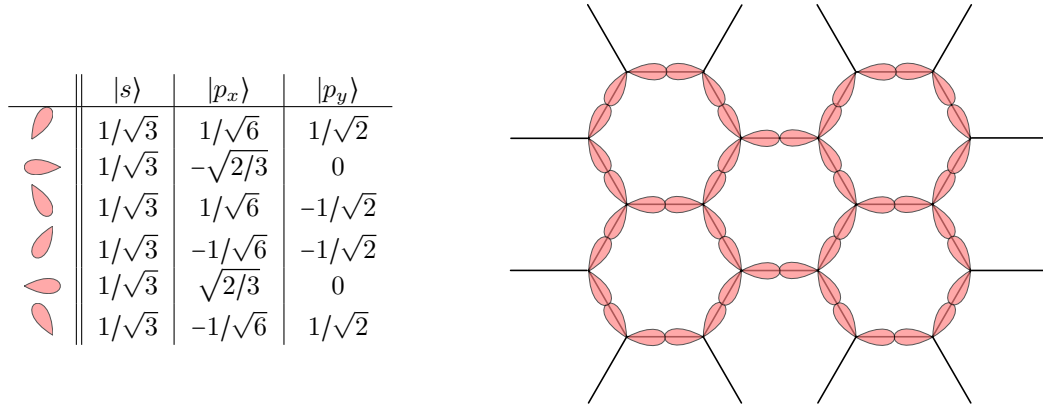
	$\lvert s \rangle$	$\lvert p_x \rangle$	$\lvert p_y \rangle$
	$1/\sqrt{3}$	$1/\sqrt{6}$	$1/\sqrt{2}$
	$1/\sqrt{3}$	$-\sqrt{2/3}$	0
	$1/\sqrt{3}$	$1/\sqrt{6}$	$-1/\sqrt{2}$
	$1/\sqrt{3}$	$-1/\sqrt{6}$	$-1/\sqrt{2}$
	$1/\sqrt{3}$	$\sqrt{2/3}$	0
	$1/\sqrt{3}$	$-1/\sqrt{6}$	$1/\sqrt{2}$

Fig. 2.2: Left: Decomposition of sp^2 hybrid orbitals, shown in red, in terms of p_x, p_y, and s orbitals.; Right: Schematic picture of the bonding due to the sp^2 hybrid orbitals.

type correspond to a triangular Bravais lattice with lattice vectors given by

$$\mathbf{a}_1 = \frac{a}{2}\left(3, \sqrt{3}\right),$$
$$\mathbf{a}_2 = \frac{a}{2}\left(3, -\sqrt{3}\right), \tag{2.2}$$

with $a = 1.42$ Å the NN distance[1]. Hence, the positions of the carbon atoms of type A and B can be described by the Bravais lattices L_A and L_B, which are given by

$$L_A = n_1\mathbf{a}_1 + n_2\mathbf{a}_2, \tag{2.3}$$
$$L_B = n_1\mathbf{a}_1 + n_2\mathbf{a}_2 + (a, 0), \tag{2.4}$$

with n_1, $n_2 \in \mathbb{Z}$. In other words, a honeycomb lattice can be seen as a triangular Bravais lattice with a two-atom basis. For future use, we also define the NN vectors δ_i

$$\delta_1 = \frac{a}{2}(-1, -\sqrt{3}), \quad \delta_2 = \frac{a}{2}(-1, \sqrt{3}), \text{ and } \delta_3 = a(1, 0). \tag{2.5}$$

Next, we introduce the reciprocal lattice R. This is defined as

$$R = n_1\mathbf{b}_1 + n_2\mathbf{b}_2, \tag{2.6}$$

such that $\mathbf{b}_1$ and $\mathbf{b}_2$ satisfy

$$\mathbf{a}_i \cdot \mathbf{b}_j = 2\pi\delta_{i,j}. \tag{2.7}$$

It is an easy exercise to show that for graphene the reciprocal lattice vectors are given by

$$\mathbf{b}_1 = \frac{2\pi}{3a}\left(1, \sqrt{3}\right), \quad \mathbf{b}_2 = \frac{2\pi}{3a}\left(1, -\sqrt{3}\right). \tag{2.8}$$

This reciprocal lattice may be used to define a primitive cell in momentum space that consists of inequivalent wave vectors. In principle such a primitive cell is not uniquely defined. However, throughout this thesis we take this primitive cell equal to the first BZ. The first BZ is defined as the set of points in momentum space that are closer to the origin than to any of the other points in the reciprocal lattice. Note that, the first BZ together with the lattice translations generate the whole plane. In Fig. 2.3 we have depicted the first BZ for graphene. Commonly one refers to the corners of the BZ as the K and K' points, the center of the BZ is called the Γ point, and the point in between the two corners of the BZ is denoted as the M point.
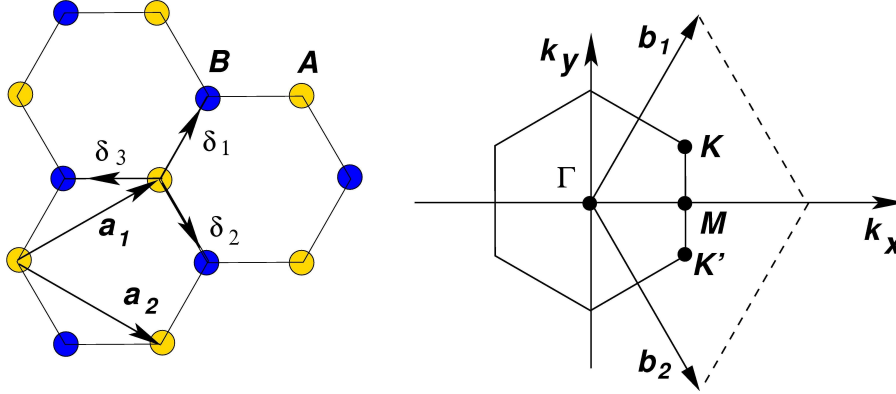
Fig. 2.3: Left: Honeycomb lattice; Right: BZ for graphene. Figure extracted from Ref.[1].

2.2   Bloch's theorem

A crystal is by definition periodic in space. As a result, the Hamiltonian H describing the electrons is invariant under translations by multiples of the lattice vector $\mathbf{a}_i$. This implies that the commutator between the Hamiltonian H and the translation operators $T_{\mathbf{a}_i}$ vanishes. Bloch's theorem then guarantees that the eigenstates $\Psi(\mathbf{r})$ of the Hamiltonian can be written as the product of a periodic function and a plane wave labeled by a so-called crystal momentum $\mathbf{k}$

$$\Psi(\mathbf{r}) = e^{i\mathbf{k}\cdot\mathbf{r}}u(\mathbf{r}). \tag{2.9}$$

Here the function u satisfies the condition

$$u(\mathbf{r} + \mathbf{a}_i) = u(\mathbf{r}), \tag{2.10}$$

for all lattice vectors $\mathbf{a}_i$. For completeness we will prove this result. From the condition $[H, T_{\mathbf{a}_i}] = 0$ we infer that one may impose

$$H\Psi(\mathbf{r}) = E\Psi(\mathbf{r}), \tag{2.11}$$

and

$$T_{\mathbf{a}_i}\Psi(\mathbf{r}) \coloneqq \Psi(\mathbf{r} + \mathbf{a}_i) = e^{i2\pi\theta_i}\Psi(\mathbf{r}), \tag{2.12}$$

where $\theta_i \in [0, 1)$. Next, we define the crystal momentum $\mathbf{k} \coloneqq \sum_i \theta_i \mathbf{b}_i$ with $\mathbf{b}_i$ the reciprocal lattice vectors defined in section 2.1. By writing $\Psi(\mathbf{r}) = e^{i\mathbf{k}\cdot\mathbf{r}}u(\mathbf{r})$ we obtain

$$\begin{aligned}
u(\mathbf{r} + \mathbf{a}_i) &= e^{-i\mathbf{k}\cdot(\mathbf{r}+\mathbf{a}_i)}\Psi(\mathbf{r} + \mathbf{a}_i) \\
&= e^{-2\pi i\theta_i}e^{-i\mathbf{k}\cdot\mathbf{r}}e^{i2\pi\theta_i}\Psi(\mathbf{r}) \\
&= e^{-i\mathbf{k}\cdot\mathbf{r}}\Psi(\mathbf{r}) = u(\mathbf{r}).
\end{aligned} \tag{2.13}$$

Hence, we have proved Bloch's theorem. It is important to note that the decomposition into a planar wave $e^{i\mathbf{k}\cdot\mathbf{r}}$ and a periodic function $u(\mathbf{r})$ is not unique

$$\begin{aligned}
e^{i\mathbf{k}\cdot\mathbf{r}}u(\mathbf{r}) &= e^{i(\mathbf{k}+\sum_j n_j\mathbf{b}_j)\cdot\mathbf{r}}e^{-i\sum_j n_j\mathbf{b}_j\cdot\mathbf{r}}u(\mathbf{r}) \\
&= e^{i\tilde{\mathbf{k}}\cdot\mathbf{r}}\tilde{u}(\mathbf{r}),
\end{aligned} \tag{2.14}$$

where we have redefined the crystal momentum $\tilde{\mathbf{k}} = \mathbf{k} + \sum_j n_j \mathbf{b}_j$ and the periodic function $\tilde{u}(\mathbf{r}) = e^{-i\sum_j n_j \mathbf{b}_j \cdot \mathbf{r}} u(\mathbf{r})$. This result allows one to shift the crystal momentum by integer multiples of the reciprocal lattice vectors such that it is an element of the first BZ. However, states corresponding to crystal momenta in the first BZ are orthogonal to each other.

Given a lattice one can easily give examples of Bloch waves. For example, in graphene we can construct a Bloch wave corresponding to the p_z orbitals. Suppose that the atomic p_z orbital is described by the wave function $\phi(\mathbf{r})$, then for each crystal momentum $\mathbf{k}$ we may define the wave functions

$$\Psi_{\mathbf{k}}^A(\mathbf{r}) = \sum_i e^{i\mathbf{k}\cdot R_i} \phi(\mathbf{r} - \mathbf{R}_i) \text{ and} \tag{2.15}$$

$$\Psi_{\mathbf{k}}^B(\mathbf{r}) = \sum_i e^{i\mathbf{k}\cdot(\mathbf{R}_i + \delta_1)} \phi(\mathbf{r} - (\mathbf{R}_i + \delta_1)), \tag{2.16}$$

here $\mathbf{R}_i$ denotes all the different lattice sites $n_1 \mathbf{a}_1 + n_2 \mathbf{a}_2$, with $n_1, n_2 \in \mathbb{Z}$. It is an easy exercise to show that the defined wave functions are indeed Bloch waves. For $\mathbf{r}$ close to a lattice site $\mathbf{R}_j$ the Bloch wave $\Psi_{\mathbf{k}}^A(\mathbf{r})$ is very similar to the atomic orbital located at that site. Suppose $\|\mathbf{r} - \mathbf{R}_j\| \ll a$, the NN distance, then we obtain

$$\Psi_{\mathbf{k}}^A(\mathbf{r}) = \sum_{i \neq j} \left[e^{i\mathbf{k}\cdot\mathbf{R}_i} \phi(\mathbf{r} - \mathbf{R}_i) + e^{i\mathbf{k}\cdot\mathbf{R}_j} \phi(\mathbf{r} - \mathbf{R}_j) \right]$$

$$\approx e^{i\mathbf{k}\cdot\mathbf{R}_j} \phi(\mathbf{r} - \mathbf{R}_j). \tag{2.17}$$

In the second line we used that the atomic orbital goes rapidly to zero away from the origin. We may also consider the Fourier transformation of the Bloch wave $\Psi_k^A(r)$. This yields

$$\int \mathrm{d}k e^{i\mathbf{k}\cdot\mathbf{R}_j} \Psi_{\mathbf{k}}^A(\mathbf{r}) = \sum_i \int \mathrm{d}k e^{i\mathbf{k}\cdot(\mathbf{R}_i - \mathbf{R}_j)} \phi(\mathbf{r} - \mathbf{R}_i)$$

$$= \sum_i \delta_{i,j} \phi(\mathbf{r} - \mathbf{R}_i)$$

$$= \phi(\mathbf{r} - \mathbf{R}_j). \tag{2.18}$$

In this way we are able to write down wave functions that satisfy the criteria for Bloch's theorem; however, we still do not know anything about the band structure. To proceed we need to introduce TB theory.

2.3 Tight-binding theory

Given a lattice system, one ultimately would like to solve the Schrödinger equation. Unfortunately, in most cases one has to resort to an approximation technique because the system is too complicated. Graphene is no exception to that rule, and its Hamiltonian reads

$$H = -\frac{\hbar^2}{2m} \nabla^2 + \sum_i V_{\mathrm{at}}(\mathbf{r} - \mathbf{R}_i) + \sum_i V_{\mathrm{at}}(\mathbf{r} - (\mathbf{R}_i + \delta_1)). \tag{2.19}$$

Here m denotes the electron's mass and $V_{\mathrm{at}}(\mathbf{r})$ is the atomic potential.

For clarity we now discuss in a completely generic setup a way to approximate the Schrödinger equation. Suppose we are given a Hamiltonian H, then the Schrödinger equation reads

$$H|\Psi\rangle = E|\Psi\rangle. \tag{2.20}$$

Next, we consider a projection P that allows us to rewrite the eigenvalue equation as

$$H[P|\Psi\rangle + (1 - P)|\Psi\rangle] = E|\Psi\rangle. \tag{2.21}$$

If for some reason the exact wave function Ψ has very little overlap with the states in the subspace to which $1 - P$ projects, we find $\|(1 - P)|\Psi\rangle\| \approx 0$, which allows us to approximate the eigenvalue equation:

$$HP|\Psi\rangle \approx E|\Psi\rangle. \tag{2.22}$$

By acting on both sides with the operator P this reduces to

$$PHP|\Psi\rangle \approx EP|\Psi\rangle. \tag{2.23}$$

Hence, we may study the system using the Hamiltonian PHP. Note that this method relies on the assumption that one may neglect $(1 - P)|\Psi\rangle$.

TB theory amounts to choosing the operator P such that P projects onto the subspace of Bloch waves composed of atomic orbitals. One can understand this approximation in the following way. Suppose that the lattice constant a is "close" to infinity. Then, due to the atomic potential around each lattice site, the wave function close to each atom should be proportional to the atomic orbital. Hence, the eigenstates then correspond to the Bloch waves obtained from the atomic orbitals. The TB assumption boils down to the fact that one assumes that as one brings the atoms closer together the wave functions are still relatively well approximated by these Bloch waves, which contain relatively few atomic orbitals.

As already pointed out in section 2.1, in graphene the bonds are formed by sp^2 hybrid orbitals, whereas the p_z orbitals govern the physics near the Fermi level. As a consequence, we may take P such that it projects onto the space spanned by the p_z-orbitals. Since the Hamiltonian H is invariant under reflection in the $x - y$ plane, one may always impose that the wave function is either symmetric or antisymmetric in the $\hat{z}$ direction. The p_z orbitals are odd under this symmetry and as such do not mix with the even s, p_x, and p_y orbitals. These considerations motivate the following definition

$$\begin{aligned} P &= \int_{BZ} dk \left[|\Psi_\mathbf{k}^A\rangle\langle\Psi_\mathbf{k}^A| + |\Psi_\mathbf{k}^B\rangle\langle\Psi_\mathbf{k}^B| \right] \\ &= \sum_i \left[|a_i\rangle\langle a_i| + |b_i\rangle\langle b_i| \right] \end{aligned} \tag{2.24}$$

where we used Eq. (2.18) in the second line. Note that this operator is only a projection if the following conditions hold

1. $\langle a_i|a_j\rangle = \delta_{i,j}$ for all i,

2. $\langle b_i|b_j\rangle = \delta_{i,j}$ for all i,

3. and $\langle a_i|b_j\rangle = \langle b_i|a_j\rangle$ for all i and j.

Throughout this thesis we assume these conditions to hold. As a result the effective Hamiltonian reads

$$PHP = \sum_{i,j} |a_i\rangle\langle a_i|H|a_j\rangle\langle a_j| + |a_i\rangle\langle a_i|H|b_j\rangle\langle b_j| + |b_i\rangle\langle b_i|H|a_j\rangle\langle a_j| + |b_i\rangle\langle b_i|H|b_j\rangle\langle b_j|. \tag{2.25}$$

Next, we need to compute the matrix elements like $\langle a_i|H|b_j\rangle$. We may write the Hamiltonian H as

$$\begin{aligned} H &= -\frac{\hbar^2}{2m}\nabla^2 + V_{\text{at}}(\mathbf{r} - \mathbf{R}_i) + \Delta V(\mathbf{r}) \\ &= H_i^A + \Delta V(\mathbf{r}) \end{aligned} \tag{2.26}$$

or as

$$\begin{aligned} H &= -\frac{\hbar^2}{2m}\nabla^2 + V_{\text{at}}(\mathbf{r} - (\mathbf{R}_i + \delta_1)) + \Delta V(\mathbf{r}) \\ &= H_i^B + \Delta V(\mathbf{r}). \end{aligned} \tag{2.27}$$

Since $|a_i\rangle$ and $|b_i\rangle$ are both atomic orbitals, they satisfy $H_i^A|a_i\rangle = \varepsilon_p|a_i\rangle$ and $H_i^B|b_i\rangle = \varepsilon_p|b_i\rangle$. This allows us to express the matrix elements as

$$
\begin{aligned}
\langle a_i|H|a_j\rangle &= \langle b_i|H|b_j\rangle \\
&= \varepsilon_p \delta_{i,j} + \int \mathrm{d}\mathbf{r}\phi(\mathbf{r} - \mathbf{R}_i)\Delta V(\mathbf{r})\phi(\mathbf{r} - \mathbf{R}_j)
\end{aligned}
\tag{2.28}
$$

and similarly we find

$$
\begin{aligned}
\langle a_i|H|b_j\rangle &= \langle b_i|H|a_j\rangle \\
&= \int \mathrm{d}\mathbf{r}\phi(\mathbf{r} - \mathbf{R}_i)\Delta V(\mathbf{r})\phi(\mathbf{r} - (\mathbf{R}_j + \delta_1)).
\end{aligned}
\tag{2.29}
$$

Throughout this thesis we make the approximation that only $\int \mathrm{d}\mathbf{r}\phi(\mathbf{r} - \mathbf{R}_i)\Delta V(\mathbf{r})\phi(\mathbf{r} - (\mathbf{R}_j + \delta_1))$ is non-zero if a_i and b_j are NN. As a result, the Hamiltonian reduces to

$$
PHP = \varepsilon_p \sum_i (|a_i\rangle\langle a_i| + |b_i\rangle\langle b_i|) + t \sum_{\langle i,j\rangle} (|a_i\rangle\langle b_j| + |b_i\rangle\langle a_j|),
\tag{2.30}
$$

where we defined t the NN hopping parameter. In graphene the value of this parameter is $t = 2.8\text{eV}$ [1]. Since we are merely interested in energy differences, we will set ε_p to zero in the remainder of this thesis. Although, the TB Hamiltonian PHP is defined on a Hilbert space of one-particle states, the second quantized version of PHP is almost identical to the first quantized one. One obtains the second quantized Hamiltonian by the following substitutions:

$$
\begin{aligned}
|a_i\rangle &\to a_i, \\
|b_i\rangle &\to b_i,
\end{aligned}
\tag{2.31}
$$

where the creation and annihilation operators satisfy the standard anti-commutation relations. Throughout this thesis we will mostly adopt the language of second quantization.

Since the obtained TB Hamiltonian is invariant under lattice translations, Bloch's theorem applies. Hence, we rewrite the Hamiltonian in terms of Bloch waves. This yields

$$
PHP = \int_{BZ} \mathrm{d}\mathbf{k}|\Psi_{\mathbf{k}}\rangle H_{\mathbf{k}}\langle\Psi_{\mathbf{k}}|
\tag{2.32}
$$

with $|\Psi_{\mathbf{k}}\rangle = (|\Psi_{\mathbf{k}}^A\rangle, |\Psi_{\mathbf{k}}^B\rangle)$ and $\langle\Psi_{\mathbf{k}}| = (\langle\Psi_{\mathbf{k}}^A|, \langle\Psi_{\mathbf{k}}^B|)^T$ which should be interpreted as two-component vectors, and

$$
H_{\mathbf{k}} = t\begin{pmatrix} 0 & \gamma_{\mathbf{k}} \\ \gamma_{\mathbf{k}}^* & 0 \end{pmatrix},
\tag{2.33}
$$

here $\gamma_{\mathbf{k}} = \sum_{j=1}^3 e^{-i\mathbf{k}\cdot\delta_j}$. Hence, starting from the complicated Schrödinger equation, TB theory has now reduced the problem to diagonalizing a 2×2 matrix. Solving the eigenvalue equation $\det(H_{\mathbf{k}} - E(\mathbf{k})) = 0$ yields

$$
E_{\pm}(\mathbf{k}) = \pm t|\gamma_{\mathbf{k}}|,
\tag{2.34}
$$

here the $+(-)$ sign corresponds to the conduction (valence) band. The full dispersion relation is shown in Fig. 2.4(a). From this figure one may already infer that at the corners of the BZ, the so called K and K' points, the valence and conduction bands touch. Around these points the dispersion is linear, see Fig. 2.4(b). This results from the fact that around these points the Hamiltonian assumes the form the two-dimensional massless Dirac Hamiltonian. If we perform a Taylor expansion on the function γ_k around $\pm K$ we find

$$
\begin{aligned}
\gamma_{\pm K+\mathbf{k}} &= \gamma_{\pm K} + \nabla_{\mathbf{k}}\gamma_{\mathbf{k}}|_{\mathbf{k}=\pm K} \cdot \mathbf{k} \\
&= 0 + v_f(\pm k_x - ik_y)
\end{aligned}
\tag{2.35}
$$

here $v_F = 3at/2\hbar$ is the Fermi velocity. As a consequence we obtain

$$
H_{\pm K+\mathbf{k}} = v_f(\pm k_x\sigma_x + k_y\sigma_y)
\tag{2.36}
$$

Hence, we have now proved that the physics near the Fermi energy is described by the massless Dirac equation with c the speed of light replaced by the Fermi velocity $v_F \approx c/300$.
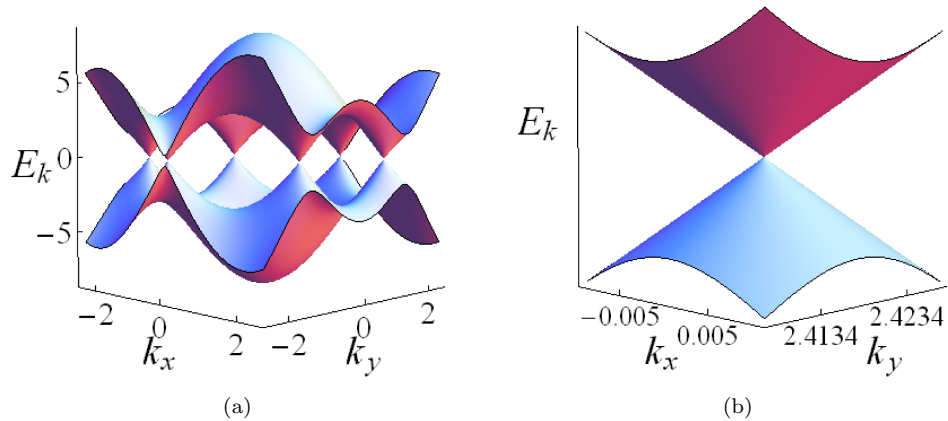
Fig. 2.4: Single-layer graphene dispersion relation. (a) Full dispersion relation for single-layer graphene. (b) Zoom-in on the Dirac cone.

2.4   Spin-orbit coupling

In the previous section we have completely neglected the spin of the electrons in graphene. In reality the electrons will experience a magnetic field due to their motion in the atomic electric field, and this magnetic field interacts with the electron spin. This type of SOC is known as intrinsic. Furthermore, when graphene lies on top of a substrate or an electric field is applied perpendicular to the graphene sheet another type of SOC is generated that is called Rashba SOC. Both types of SOC lead to a hybridization among the p_z and p_x, p_y, and s-orbitals. Therefore, to derive the corresponding SOC Hamiltonians one proceeds in the following way:

1. Write down the Schrödinger equation with the inclusion of the microscopic SOC Hamiltonians.

2. Instead of only considering TB theory for p_z orbitals, now include also the p_x, p_y, and s-orbitals.

3. Since the hybridization is considered to be small, which as it turns out is a good approximation in graphene, the low-energy physics is still mainly governed by the p_z-orbitals. As a result, one may integrate out the p_x, p_y, and s-orbitals and obtain an effective theory solely in terms of the p_z-orbitals that includes SOC.

The first and second step in this recipe are fairly straightforward. However, in the third step one may take different routes to obtain an effective theory. One of these approaches boils down to applying second-order degenerate perturbation theory in momentum space to calculate how the band structure
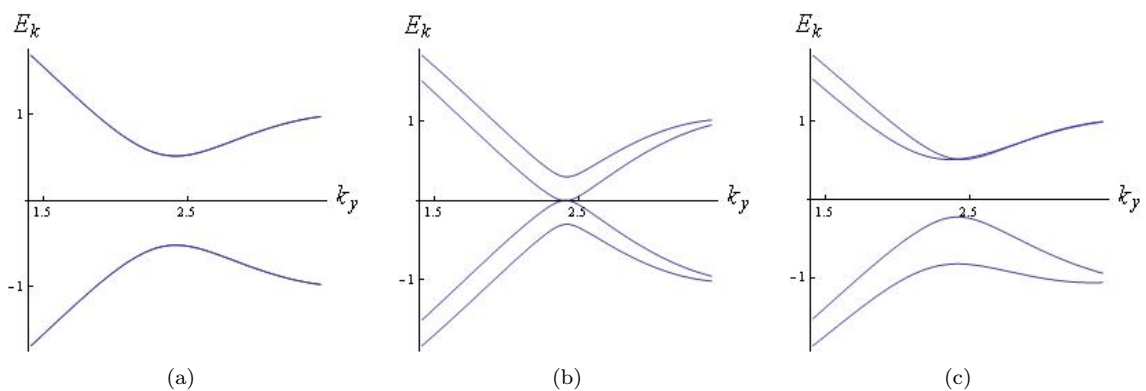

Fig. 2.5: Plots of the single-layer graphene dispersion relation along the line $k_x = 0$:(a) $\lambda_R = 0$ and $\lambda_I = 0.1$,(b) $\lambda_R = 0.1$ and $\lambda_I = 0$, and (c) $\lambda_R = 0.1$ and $\lambda_I = 0.1$.
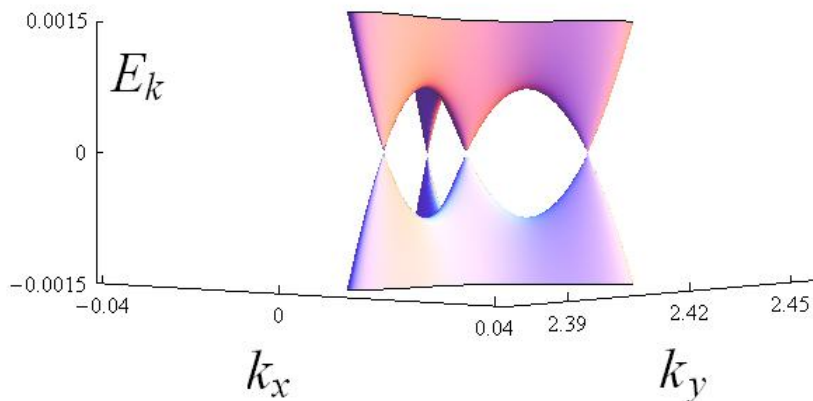
Fig. 2.6: Splitting of the Dirac cone into 4 Dirac cones due to the Rashba term.

changes at the $\pm K$ points due to SOC [22]. Another method amounts to writing down the transfer equations and then perturbatively integrate out the contributions from the high-energy orbitals [23]. We will not repeat these calculation here, but simply state the SOC Hamiltonians that apply to graphene. Moreover, in Chapter 4 we present a method that is more general than the previously discussed techniques. First, we discuss the intrinsic SOC after which we consider the Rashba SOC.

The intrinsic SOC Hamiltonian H_I is given by an next-nearest neighbors (NNN) hopping Hamiltonian

$$H_I = i\lambda_I \sum_{\langle\langle i,j\rangle\rangle} v_{ij}(a_i^\dagger \sigma_z a_j + b_i^\dagger \sigma_z b_j), \tag{2.37}$$

here $\langle\langle i,j\rangle\rangle$ denotes the summation over NNN, $v_{ij} = +(-)$ if the hopping is (anti) clock-wise, and λ_I is the intrinsic SOC parameter. One can solve this Hamiltonian exactly; however, here we just show the resulting band structure, see Fig. 2.5(a). As one can observe the intrinsic SOC opens up a gap at the $\pm K$ points. Hence, it changes graphene from a zero-gap semiconductor into a gapped system. In 2005 it was shown by Kane and Mele that this gap is topologically non-trivial [2]. We will discuss this shortly in section 2.9. Note that the spectrum is still spin-degenerate. This is to be expected since the full Hamiltonian is invariant under time-reversal and spatial inversion.

The Rashba SOC Hamiltonian H_R is given by a NN hopping term

$$H_R = i\lambda_R \sum_{\langle i,j\rangle} a_i^\dagger (\boldsymbol{\sigma} \times \hat{d}_{ij}) \cdot \hat{z} b_j + h.c., \tag{2.38}$$

with $\hat{d}_{ij}$ the unit vector pointing from site i to j and $\boldsymbol{\sigma}$ the vector of Pauli matrices. The most important difference with the intrinsic SOC is the fact that the Rashba SOC couples the different spin components whereas the intrinsic SOC does not. The band structure is shown in Fig. 2.5(b). If one zooms in on the $\pm K$ points, one observes that each of the Dirac cones splits into four distinct cones of which one is still located at the $\pm K$ points, see also Fig. 2.6. In the literature this is known as a Lifshitz transition, which means that the topology of the Fermi surface is altered. Furthermore, the spin degeneracy is lifted, which is a result of the fact that the Rashba SOC Hamiltonian is not invariant under spatial inversion. If we consider both Rashba and intrinsic SOC, we notice that depending on the relative values of λ_R and λ_I the gap closes or opens, see Fig. 2.5(c).

2.5 The Berry phase

In graphene the linear dispersion relation is protected by spatial inversion and time-reversal symmetry. In order to show this, we first need to introduce the Berry phase. The Berry phase is intimately connected with the adiabatic theorem. This theorem basically states, given some additional assumptions,

that for a Hamiltonian that varies slowly in time the system remains in its instantaneous eigenstate [24]. We will now formalize this statement. Suppose we are given some slowly varying Hamiltonian $H(t)$; then at each instance t, there exists an orthonormal basis of energy-eigenstates $|\Psi_n(t)\rangle$, with energies $E_n(t)$. The adiabatic theorem says that if one starts out in a state $|\Psi(0)\rangle = |\Psi_n(0)\rangle$, then at time t, the state is given by $|\Psi(t)\rangle = e^{-i\phi(t)}|\Psi_n(t)\rangle$. We may write the phase $\phi(t)$ as the sum of the dynamical phase $\int_0^t \mathrm{d}\tilde{t} E(\tilde{t})$ and an extra term $\gamma(t)$. This additional phase γ is referred to as the Berry phase.

To evaluate the Berry phase, we apply the Schrödinger equation to the state $|\Psi(t)\rangle$,

$$i\frac{\partial}{\partial t}|\Psi(t)\rangle = \left[E_n(t) + \dot{\gamma}(t)\right]e^{-i\phi(t)}|\Psi_n(t)\rangle + e^{-i\phi(t)}\frac{\partial}{\partial t}|\Psi_n(t)\rangle \qquad (2.39)$$
$$= H(t)|\Psi(t)\rangle$$
$$= E_n(t)|\Psi(t)\rangle,$$

where $\dot{\gamma}(t)$ denotes the time derivative of $\gamma(t)$. From this we obtain the following equality:

$$\dot{\gamma}(t)|\Psi_n(t)\rangle = -i\frac{\mathrm{d}}{\mathrm{d}t}|\Psi_n(t)\rangle. \qquad (2.40)$$

Now, suppose that the Hamiltonian actually depends on a set of parameters $\mathbf{u}(t) = (u_1, \dots, u_m)$, which vary slowly in time. Then by applying the chain rule we obtain

$$\dot{\gamma}(t)|\Psi_n(\mathbf{u}(t))\rangle = -i\sum_i \frac{\partial}{\partial u_i}|\Psi_n(\mathbf{u}(t))\rangle\frac{\mathrm{d}u_i}{\mathrm{d}t}. \qquad (2.41)$$

In order to eliminate the remaining ket, we apply the same bra from the left. This results in

$$\dot{\gamma}(t) = -i\sum_i \langle\Psi_n(\mathbf{u}(t))|\frac{\partial}{\partial u_i}|\Psi_n(\mathbf{u}(t))\rangle\frac{\mathrm{d}u_i}{\mathrm{d}t} \qquad (2.42)$$
$$= \sum_i A_i(\mathbf{u}(t))\frac{\mathrm{d}u_i}{\mathrm{d}t}.$$

We have implicitly defined the Berry vector potential A_i. Now with this notation we find

$$\gamma(t) = \sum_i \int A_i \cdot \frac{\mathrm{d}u_i}{\mathrm{d}t}\mathrm{d}t \qquad (2.43)$$
$$= \int_{\mathbf{u}(0)}^{\mathbf{u}(T)} \mathbf{A}(\mathbf{u}) \cdot \mathrm{d}\mathbf{u}.$$

Hence, the Berry phase is given as the line-integral of the Berry vector potential. One cannot assign any meaning to the absolute phase of a state, what matters is the relative phase between two states. To illustrate this we consider the two states $|\Psi(\mathbf{u})\rangle$, and $|\tilde{\Psi}(\mathbf{u})\rangle = e^{i\alpha(\mathbf{u})}|\Psi(\mathbf{u})\rangle$, where α is a real-valued function. Of course physically these states are indistinguishable, but their Berry phase potentials differ by a derivative, since

$$\tilde{A}_i = -i\langle\tilde{\Psi}|\frac{\partial}{\partial u_i}|\tilde{\Psi}\rangle \qquad (2.44)$$
$$= A_i + \frac{\partial \alpha}{\partial u_i}.$$

Hence the Berry phases at time t_f, are related by

$$\tilde{\gamma}(t_f) = \gamma(t_f) + \int_{\mathbf{u}(0)}^{\mathbf{u}(t_f)} \nabla\alpha \cdot \mathrm{d}\mathbf{u} \qquad (2.45)$$
$$= \gamma(t_f) + \left[\alpha(\mathbf{u}(t_f)) - \alpha(\mathbf{u}(0))\right].$$

Thus in general these Berry phases are dependent on the gauge you choose. However, if the path in parameter space is closed, then the Berry phase does not depend on the gauge choice up to integer multiples of 2π. From now on we refer to the Berry phase when we consider a closed path in parameter space. Since a closed line-integral can be related to a surface integral by invoking Stokes'theorem, we define the Berry curvature $F = \nabla \times A$, and note that

$$\gamma = \oint A \cdot \mathrm{d}u \tag{2.46}$$
$$= \int F \cdot \mathrm{d}S.$$

In section 2.9 we explore the relation between the Berry curvature F and the Hall conductance, but first we study time-reversal symmetry.

2.6   Time-reversal symmetry and Kramers' theorem

Symmetries in quantum mechaniscs, according to Wigner's theorem, are represented either by unitary or anti-unitary operators. A fundamental symmetry belonging to the latter class is time-reversal. Under time reversal time changes sign $t \to -t$, whereas the position remains invariant $x \to x$. Therefore $T\hat{x}T^\dagger = \hat{x}$, where T denotes the time-reversal operator. On the other hand, the momentum $\mathbf{p} \to -\mathbf{p}$, hence $T\hat{\mathbf{p}}T^\dagger = -\hat{\mathbf{p}}$. At first sight this seems trivial; however it has one important consequence, namely it forces T to be an anti-unitary operator. This can be seen by considering the canonical commutation relation, which should be invariant under time-reversal.

From the previous arguments we can already conclude that under time-reversal the orbital angular momentum $\hat{L}$ changes sign. We generalize this to the intrinsic spin, hence $\hat{S} \to -\hat{S}$ under time reversal. The time-reversal operator is the product of an unitary matrix U and the operator for complex conjugation K, and it turns out to be of the form $U = e^{i\phi}\sigma_y$ in a spin-1/2 system, with ϕ as an arbitrary phase.

From the above it follows that $T^2 = -I$. This has some important consequences for a time-reversal invariant Hamiltonian H. Since if $|n\rangle$ is an eigenstate of H, then so is $T|n\rangle$. However these two states are not related by a simple phase. This we can show by some simple algebra. Assume that the two states are related, $T|n\rangle = e^{-i\phi}|n\rangle$. Then,

$$\begin{aligned} T^2|n\rangle &= Te^{-i\phi}|n\rangle \\ &= e^{i\phi}T|n\rangle \\ &= e^{i\phi}e^{-i\phi}|n\rangle = |n\rangle. \end{aligned} \tag{2.47}$$

From this it follows that $T^2 = I$, contradicting $T^2 = -I$; hence our assumption has to be false. This has as a consequence that each eigenstate of the Hamiltonian is double-degenerate. This is known as Kramers' theorem. In some cases it leads to crossing of energy bands. For example this can be seen in the case of graphene with SOC included, see Fig.2.9. To lift the spin-degeneracy at the M-point, which is invariant under time-reversal, one has to break time-reversal symmetry.

Next, we study how time-reversal symmetry puts constraints on the Berry vector potential. We study a Bloch Hamiltonian H that has eigenstates $|\Psi_{\mathbf{k},a}\rangle$ labeled by a crystal momentum $\mathbf{k}$ and a band index a. It then follows that we may consider the Berry vector potential $A_a(\mathbf{k})$, which reads

$$A_a(k) = \langle \Psi_{k,a}|i\nabla_k|\Psi_{k,a}\rangle. \tag{2.48}$$

By definition every anti-unitary operator U satisfies

$$\langle U\Psi|U\Xi\rangle = \langle\Psi|\Xi\rangle^*, \tag{2.49}$$

for any two states $|\Psi\rangle$ and $|\Xi\rangle$. In particular this applies to the time-reversal operator T. Since the Berry vector potential is real, we obtain

$$\begin{aligned} A_a(\mathbf{k}) &= \langle T\Psi_{\mathbf{k},a}|Ti\nabla_{\mathbf{k}}|\Psi_{\mathbf{k},a}\rangle \\ &= -\langle T\Psi_{\mathbf{k},a}|i\nabla_{\mathbf{k}}T|\Psi_{\mathbf{k},a}\rangle. \end{aligned} \tag{2.50}$$
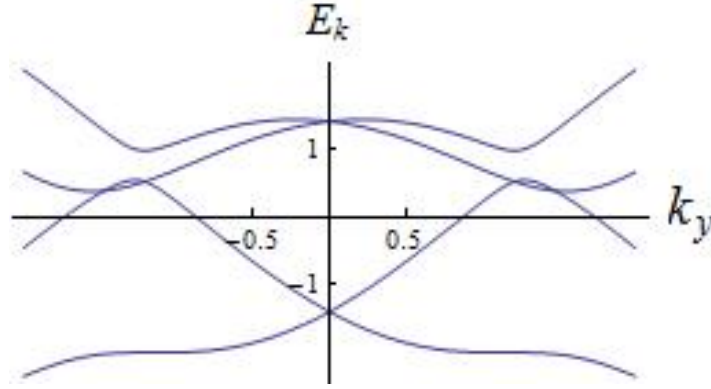
Fig. 2.7: Cut along the line $k_x = 2\pi/3$ of the single-layer graphene dispersion relation with $\lambda_R = 0.5$eV and $\lambda_I = 0.1$eV. The M-point is located at $k_y = 0$.

Here, in the second line we used that T anti-commutes with i. Given that the Hamiltonian H is invariant under time reversal, we find that $T|\Psi_{a,\mathbf{k}}\rangle = e^{i\phi(\mathbf{k})}|\Psi_{a,-\mathbf{k}}\rangle$, with $\phi(\mathbf{k}) \in \mathbb{R}$. This yields

$$\begin{aligned}
A_a(\mathbf{k}) &= -\langle\Psi(-\mathbf{k})|e^{i\phi(\mathbf{k})}i\nabla_\mathbf{k}e^{-i\phi(\mathbf{k})}|\Psi(-\mathbf{k})\rangle \\
&= \langle\Psi(-\mathbf{k})|e^{i\phi(\mathbf{k})}i\nabla_{-\mathbf{k}}e^{-i\phi(\mathbf{k})}|\Psi(-\mathbf{k})\rangle \\
&= A_a(-\mathbf{k}) - \nabla_\mathbf{k}\phi(\mathbf{k}).
\end{aligned} \tag{2.51}$$

Hence, we have now proved that for a system that is invariant under time-reversal the vector potentials $A(\mathbf{k})$ and $A(-\mathbf{k})$ are related by a total derivative. At the level of the Berry curvature this translates into the fact $F(\mathbf{k}) = -F(-\mathbf{k})$.

2.7 Spatial inversion

Inspection of the honeycomb lattice shows that the honeycomb lattice is invariant under inversion through the center of the unit cell. The TB Hamiltonian (2.30) inherits this symmetry. If P denotes the inversion operator we can make this more precise by stating that the annihilation operators defined in Eq. (2.31) transform as

$$\begin{aligned}
Pa_iP^{-1} &= b_{-i} \\
Pb_iP^{-1} &= a_{-i},
\end{aligned} \tag{2.52}$$

where we assume $\mathbf{R}_i = -\mathbf{R}_{-i}$. From this one can derive how the other operators transform. For example we study how spatial inversion affects the operator a_k

$$Pa_\mathbf{k}P = P\sum_i e^{i\mathbf{k}\cdot\mathbf{R}_i}a_iP = \sum_i e^{i\mathbf{k}\cdot\mathbf{R}_i}b_{-i} = \sum_{-i}e^{-i\mathbf{k}\mathbf{R}_i}b_i = b_{-\mathbf{k}}. \tag{2.53}$$

Hence, spatial inversion interchanges the two sublattices and reverses the crystal momentum. One may ask whether spatial inversion imposes certain conditions on the Berry vector potential. To study this we assume that the Hamiltonian H commutes with P. Since P is unitary, we may write

$$\begin{aligned}
A_a(\mathbf{k}) &= \langle\Psi_{\mathbf{k},a}|i\nabla_\mathbf{k}|\Psi_{\mathbf{k},a}\rangle \\
&= \langle P\Psi_{\mathbf{k},a}|Pi\nabla_\mathbf{k}|\Psi_{\mathbf{k},a}\rangle.
\end{aligned} \tag{2.54}$$

One can show that P commutes with $i\nabla_\mathbf{k}$. Therefore, one obtains

$$\begin{aligned}
A_a(\mathbf{k}) &= \langle P\Psi_{\mathbf{k},a}|i\nabla_\mathbf{k}P|\Psi_{\mathbf{k},a}\rangle \\
&= \langle\Psi_{-\mathbf{k},a}|e^{i\phi(\mathbf{k})}i\nabla_\mathbf{k}e^{-i\phi(\mathbf{k})}|\Psi_{-\mathbf{k},a}\rangle \\
&= -A_a(-\mathbf{k}) - \nabla_k\phi(\mathbf{k}).
\end{aligned} \tag{2.55}$$

So indeed, the presence of inversion symmetry guarantees that the Berry vector potentials $A_a(\mathbf{k})$ and $A_a(-\mathbf{k})$ differ by a minus sign (up to a gauge transformation).

2.8 Symmetries and graphene

Now we will compute the Berry phase for a very simple example. We consider single-layer graphene. The Hamiltonian is given by

$$H \quad = \quad \int \mathrm{d}\mathbf{k}\Psi^{\dagger}\left(\mathbf{k}\right)H\left(\mathbf{k}\right)\Psi\left(\mathbf{k}\right). \tag{2.56}$$

We consider the Berry phase of loops encircling the Dirac points. Around the Dirac points the Hamiltonian satisfies

$$H\left(\pm K + \mathbf{k}\right) \quad \approx \quad v_F \begin{pmatrix} 0 & \pm k_x - ik_y \\ \pm k_x + ik_y & 0 \end{pmatrix}. \tag{2.57}$$

Hence, in order to compute the Berry phase we may use the massless Dirac Hamiltonian. For each value of k we can find an eigenstate $\Psi^{\pm}(\mathbf{k})$ of $H(\pm K + \mathbf{k})$ with eigenvalue $v_F\|\mathbf{k}\|$,

$$\Psi^{\pm}(\mathbf{k}) \quad = \quad \frac{1}{\sqrt{2}}(1, \pm e^{i\phi})^T, \tag{2.58}$$

where we used $k_x + ik_y = e^{i\phi}\|\mathbf{k}\|$. To calculate the Berry phase of the two curves encircling the Dirac points, we switch to polar coordinates (k, ϕ), then the Berry potential is given by

$$A_k^{\pm} \quad = \quad -i\langle \Psi^{\pm}\left(k\right)|\partial_k|\Psi^{\pm}\left(k\right)\rangle \tag{2.59}$$

$$A_\phi^{\pm} \quad = \quad = -i\langle \Psi^{\pm}\left(k\right)|\partial_\phi|\Psi^{\pm}\left(k\right)\rangle \tag{2.60}$$

$$= \quad -\frac{i}{2}\left(\pm i\right) = \pm\frac{1}{2}.$$

As a result we find $\gamma^{\pm} = \oint A^{\pm}\left(k\right)\cdot \mathrm{d}k = \int_0^{2\pi} A_\phi^{\pm}\mathrm{d}\phi = \pm\pi$. This is in agreement with time-reversal symmetry and inversion symmetry, since these symmetries impose $\gamma^{+} + \gamma^{-} = 0 \bmod 2\pi$ and $\gamma^{+} - \gamma^{-} = 0 \bmod 2\pi$. However if one computes the Berry phase by invoking Stokes theorem, one obtains $F = 0$, and hence $\gamma^{\pm} = 0$. The solution to this paradox lies in the fact that A is ill-defined at $\pm K$ due to the band touching. As a consequence, the domain of A is not simply connected and one may not invoke Stokes theorem.

In particular, this result guarantees that the Dirac points are locally stable if both time-reversal and inversion symmetry are respected. If a gap would open at the $\pm K$ points, then A is well defined everywhere in the BZ. Therefore, we may invoke Stokes' theorem, which then yields $\gamma^{\pm} = 0$.

It turns out that we may obtain the same results by solely focusing on the Hamiltonian. Suppose we consider a time-reversal and inversion invariant 2×2 Hamiltonian, then we may express this Hamiltonian H_k as

$$H\left(\mathbf{k}\right) = f_x\left(\mathbf{k}\right)\sigma_x + f_y\left(\mathbf{k}\right)\sigma_y + g\left(\mathbf{k}\right)I_{2\times 2}, \tag{2.61}$$

where f_i and g are real valued functions. Normally one would include a term multiplying the σ_z matrix, but this violates time-reversal and inversion symmetry. Since the identity matrix does not affect the band touching, we may set $g = 0$ above. Next, we make a graphic representation of this Hamiltonian by drawing at each crystal momentum (k_x, k_y) the vector $(f_x(\mathbf{k}), f_y(\mathbf{k}))$. In Fig.2.8 we have made such a representation for graphene's low-energy Hamiltonian (2.57). One can easily see that the K point shows a vortex, whereas the $-K$ point exhibits an anti-vortex. Now suppose that we change the Hamiltonian in a continuous way, whilst respecting time-reversal symmetry and inversion symmetry. Then it is easily seen that we cannot remove the vortex and anti-vortex. Since a vortex and anti-vortex correspond to band-touching points we conclude that these points are protected.

2.9 Topological insulators

In section 2.4 we showed that the intrinsic SOC can open a gap in graphene and turns it into a (topological) insulator. It turns out that in graphene there are many possibilities to open a gap, a nice overview
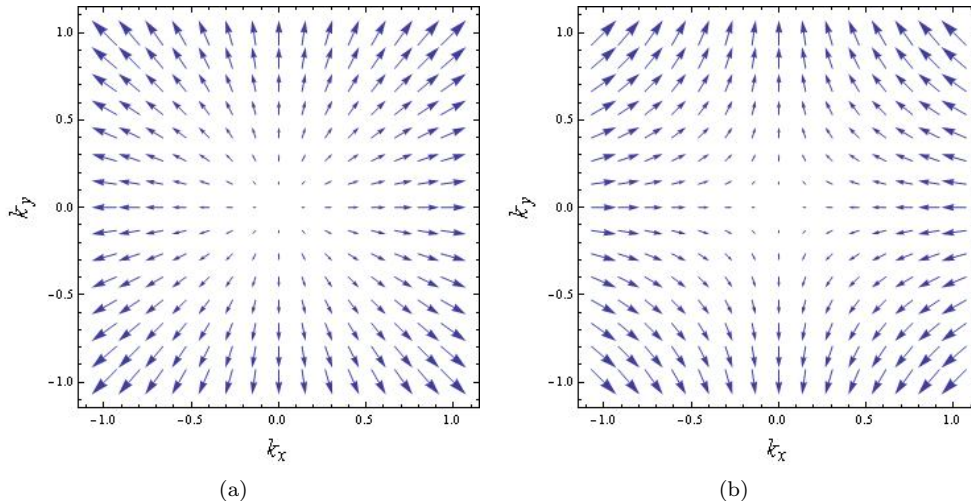
Fig. 2.8: Graphic representation of single-layer graphene Hamiltonian. (a) Vectorplot for graphene Hamiltonian near K point. (b)Vectorplot for graphene Hamiltonian near K' point.

is given in Ref. [25]. For example one can break the sublattice symmetry by giving the A and B sublattices a different on-site energy [26]. Another possibility is to break time-reversal symmetry by applying a staggered magnetic flux such that the net flux through each plaquette of the honeycomb lattice is zero [27]. It turns out that one can distinguish insulators by the topology of their band structures. This means that to deform insulators with different topologies into each other one has to close the insulating gap. One may compare this with the fact that one can not smoothly deform a sphere into a torus.

A well known example of an insulator with a non-trivial topology is the integer quantum Hall state. This state can be realized if a two-dimensional electron gas is subjected to a strong perpendicular magnetic field and an in-plane voltage is applied. It turns out that this state is characterized by an insulating bulk that forces the longitudinal conductance to vanish, whereas both edges of the system host N channels that carry the Hall currents that flow perpendicular to the direction of the electric field. As a result the Hall conductance is quantized

$$\sigma_{xy} = N\frac{e^2}{h}. \tag{2.62}$$

It should be stressed that these edge currents are chiral, meaning that on each edge all electrons move in the same direction. Precisely this feature is at the root of the exact quantization of the Hall conductance, because the chirality of the edge currents prevent them from backscattering.

It was shown in a paper by Thouless, Kohmoto, Nightingale, and den Nijs (TKNN) that one can relate the Hall conductance to a topological invariant associated with a Bloch Hamiltonian describing the bulk [28]. By making use of the Kubo formula, TKNN showed that

$$\sigma_{xy} = \frac{e^2}{h} \sum_{a \in \text{ filled bands}} c_a, \tag{2.63}$$

where c_a is the first Chern number corresponding to band a. This number is a topological invariant and given by

$$c_a = \frac{1}{2\pi} \int_{BZ} \mathrm{d}k F_a(k), \tag{2.64}$$

where $F_a(k)$ is the Berry curvature of band a. In particular this formula relates the number of edge states to a quantity obtained from the bulk Hamiltonian. This result is known as the bulk-edge

correspondence. Since the number of edge channels is given by a topological invariant one can not smoothly deform the quantum Hall phase into a trivial insulator. It turns out that Eq. (2.63) applies to all insulating systems described by a Bloch Hamiltonian. In particular, it applies to graphene with intrinsic SOC. However, for this system the contributions coming from the spin up electrons are canceled by the spin down electrons. More precisely, for graphene we find

$$\sigma_{xy} = \frac{e^2}{h}(c_{-,\uparrow} + c_{-,\downarrow}) = \frac{e^2}{h}(1 + (-1)) = 0. \tag{2.65}$$

This is not a mere coincidence, but results from the fact that this system is invariant under time-reversal. In general, one can show that for a system that is invariant under time reversal symmetry and where no spin mixing occurs, one obtains

$$c_{a,\uparrow} = -c_{a,\downarrow}. \tag{2.66}$$

As a result the Hall conductance vanishes. Kane and Mele showed that graphene with intrinsic SOC gives rise to the quantum spin Hall effect characterized by a quantized spin Hall conductance, which is defined as

$$\sigma_{xy}^{\text{spin}} = \frac{\hbar}{2e}(\sigma_{xy,\uparrow} - \sigma_{xy,\downarrow}) = \frac{e}{2\pi}. \tag{2.67}$$

This corresponds to a state with insulating bulk and edges that carry helical currents. This means that on each edge the spin up and spin down electrons move in opposite directions. One might wonder whether such a state is stable. For example, we have already seen that a substrate can induce a coupling between the different spin species. This may lead to backscattering and potentially could destroy the quantum spin Hall effect turning it into a trivial insulator. However, one may show that if the number of edge channels per spin is odd then it in not possible to deform this state into a trivial insulator without closing the gap in the bulk of the system. This follows from Kramers' theorem and is illustrated in Fig. 2.9. It turns out that in general one can assign to each time-reversal symmetric insulator a $\mathbb{Z}_2$ topological invariant where 1 corresponds to a topological insulator and 0 to a trivial insulator. For a system without spin-mixing the value of this $\mathbb{Z}_2$ invariant ν is given by

$$\nu = \sum_{a \in \text{ filled bands}} c_{a,\uparrow} \text{ mod } 2 \tag{2.68}$$

So indeed graphene with intrinsic SOC gives rise to the quantum spin Hall effect. However, it should be stressed that in graphene the value of the SOC parameter is too small, and therefore this effect has not been measured. However, the quantum spin hall effect has been experimentally realized in HgTe/CdTe quantum wells [29].
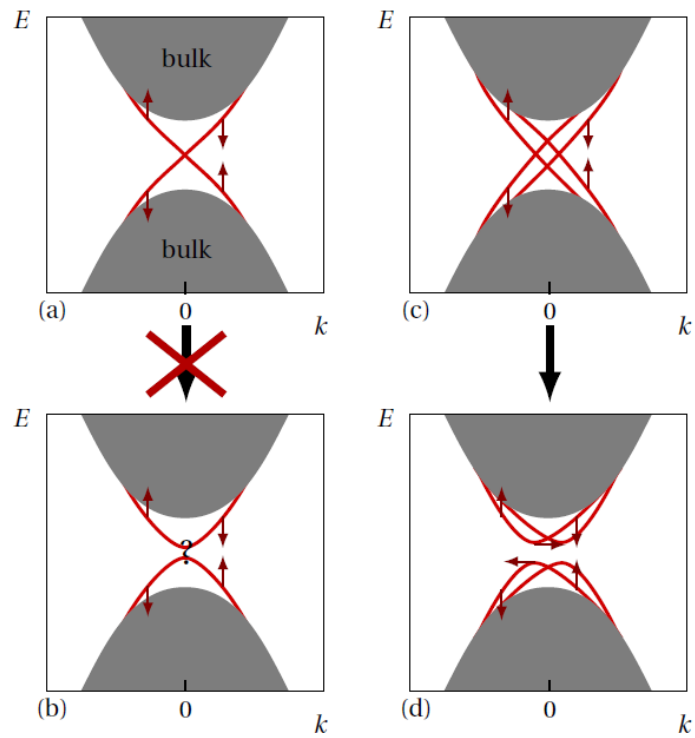
Fig. 2.9: Illustration of the topological $\mathbb{Z}_2$ invariant for time-reversal symmetric systems. (a) Band structure exhibiting one pair of edge channels that connects the valence and conduction bands. Note the crossing at zero momentum. (b) To open a gap in (a) at zero momentum, one has to break time-reversal symmetry. (c) Band structure exhibiting two pairs of edge channels that connect the valence and conduction band. (d) For the system shown in (c) one can open a gap whilst respecting time-reversal symmetry, because now the crossings do not occur at the time-reversal invariant momentum $k = 0$. Figure extracted from Ref. [30].

3. TIGHT-BINDING DESCRIPTION OF GRAPHYNES WITHOUT SPIN-ORBIT COUPLING

As announced in the introduction, we specifically focus on the three graphynes α, β, and γ-graphyne. In this chapter we show how one can study their band structures using TB theory.

The three types of graphyne can all be described in terms of a TB model that takes into account only the p_z orbitals. It was also shown that one can integrate out the contributions coming from the acetylene bonds to derive an effective model (see also App. A) [31, 16]. By doing so, one can describe α-graphyne by the same Hamiltonian as used for graphene, but with a different value of the NN hopping parameter. On the other hand, β- and γ-graphyne are well described by an effective six-site model, with two hopping parameters. Below we discuss separately the band structure for each type of graphyne and describe the system by an effective Hamiltonian.

3.1 α-graphyne

Of all graphynes, α-graphyne is the simplest. One can envision α-graphyne as being obtained from graphene upon insertion of two more carbon atoms bonded by an acetylene linkage between any two carbon atoms of the honeycomb graphene lattice. As a result, the number of atoms in the unit cell grows from 2 to 8, see Fig. 3.1(a). To describe this system in terms of a TB model, we will need two different hopping parameters: $t_{\alpha,2}$ and $t_{\alpha,3}$. Using the labeling shown in Fig. 3.1(a), the Hamiltonian reads

$$H^\alpha = t_{\alpha,2} \sum_{\langle i,j \rangle} \left[A_i^\dagger \left(a_{1,j} + a_{2,j} + a_{3,j} \right) + B_i^\dagger \left(b_{1,j} + b_{2,j} + b_{3,j} \right) \right] + t_{\alpha,3} \sum_{\langle i,j \rangle} \left(a_{1,i}^\dagger b_{1,j} \right.$$
$$\left. + a_{2,i}^\dagger b_{2,j} + a_{3,i}^\dagger b_{3,j} \right) + h.c. \tag{3.1}$$

By integrating out the electrons forming the acetylene bonds (see App. B.1), we obtain an effective low-energy Hamiltonian

$$H_{\text{eff}}^\alpha = \tilde{t}_\alpha \sum_{\langle i,j \rangle} A_i^\dagger B_j + h.c., \tag{3.2}$$

where $\tilde{t}_\alpha = -t_{\alpha,2}^2 t_{\alpha,3} / (3t_{\alpha,2}^2 + t_{\alpha,3}^2)$. Fitting the TB-parameters with a first-principles calculation[31] yields $t_{\alpha,2} = -2.85\text{eV}$ and $t_{\alpha,3} = -7.50\text{eV}$, hence $\tilde{t}_\alpha = 0.76\text{eV}$. As shown in Fig. 3.2(a), the band structure obtained from the low-energy approximation (red dashed lines) fits very well the band structure obtained from the full TB model (blue solid lines).

Since the physics around the Fermi-energy in α-graphyne is described by the same Hamiltonian as graphene, it comes as no surprise that α graphyne exhibits two Dirac cones at the K and K' points, see Figs. 3.2(a) and 3.3(a). The main difference with graphene is the reduced Fermi velocity. In graphene the Fermi velocity is given by $v_F \approx 3at/2\hbar$, with $t \approx -2.8\text{eV}$ the hopping amplitude [1] and a the NN distance, whereas in α-graphyne $v_F \approx 9a\tilde{t}_\alpha/2\hbar$. Note that in graphene the NN distance $a = 1.42\text{Å}$ [1], whereas in α-graphyne there are actually two different bond lengths, one for the single bond $d_s = 1.40\text{Å}$ and one for the triple bond $d_t = 1.23\text{Å}$ [16]. However, setting d_s and d_t equal to the bond length a in graphene gives an error smaller than 10%. Since α-graphyne is described by the same Hamiltonian as graphene, the Dirac cones in α-graphyne are also protected by time-reversal and inversion symmetry.
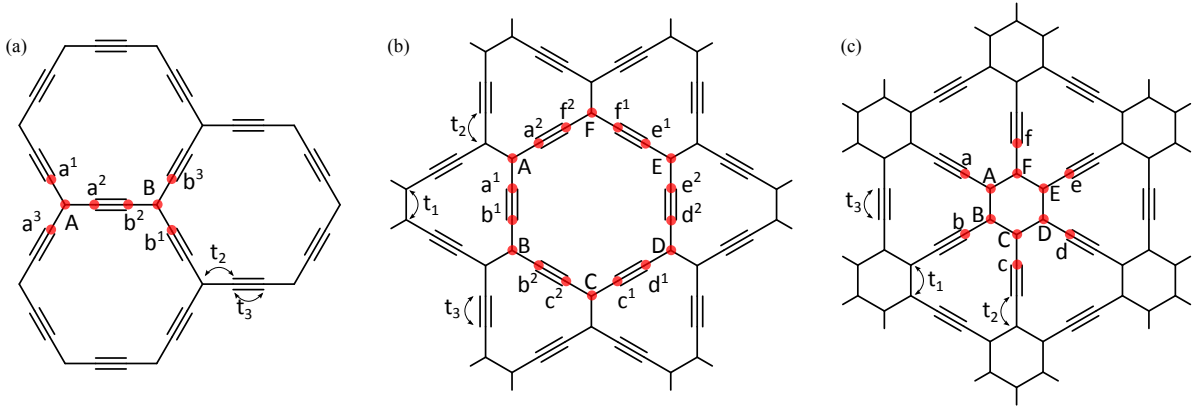
Fig. 3.1: Lattice structure of α-, β- and γ-graphyne, shown in panels (a), (b), and (c), respectively. Atoms at the vertices are denoted by capital letters, whereas atoms located at the edges are denoted by lower-case letters. The hopping parameters t_i are also shown, with the subscripts 1, 2, and 3 corresponding to vertex-vertex, vertex-edge, and edge-edge hoppings, respectively.

3.2 β-graphyne

Among the three different types of graphyne that we consider, β-graphyne has the most complicated lattice structure. Its unit cell involves 18 atoms and consists of a large hexagon, which has one carbon atom located at each vertex, and two carbon atoms connected by an acetylene linkage between each two neighboring vertices, see Fig. 3.1(b). A TB description of β-graphyne requires three different hopping parameters: $t_{\beta,1}$, $t_{\beta,2}$, and $t_{\beta,3}$. Using the labeling displayed in Fig. 3.1(b), the TB Hamiltonian reads

$$
\begin{aligned}
H^\beta = {}& t_{\beta,1} \sum_{\langle i,j \rangle} \left(A_i^\dagger D_j + B_i^\dagger E_j + C_i^\dagger F_j \right) + t_{\beta,2} \sum_{\langle i,j \rangle} \left[A_i^\dagger \left(a_{1,j} + a_{2,j} \right) + B_i^\dagger \left(b_{1,j} + b_{2,j} \right) \right. \\
& + C_i^\dagger \left(c_{1,j} + c_{2,j} \right) + D_i^\dagger \left(d_{1,j} + d_{2,j} \right) + E_i^\dagger \left(e_{1,j} + e_{2,j} \right) + \left. F_i^\dagger \left(f_{1,j} + f_{2,j} \right) \right] \\
& + t_{\beta,3} \sum_{\langle i,j \rangle} \left(a_{1,i}^\dagger b_{1,j} + b_{2,i}^\dagger c_{2,j} + c_{1,i}^\dagger d_{1,j} + d_{2,i}^\dagger e_{2,j} + e_{1,i}^\dagger f_{1,j} + f_{2,i}^\dagger a_{2,j} \right) + h.c.
\end{aligned}
\tag{3.3}
$$

By performing a Fourier transformation and subsequently eliminating the high-energy orbitals (see App. B.2), we obtain an effective six-site model. The effective low-energy Hamiltonian reads

$$
\begin{aligned}
H_{\text{eff}}^\beta = {}& t_{\text{int}}^\beta \sum_{\langle i,j \rangle} \left[A_i^\dagger \left(B_j + F_j \right) + C_i^\dagger \left(B_j + D_j \right) + E_i^\dagger \left(D_j + F_j \right) \right] \\
& + t_{\text{ext}}^\beta \sum_{\langle i,j \rangle} \left[A_i^\dagger D_j + C_i^\dagger F_j + E_i^\dagger B_j \right] + h.c.,
\end{aligned}
\tag{3.4}
$$

where $t_{\text{int}}^\beta = -t_{\beta,2}^2 t_{\beta,3} / (2t_{\beta,2}^2 + t_{\beta,3}^2)$ and $t_{\text{ext}}^\beta = t_{\beta,1} t_{\beta,3}^2 / (2t_{\beta,2}^2 + t_{\beta,3}^2)$. In β-graphyne, it is found[31] that $t_{\beta,1} = -2.00$eV, $t_{\beta,2} = -2.70$eV, and $t_{\beta,3} = -4.30$eV, hence $t_{\text{int}}^\beta = 0.95$eV and $t_{\text{ext}}^\beta = -1.12$eV. It turns out that the agreement between this effective model (red dashed lines) and the full TB Hamiltonian (blue solid lines) is extremely good, see Fig. 3.2(b). Note that the dispersion relation exhibits six Dirac cones, located on the line $\Gamma - M$ [see also Fig. 3.3(b)]. As opposed to graphene and α-graphyne, where the cones exhibit a threefold symmetry, in β-graphyne the cones are symmetric under mirror reflection through the normal plane containing the line Γ-M [13].

3.3 γ-graphyne

γ-graphyne has a somewhat simpler structure than β-graphyne, as its unit cell contains only 12 atoms, see Fig. 3.1(c). The TB description of γ-graphyne involves three hopping parameters: $t_{\gamma,1}$, $t_{\gamma,2}$, and
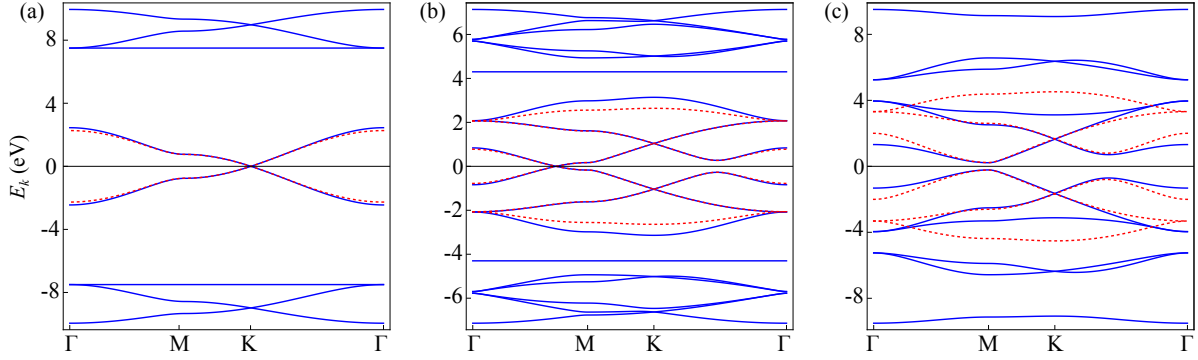
Fig. 3.2: Dispersion relation for α-, β-, and γ-graphyne, along high-symmetry lines, shown in (a), (b), and (c), respectively. The (blue) solid lines correspond to the dispersion relation obtained from the full TB Hamiltonian, whereas the (red) dashed lines correspond to the dispersion relation obtained from the low-energy approximation.

$t_{\gamma,3}$. Using the labeling shown in Fig. 3.1(c), we find that H^γ is given by

$$H^\gamma = t_{\gamma,1} \sum_{\langle i,j \rangle} \left[A_i^\dagger \left(B_j + F_j \right) + C_i^\dagger \left(B_j + D_j \right) + E_i^\dagger \left(D_j + F_j \right) \right] + t_{\gamma,2} \sum_{\langle i,j \rangle} \left(A_i^\dagger a_j \right.$$
$$\left. + B_i^\dagger b_j + C_i^\dagger c_j + D_i^\dagger d_j + E_i^\dagger e_j + F_i^\dagger f_j \right) + t_{\gamma,3} \sum_{\langle i,j \rangle} \left(a_i^\dagger d_j + b_i^\dagger e_j + c_i^\dagger f_j \right) + h.c. \quad (3.5)$$

As for β-graphyne, here we also perform a Fourier transformation (see App. B.3), then eliminate the high-energy orbitals, to obtain the effective model

$$H_{\text{eff}}^\gamma = t_{\text{int}}^\gamma \sum_{\langle i,j \rangle} \left[A_i^\dagger \left(B_j + F_j \right) + C_i^\dagger \left(B_j + D_j \right) + E_i^\dagger \left(D_j + F_j \right) \right]$$
$$+ t_{\text{ext}}^\gamma \sum_{\langle i,j \rangle} \left[A_i^\dagger D_j + C_i^\dagger F_j + E_i^\dagger B_j \right] + h.c., \quad (3.6)$$

with $t_{\text{int}}^\gamma = t_{\gamma,1} t_{\gamma,3}^2 / (t_{\gamma,2}^2 + t_{\gamma,3}^2)$ and $t_{\text{ext}}^\gamma = -t_{\gamma,2}^2 t_{\gamma,3} / (t_{\gamma,2}^2 + t_{\gamma,3}^2)$. Mapping this TB model to DFT calculations[31] yields $t_{\gamma,1} = -2.75$eV, $t_{\gamma,2} = -3.11$eV, and $t_{\gamma,3} = -4.04$eV, hence $t_{\text{int}}^\gamma = -1.73$eV and $t_{\text{ext}}^\gamma = 1.50$eV. The band structure does not exhibit any Dirac points at the Fermi energy, see Figs. 3.2(c) and 3.3(c). The gap at the M point is approximately equal to 0.44eV. Notice that the low-energy approximation is less accurate for γ-graphyne than for α- and β-graphyne due to the presence of a band gap.

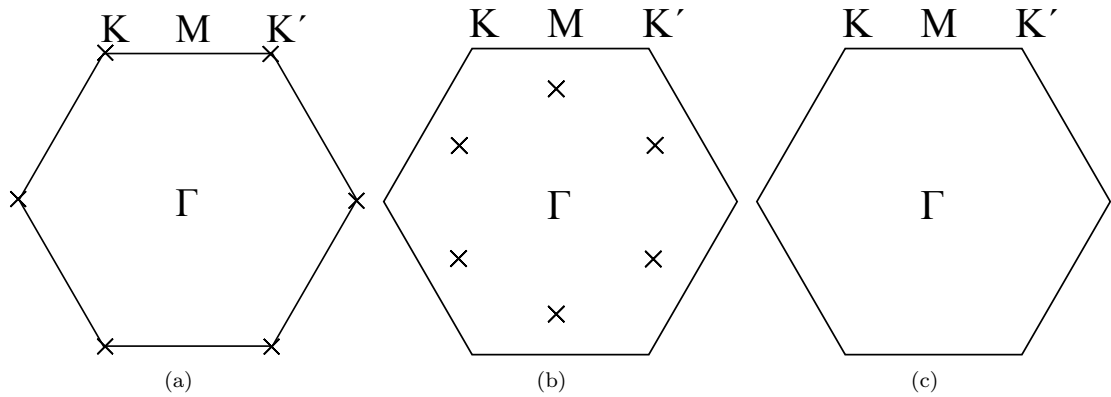Fig. 3.3: Sketch of BZ for α-, β-, and γ-graphyne, shown in panels (a), (b), and (c), respectively. The crosses correspond to Dirac cones.

4. TIGHT-BINDING THEORY OF SPIN-ORBIT COUPLING

Whereas the SOC has been extensively studied in graphene, this coupling has been rather unexplored in graphynes. In this Chapter, we derive the TB Hamiltonians corresponding to both Rashba and intrinsic SOC. Moreover, we show how the effective coupling parameters are related to the microscopic hopping parameters.

4.1 Microscopic origin of spin-orbit coupling

The intrinsic SOC originates from relativistic corrections to the Schrödinger equation. By expanding the Dirac equation up to second order in v/c, with v denoting the electron velocity, one finds that the microscopic Hamiltonian acquires an additional term

$$H_L = -\frac{\hbar}{4mc^2}\boldsymbol{\sigma}\cdot(\mathbf{p}\times\nabla V),\tag{4.1}$$

where $\boldsymbol{\sigma}$ is a vector of Pauli matrices, $\mathbf{p}$ is the momentum, m is the electron mass, and V is the nuclear potential [32]. If one rewrites this expression in spherical coordinates, one obtains

$$H_L = -f(r)\boldsymbol{\sigma}\cdot\mathbf{L},\tag{4.2}$$

where f is a function that goes rapidly to zero away from the origin and $\mathbf{L}$ is the orbital angular momentum. In order to see how this additional Hamiltonian enters the TB models, we need to reconsider the derivation presented in Chapter 3. The models we wrote down only describe the band-structure due to the p_z orbitals, but the bonds in graphyne are formed by the s, p_x, and p_y orbitals, which are called σ orbitals due to their symmetry. When SOC is not involved, the σ and p_z orbitals decouple since the former are even and the latter are odd with respect to mirror reflection through the $x-y$ plane. The inclusion of spin changes this picture drastically. Reflection through the $x-y$ plane is represented by σ_z in spin-space and therefore we find that spin up ($|\uparrow\rangle$) is even, whereas spin down ($|\downarrow\rangle$) is odd under this transformation. Hence, this symmetry allows now for the coupling between $p_{z,\uparrow}$, $p_{x,\downarrow}$, $p_{y,\downarrow}$, and $s_\downarrow$ orbitals, which are odd under this reflection. Analogously, it follows that the orbitals $p_{z,\downarrow}$, $p_{x,\uparrow}$, $p_{y,\uparrow}$, and $s_\uparrow$, which are even under this symmetry operation, can be coupled. Moreover, when an external electric field is applied perpendicularly to the $x-y$ plane, the microscopic Hamiltonian acquires a term

$$H_E = Ez,\tag{4.3}$$

with E the magnitude of the applied electric field. This microscopic Hamiltonian H_E couples now the s orbitals to the p_z orbitals. This can be seen as a consequence of the broken mirror symmetry. It turns out that the combination of the terms H_L and H_E leads to the Rashba SOC, while H_L alone leads to the intrinsic SOC. Hence, in order to describe SOC in graphyne we have to include both the p_z- and the σ-orbitals. On top of the SOC generated by the σ-orbitals we also need to consider the effect of the inclusion of the d_{xz} and d_{yz} orbitals, as it has been shown before for graphene [23]. However, the nature of this effect is entirely different, because even without considering spin, the p_z orbitals already couple to the d_{xz} and d_{yz} orbitals. The intrinsic SOC leads to a spin dependent on-site hoppings between the d_{xz} and d_{yz} orbitals. In the following, we discuss separately the SOC generated by the σ-orbitals and by the d-orbitals.

4.2   Spin-orbit coupling generated by the σ-orbitals

Since we have to include the σ-orbitals and spin, the number of orbitals in the TB models increases by a factor of eight (two for spin, four for orbitals). The corresponding Hamiltonian reads

$$H = H_z + H_\sigma + H_{SOC}^{z,\sigma} + \left(H_{SOC}^{z,\sigma}\right)^\dagger, \tag{4.4}$$

where H_z describes the p_z orbitals, H_σ describes the σ orbitals (see App. C), and $H_{SOC}^{z,\sigma}$ accounts for the hopping from p_z orbitals to σ-orbitals due to the SOC. The latter can be decomposed as

$$H_{SOC}^{z,\sigma} = H_L^{z,\sigma} + H_E^{z,\sigma}, \tag{4.5}$$

with the orbital angular momentum and electric field terms given by

$$H_L^{z,\sigma} = \xi_{p1} \sum_i{}' p_{z,i}^\dagger \left(-i\sigma_y p_{x,i} + i\sigma_x p_{y,i}\right) + \xi_{p2} \sum_i{}'' p_{z,i}^\dagger \left(-i\sigma_y p_{x,i} + i\sigma_x p_{y,i}\right), \tag{4.6}$$

$$H_E^{z,\sigma} = \xi_{sp1} \sum_i{}' p_{z,i}^\dagger s_i + \xi_{sp2} \sum_i{}'' p_{z,i}^\dagger s_i, \tag{4.7}$$

where $p_{z,i}^\dagger$ creates an electron in a p_z orbital at position i, and analogous notation is used for the p_x, p_y, and s orbitals. These terms result from considering the matrix elements $\boldsymbol{\sigma} \cdot \mathbf{L}$ and Ez, see also Table 4.1. For example we may consider the matrix element $\langle p_z|\boldsymbol{\sigma} \cdot \mathbf{L}|p_x\rangle$. As a first step we rewrite L_x and L_y in terms of raising and lowering operators

$$L_x = \frac{1}{2}(L_+ + L_-),$$
$$L_y = -\frac{i}{2}(L_+ - L_-) \tag{4.8}$$

Next, one rewrites the real atomic orbitals p_x, p_y, and p_z in terms of the complex orbitals $|n, l, m\rangle$ that are simultaneously eigenstates of the operators H, L^2 and L_z. Since all the orbitals we consider are in the second shell, which corresponds to $n = 2$, we simply write $|2, l, m\rangle = |l, m\rangle$. This then reads:

$$|p_x\rangle = \frac{1}{\sqrt{2}}(-|1, 1\rangle + |1, -1\rangle),$$
$$|p_y\rangle = \frac{i}{\sqrt{2}}(|1, 1\rangle + |1, -1\rangle),$$
$$|p_z\rangle = |1, 0\rangle. \tag{4.9}$$

Hence, this yields

$$L_x|p_x\rangle = \frac{1}{2}\frac{1}{\sqrt{2}}(L_+ + L_-)(-|1, 1\rangle + |1, -1\rangle)$$
$$= \frac{1}{2}(-|1, 0\rangle + |1, 0\rangle) = 0 \tag{4.10}$$

Similarly, we find

$$L_y|p_x\rangle = -\frac{i}{2}(L_+ - L_-)\frac{1}{\sqrt{2}}(-|1, 1\rangle + |1, -1\rangle)$$
$$= -\frac{i}{2}2|1, 0\rangle$$
$$= -i|p_z\rangle. \tag{4.11}$$

As a result, we obtain $\langle p_z|\boldsymbol{\sigma} \cdot \mathbf{L}|p_x\rangle = \langle p_z| - i\sigma_y|p_z\rangle = -i\sigma_y$, where we also used $\langle p_z|L_z|p_x\rangle = 0$.

The exact value of the on-site coupling parameters ξ_{p1}, ξ_{p2}, ξ_{sp1}, and ξ_{sp2} may be obtained by fitting the band structure obtained from Eq. (4.4) to first-principles calculations. Note that ξ_{sp1} and ξ_{sp2} are

both linear in E. Furthermore, the prime (double prime) in the summation indicates that the sum is taken over atoms located at the edges (vertices). Since the p_z-orbitals correspond to the low-energy states, we can use the approximation scheme outlined in the App. A, which yields

$$H_{z,v+e}^{\text{eff}} = S^{-1/2}(H_z - H_{SOC}^{z,\sigma}H_\sigma^{-1}(H_{SOC}^{z,\sigma})^\dagger)S^{-1/2},$$
$$= S^{-1/2}H_z S^{-1/2} - S^{-1/2}H_{SOC}^{z,\sigma}H_\sigma^{-1}(H_{SOC}^{z,\sigma})^\dagger S^{-1/2}. \tag{4.12}$$

In the second line, we have split the Hamiltonian in two parts. Note that the first term can neither lead to the opening of a gap, nor shift the position of the Dirac cones. This follows from the relation $\det\left[S^{-1/2}H_z S^{-1/2}\right] = \det H_z/\det S$. Hence, as for the first term, we may simply set $S = \mathbb{I}$. With respect to the second term, we use

$$S^{-1/2} = \mathbb{I} - H_{SOC}^{z,\sigma}H_\sigma^{-1}(H_{SOC}^{z,\sigma})^\dagger/2 + \ldots \tag{4.13}$$

This shows that if we use $\mathbb{I}$, we neglect contributions proportional to ξ^4 in the second term, with $\xi \in \{\xi_{sp1}, \xi_{sp2}, \xi_{p1}, \xi_{p2}\}$. This is allowed, since all ξ's are very small compared to the other hopping parameters. As a result, we approximate the effective Hamiltonian by

$$H_{z,v+e}^{\text{eff}} = H_z - H_{SOC}^{z,\sigma}H_\sigma^{-1}(H_{SOC}^{z,\sigma})^\dagger. \tag{4.14}$$

Since in this approximation the Hamiltonian is given in momentum-space, we need to perform an inverse Fourier transformation to obtain a real-space TB Hamiltonian. Using that the hoppings which form the bonds are the largest energies in the system, we can simplify H_σ^{-1}. First of all, we use sp, sp^2, and p hybrid orbitals, shown in Figs. 4.1(a), (b), and (c), respectively. In this model, we only take into account the on-site energies ε_i and hoppings $V_5, \ldots, V_9$, as well as the NN hoppings $V_1, \ldots, V_4$ which form a bond and neglect all other hopping processes, yielding

$$H_\sigma = H_{\sigma,\text{onsite}} + H_{\sigma,\text{NN}}. \tag{4.15}$$

If the on-site energies and hopping parameters of the hybrid orbitals are smalller than the NN-hopping parameters of the bonds, we may approximate the inverse matrix by

$$H_\sigma^{-1} \approx H_{\sigma,\text{NN}}^{-1} - H_{\sigma,\text{NN}}^{-1}H_{\sigma,\text{onsite}}H_{\sigma,\text{NN}}^{-1}. \tag{4.16}$$

This approximation is justified by the fact that the hybrid orbitals are mainly composed of p orbitals that have very small on-site energies. In this simple TB model, we find that

$$\left(H_{\sigma,\text{NN}}^{-1}\right)_{ij} = \begin{cases} 1/\left(H_{\sigma,\text{NN}}\right)_{ij}^* & \text{if } (H_{\sigma,\text{NN}})_{ij} \neq 0 \\ 0 & \text{if } (H_{\sigma,\text{NN}})_{ij} = 0. \end{cases} \tag{4.17}$$

This expression can easily be transformed to real space. The effective SOC Hamiltonian is then given by the second term on the RHS of Eq. (4.14) combined with Eq. (4.16),

$$H_{\text{SOC,eff}} = H_{SOC}^{z,\sigma}\left(H_{\sigma,\text{NN}}^{-1} - H_{\sigma,\text{NN}}^{-1}H_{\sigma,\text{onsite}}H_{\sigma,\text{NN}}^{-1}\right)(H_{SOC}^{z,\sigma})^\dagger. \tag{4.18}$$

Using the Hamiltonians $H_{SOC}^{z,\sigma}$, $H_{\sigma,\text{NN}}$, and $H_{\sigma,\text{onsite}}$ for α, β, and γ-graphyne, we obtain the SOC in real space

$$H_{\text{SOC,eff}}^\sigma = H_{\text{R}}^\sigma + H_{\text{I}}^\sigma + H_{\text{rest}}^\sigma, \tag{4.19}$$

where

$$H_{\text{R}}^\sigma = i \sum_{\langle i,j \rangle} \lambda_{R,ij}^\sigma p_{z,i}^\dagger \left(\boldsymbol{\sigma} \times \hat{\mathbf{d}}_{ij}\right) \cdot \hat{\mathbf{z}} p_{z,j}, \tag{4.20}$$

$$H_{\text{I}}^\sigma = i \sum_{\langle\langle i,j \rangle\rangle} \lambda_{I,ij}^\sigma v_{ij} p_{z,i}^\dagger \sigma_z p_{z,j}, \tag{4.21}$$

$\boldsymbol{\sigma} \cdot \boldsymbol{L}$	p_x	p_y	s
p_z	$-i\sigma_y$	$i\sigma_x$	0

Tab. 4.1: Matrix elements for $\boldsymbol{\sigma} \cdot \mathbf{L}$. Note that the Pauli matrices act in spin space.
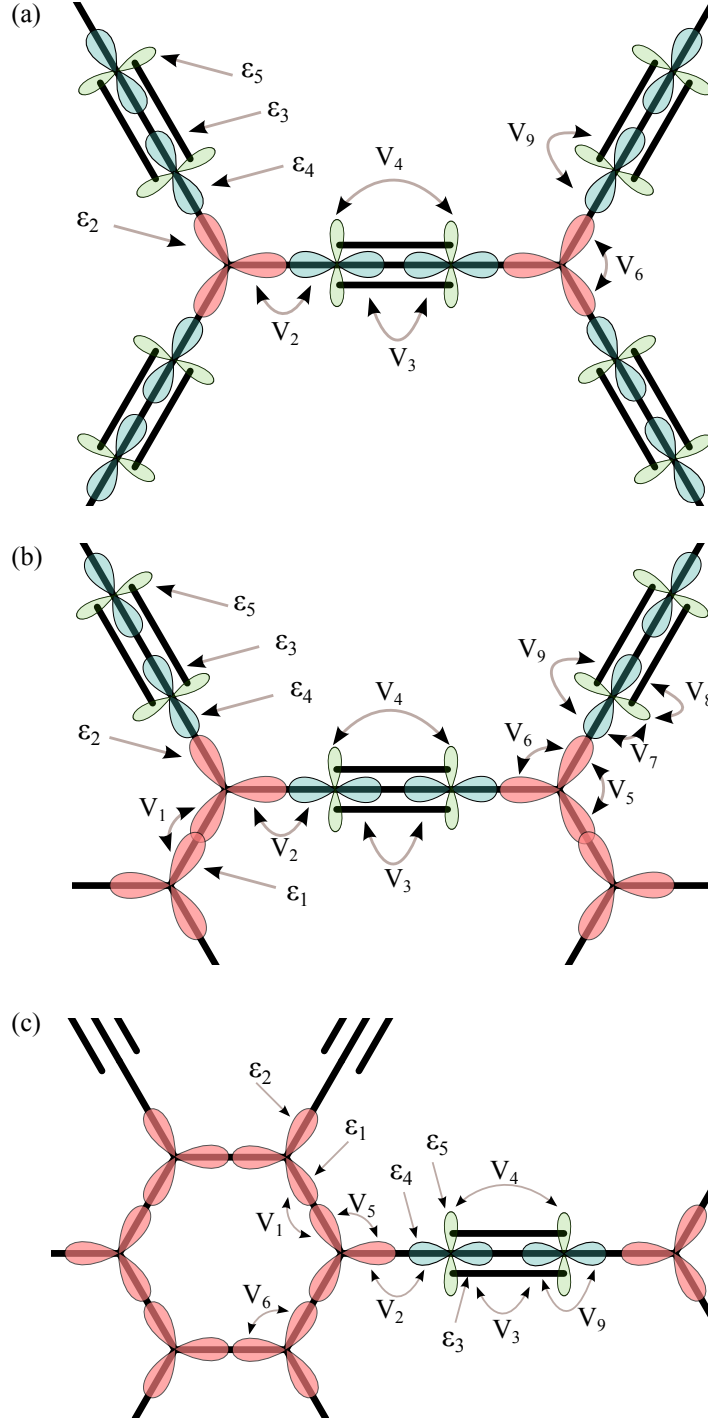
Fig. 4.1: Parameters used for the σ-TB models for α, β, and γ-graphyne, shown in panels (a), (b), and (c). The hopping parameters $V_1, \ldots, V_4$ correspond to NN hoppings, whereas $V_5, \ldots, V_9$ correspond to on-site hoppings, and $\varepsilon_1, \ldots, \varepsilon_5$ denote the on-site energies. Other hopping parameters have been set to zero.

and H_{rest} describes the NNN corrections to the Rashba SOC (which can be neglected), together with some very small spin-independent and thus irrelevant NN and NNN hoppings and on-site energies. In both expressions we have included position-dependent coupling constants $\lambda_{R,ij}^\sigma$ and $\lambda_{I,ij}^\sigma$, $\hat{\mathbf{d}}_{ij}$ is the unit vector pointing from site i to j, and $v_{ij} = +(-)$ if the hopping is (anti-)clockwise, and zero if it is along the acetylene bond. In total we need six different coupling parameters to completely describe

SOC in graphyne: three for Rashba ($\lambda_{R,i}^\sigma$) and three for the intrinsic SOC ($\lambda_{I,i}^\sigma$), with $i = 1, 2, 3$, corresponding to vertex-vertex, vertex-edge, and edge-edge hoppings, respectively. In Table 4.2 we give the expressions for these coupling parameters in terms of the σ hopping parameters, as obtained from Eqs. (4.20) and (4.21).

It turns out that for the three types of graphyne that we consider, we obtain Hamiltonians of the same form as in graphene, simply with adjusted coupling parameters. However, in β-graphyne there is an additional contribution to the intrinsic SOC Hamiltonian. In α- and γ-graphyne, each hopping along a straight path yields no contribution to the intrinsic SOC Hamiltonian, which is a consequence of the mirror symmetry through the acetylene bond in these systems. This symmetry is weakly broken in β-graphyne. As a result of this weak symmetry breaking in β-graphyne, we obtain a very small additional contribution to the intrinsic SOC Hamiltonian,

$$H_{\beta,4} = i\lambda_{I,4}^\sigma \sum_{\langle\langle i,j\rangle\rangle} w_{ij} p_{z,i}^\dagger \sigma_z p_{z,j}, \tag{4.22}$$

where $w_{ij} = +(-)$ if the hopping is along the acetylene bond going (anti-)clockwise with respect to the center of the unit-cell, and $\lambda_{I,4}^\sigma = \sqrt{2}\xi_{p1}\xi_{p2}V_7/(\sqrt{3}V_2V_4)$. Since V_7 is non-zero only in β-graphyne, this contribution is absent in α and γ graphyne. Furthermore, we would like to point out that in the TB models we used, we have neglected subdominant NN hoppings. However, the inclusion of these can lead to an NN intrinsic SOC term in the Hamiltonian. In β-graphyne this is generated by the NN hopping from the sp^2 orbitals to the p orbitals, whereas in γ-graphyne this is caused by the hopping between sp^2 orbitals which point in different directions. These contributions can easily be explained from the broken mirror symmetry through the acetylene bond in β-graphyne, and through the σ-bond forming the hexagon in γ-graphyne. Since these symmetries are only weakly broken, their effect will be very small.

In Ref. [33], the effect of intrinsic SOC on the dispersion relation in graphyne was calculated from first principles. The obtained gap of 0.014 meV in α-graphyne is rather large as compared to graphene, and may be attributed to the inhomogeneity in the charge distribution around the acetylene bond. By fitting the gap obtained within the TB model to the one derived from first-principles calculations, we find that for α-graphyne $\lambda_{I,3}^\sigma \approx 0.041\text{meV}$. In α-graphyne $V_6 = \epsilon_s/3 \approx 2.67\text{eV}$, and a rough estimate yields $V_2 \approx 5 - 10\text{eV}$. This leads to an approximate lower bound for $\xi_{p1} \approx 12.6\text{meV}$, whereas in graphene $\xi_p \approx 2.8\text{meV}$. In addition, around the vertices the charge is rather homogenously distributed, and thus we expect that the coupling ξ_{p2} is roughly of the same size as in graphene, $\xi_{p2} \approx 2.8\text{meV}$.

Inspection of Table 4.2 clearly shows that the parameters corresponding to the Rashba coupling parameters are proportional to $\xi_{sp}\xi_p/V_i$, where V_i is one of the NN hopping parameters. This is expected, since the Rashba terms arise from

$$H_E^{z,\sigma} H_{\sigma,\text{NN}}^{-1} (H_L^{z,\sigma})^\dagger + h.c., \tag{4.23}$$

where the matrix $H_E^{z,\sigma}$ contributes a factor ξ_{sp}, H_{NN} yields a factor V_i, and $H_L^{z,\sigma}$ a factor ξ_p. Note that V_4 does not appear in Table 4.2; this can be understood from the matrix structure of Eq. (4.23). Terms from right to left in this expression correspond to *(i)* the on-site hopping from a p_z orbital to a hybrid orbital, *(ii)* subsequent hopping between two NN hybrid orbitals, and *(iii)* the on-site hopping from an sp or sp^2 hybrid orbital to a p_z orbital due to the electric field. Since V_4 is responsible for the hopping between two NN p orbitals, it does not contribute to this process. Notice also that $\varepsilon_1 - \varepsilon_5$ and $V_5 - V_9$ do not appear here because they correspond to on-site energies and hoppings, respectively.

The intrinsic SOC arises from

$$H_L^{z,\sigma} H_{\sigma,\text{NN}}^{-1} H_{\sigma,\text{onsite}} H_{\sigma,\text{NN}}^{-1} (H_L^{z,\sigma})^\dagger + h.c., \tag{4.24}$$

hence, the coupling parameters are all of the form $\xi_p^2 AB^{-2}$, where $A \in \{V_5, \ldots, V_9, \varepsilon_1, \ldots, \varepsilon_5\}$ comes from $H_{\sigma,\text{onsite}}$ and $B \in \{V_1, \ldots, V_4\}$ comes from $H_{\sigma,\text{NN}}$. However, Table 4.2 clearly shows that actually

σ	α, β, and γ
$\lambda_{R,1}^{\sigma}$	$2\sqrt{2}\xi_{2sp}\xi_{2p}/(3V_1)$
$\lambda_{R,2}^{\sigma}$	$(\sqrt{2}\xi_{sp1}\xi_{p2} + \xi_{sp2}\xi_{p1})/(\sqrt{6}V_2)$
$\lambda_{R,3}^{\sigma}$	$\xi_{1sp}\xi_{1p}/V_3$
$\lambda_{I,1}^{\sigma}$	$V_6\xi_{p,2}^2/(\sqrt{3}V_1^2)$
$\lambda_{I,2}^{\sigma}$	$V_5\xi_{p,2}\xi_{p,1}/(2V_1V_2)$
$\lambda_{I,3}^{\sigma}$	$\sqrt{3}V_6\xi_{p1}^2/(4V_2^2)$

Tab. 4.2: SOC parameters for the three types of graphyne arising from the σ-orbitals.

none of these parameters is proportional to an onsite energy ε_i. The reason for this is that if we read Eq. (4.24) from right to left, we find that *(i)* the first matrix leads to the hopping from a p_z orbital to one of the hybrid orbitals due to the SOC, *(ii)* then $H_{\sigma,\mathrm{NN}}^{-1}$ leads to the hopping to a NN hybrid orbital, *(iii,a)* the term $H_{\sigma,\mathrm{onsite}}$ can lead to the onsite hopping to another hybrid orbital; this contributes a factor V_j with $j = 5, \ldots, 9$, or *(iii,b)* it can simply stay on the same orbital which would contribute a factor ε_i. However, this last scenario leads then subsequently to the hopping to the hybrid orbital where one started, therefore there are no terms proportional to ε_i. The parameter V_8 is also absent in Table 4.2. This can be understood by analyzing the hopping process proportional to V_8: starting from the p_z orbital a^1 (see Fig. C.2 and Fig. 4.1), we then find that

1. $(H_L^{z,\sigma})^\dagger$ contributes a factor proportional to σ_y, and leads to the hopping to state a_1^1

2. $H_{\sigma,\mathrm{NN}}^{-1}$ contributes a factor V_3^{-1}, and leads to the hopping to state b_1^1

3. $H_{\sigma,\mathrm{onsite}}$ contributes a factor V_8, and leads to the hopping to state b_3^1

4. $H_{\sigma,\mathrm{NN}}^{-1}$ contributes a factor V_3^{-1}, and leads to the hopping to state a_1^1

5. $(H_L^{z,\sigma})^\dagger$ contributes a factor proportional to σ_y, and leads to the hopping to p_z-orbital a^1.

Hence, the term proportional to V_8 does not lead to a NNN hopping process, but gives rise to an onsite energy, which can be neglected. Concerning the absence of V_9 and V_3 in Table 4.2, we would like to point out that this term does actually lead to a NNN hopping in Eq. (4.24) that is, however, spin-independent. This can be seen from the fact that from right to left again, for this process the hybrid orbital to which the p_z orbital hops points in the same direction as the hybrid orbital from which it hops to the NNN p_z orbital. To illustrate this process, we consider the hopping from A to b^1 via V_9 and V_3 (see Fig. C.2 and Fig. 4.1)

1. $(H_L^{z,\sigma})^\dagger$ contributes a factor proportional to σ_y, and leads to the hopping to state A_2

2. $H_{\sigma,\mathrm{NN}}^{-1}$ contributes a factor $1/V_2$, and leads to the hopping to state a_2^1

3. $H_{\sigma,\mathrm{onsite}}$ contributes a factor V_9, and leads to the hopping to state a_1^1

4. $H_{\sigma,\mathrm{NN}}^{-1}$ contributes a factor $1/V_3$, and leads to the hopping to state b_1^1

5. $(H_L^{z,\sigma})^\dagger$ contributes a factor proportional to σ_y, and leads to the hopping to state b^1.

Since the initial and final hoppings are both proportional to σ_y, we find that the combination is proportional to $\sigma_y \cdot \sigma_y = \mathbb{I}$, hence, it does not lead to a spin-dependent hopping. Note that the parameters V_4 and V_7 appear in Eq. (4.22).

4.3 Spin-orbit coupling generated by the d-orbitals.

The preceding discussion showed that the coupling parameters for the intrinsic SOC are of second order in ξ_{p1} and (or) ξ_{p2}. In Ref. [23], it was shown that the gap opening in graphene is actually due to intrinsic SOC hosted by the d_{xz} and d_{yz} orbitals. The reason is that the intrinsic SOC due

d	α, β, and γ
$\lambda_{I,1}^d$	$\sqrt{3}V_{dp1}^2\xi_d/2\epsilon_d^2$
$\lambda_{I,2}^d$	$\sqrt{3}V_{dp1}V_{dp2}\xi_d/2\epsilon_d^2$
$\lambda_{I,3}^d$	$\sqrt{3}V_{dp2}^2\xi_d/2\epsilon_d^2$

Tab. 4.3: SOC parameters for the three types of graphyne arising from the d-orbitals.

to the d orbitals is of first order in the intrinsic SOC parameter for the d-orbitals, ξ_d. To include the contributions stemming from the d-orbitals, we write down the TB Hamiltonian, with the hopping between the p_z, d_{xz}, and d_{yz} orbitals included, and the ISO-coupling among the d-orbitals

$$H = H_z + H_{zd} + H_{zd}^\dagger + H_d + H_L^d, \tag{4.25}$$

where H_z describes the hopping between the p_z orbitals, H_{zd} describes the hopping from the d orbitals to the p_z orbitals, H_d is the TB Hamiltonian describing the d_{xz} and d_{yz} orbitals, and H_L^d describes the intrinsic SOC between the d_{xz} and d_{yz} orbitals. The latter term is given by

$$H_L^d = i\xi_{d1}\sum_i{}' d_{yz,i}^\dagger \sigma_z d_{xz,i} + i\xi_{d2}\sum_i{}'' d_{yz,i}^\dagger \sigma_z d_{xz,i} + h.c. \tag{4.26}$$

The Hamiltonian H_{zd} is given by

$$H_{zd} = \sum_{\langle i,j\rangle} V_{dp,ij} p_{z,i}^\dagger (n_{ij,x}d_{xz,j} + n_{ij,y}d_{yz,j}), \tag{4.27}$$

here n_{ij} denotes the unit vector pointing from site i to j and $V_{dp,ij} = V_{dp,k}$ with $k = 1, 2, 3$ depending whether n_{ij} points from vertex to vertex, vertex to edge or edge to edge, respectively. Again, we use the approximation scheme from App. A that leads to the following effective Hamiltonian

$$H_{z,v+e}^{\text{eff}} = S^{-1/2}\left(H_z - H_{zd}\left(H_L^d + H_d\right)^{-1}H_{dz}\right)S^{-1/2}. \tag{4.28}$$

Following the same reasoning as before we simply set $S = \mathbb{I}$. Since ξ_{d1} and ξ_{d2} are very small, we may approximate $\left(H_L^d + H_d\right)^{-1} \approx H_d^{-1} - H_d^{-1}H_L^d H_d^{-1}$. Notice that this explains why the intrinsic SOC generated by the d-orbitals is first order in ξ_d. As a result, the effective intrinsic SOC Hamiltonian due to the d-orbitals is given by

$$H_{\text{SOC,eff}} = H_{zd}H_d^{-1}H_L^d H_d^{-1}H_{dz}. \tag{4.29}$$

Because of the large on-site energies of the d orbitals ε_d, we may approximate $H_d^{-1} \approx \varepsilon_d^{-1}\mathbb{I}$. Therefore, Eq. (4.29) reduces to

$$H_{\text{SOC,eff}} = H_{zd}H_L^d H_{zd}^\dagger/\varepsilon_d^2. \tag{4.30}$$

Using the Hamiltonians H_L^d and H_{zd}, we finally obtain the intrinsic SOC Hamiltonian due to the d-orbitals,

$$H_I^d = i\sum_{\langle\langle i,j\rangle\rangle} \lambda_{I,ij}^d v_{ij} p_{z,i}^\dagger \sigma_z p_{z,j}, \tag{4.31}$$

where $v_{ij} = (+)-$ if the hopping is (anti-)clockwise. As for the σ-orbitals, we will need three different coupling parameters $(\lambda_{I,i}^d)$ to completely describe intrinsic SOC; the labeling used is the same as for the σ-orbitals. The coupling parameters are given in Table 4.3. Note that the expressions for the SOC parameters due to the d-orbitals and due to the σ-orbitals have the same sign. Therefore, the intrinsic SOC is governed by the parameters $\lambda_{I,j} = \lambda_{I,j}^\sigma + \lambda_{I,j}^\sigma$. As a result, the inclusion of d-orbitals increases the effect of SOC in graphynes.

SOC	α, β, and γ
$\tilde{\lambda}_{\mathrm{I}}^{\alpha}$	$\lambda_{I,3} t_2^2/(t_3^2 + 3t_2^2)$
$\lambda_{\mathrm{I,ext}}^{\beta}$	$-\lambda_{I,2} t_2 t_3/(t_3^2 + 2t_2^2)$
$\lambda_{\mathrm{I,ext}}^{\gamma}$	$-\lambda_{I,2} t_3 t_2/(t_2^2 + t_3^2)$
$\lambda_{\mathrm{I,int}}^{\beta}$	$\lambda_{I,3} t_2^2/(t_3^2 + 2t_2^2)$
$\lambda_{\mathrm{I,int}}^{\gamma}$	$\lambda_{I,1} t_3^2/(t_2^2 + t_3^2)$
$\tilde{\lambda}_{\mathrm{R}}^{\alpha}$	$2\lambda_{R,2} t_2 t_3/(t_3^2 + 3t_2^2) + \lambda_{R,3} t_2^2/(t_3^2 + 3t_2^2)$
$\lambda_{\mathrm{R,ext}}^{\beta}$	$\lambda_{R,1} t_3^2/(t_3^2 + 2t_2^2)$
$\lambda_{\mathrm{R,ext}}^{\gamma}$	$2\lambda_{R,2} t_2 t_3/(t_3^2 + t_2^2) + \lambda_{R,2} t_2^2/(t_3^2 + t_2^2)$
$\lambda_{\mathrm{R,int}}^{\beta}$	$-2\lambda_{R,2} t_2 t_3/(t_3^2 + 2t_2^2) - \lambda_{R,3} t_2^2/(t_3^2 + 2t_2^2)$
$\lambda_{\mathrm{R,int}}^{\gamma}$	$\lambda_{R,1} t_3^2/(t_2^2 + t_3^2)$

Tab. 4.4: SOC parameters for the effective TB models.

4.4 Spin-orbit coupling Hamiltonians in the two-site and six-site model

The SOC Hamiltonians that we obtained are all given in terms of the full TB Hamiltonian. The next step is to integrate out the high-energy orbitals to obtain SOC Hamiltonians that can be used in the effective models introduced in Chapter 3. In general, the effective Hamiltonian reads

$$H_{z,v}^{\mathrm{eff}} = S^{-1/2} \left(H_{vv} - H_{ve} H_{ee}^{-1} H_{ve}^{\dagger} \right) S^{-1/2}, \tag{4.32}$$

where H_{vv} (H_{ee}) describe the orbitals at the vertices (edges), and H_{ve} mixes them. In order to incorporate SOC in this description, we write each matrix as the sum of a spin-independent part, denoted by a tilde, and a part describing the SOC, denoted by the subscript SOC. Because the SOC parameters are very small compared to the other hopping energies, we may expand Eq. (4.32) up to first order in the SOC parameters. One then readily obtains

$$S^{-1/2} = (\tilde{S} + S_{SOC})^{-1/2} \approx \tilde{S}^{-1/2} - \frac{1}{2}\tilde{S}^{-3/2} S_{SOC}, \tag{4.33}$$

where

$$S_{SOC} = H_{lh,SOC} \tilde{H}_{hh}^{-2} \tilde{H}_{lh}^{\dagger} - \tilde{H}_{lh} \tilde{H}_{hh}^{-2} H_{hh,SOC} \tilde{H}_{hh}^{-1} \tilde{H}_{lh}^{\dagger} + h.c. \tag{4.34}$$

However, if we simply set $S = \tilde{S}$ we do not miss any gap openings or shifts in the positions of the Dirac cones. Hence, we approximate Eq. (4.32) by

$$H_{z,v}^{\mathrm{eff}} \approx \tilde{S}^{-1/2} \left(H_{vv} - H_{ve} H_{ee}^{-1} H_{ve}^{\dagger} \right) \tilde{S}^{-1/2}. \tag{4.35}$$

As a result, we find

$$H_{\mathrm{eff}} \approx \tilde{H}_{\mathrm{eff}} + H_{SOC}, \tag{4.36}$$

where $H_{SOC} = H_{1,SOC} + H_{2,SOC} + H_{3,SOC}$, with

$$H_{1,SOC} = \tilde{S}^{-1/2} H_{vv,SOC} \tilde{S}^{-1/2}, \tag{4.37}$$

$$H_{2,SOC} = -\tilde{S}^{-1/2} H_{ve,SOC} \tilde{H}_{ee}^{\dagger} \tilde{H}_{ve}^{\dagger} \tilde{S}^{-1/2} + h.c., \tag{4.38}$$

$$H_{3,SOC} = \tilde{S}^{-1/2} \tilde{H}_{ve} \tilde{H}_{ee}^{-1} H_{ee,SOC} \tilde{H}_{ee}^{-1} \tilde{H}_{ve}^{\dagger}. \tag{4.39}$$

By performing these calculations for α-graphyne we obtain,

$$H_{R,\alpha} = i\lambda_R \sum_{\langle i,j \rangle} p_{z,i}^{\dagger} \left(\boldsymbol{\sigma} \times \hat{\mathbf{d}}_{ij} \right) \cdot \hat{\mathbf{z}} p_{z,j}, \tag{4.40}$$

$$H_{I,\alpha} = i\lambda_I \sum_{\langle\langle i,j \rangle\rangle} v_{ij} p_{z,i}^{\dagger} \sigma_z p_{z,j}, \tag{4.41}$$

which are the standard SOC Hamiltonians as used for graphene. The results for β and γ graphyne are slightly different than for graphene, since now we have to distinguish between the inter and intra-unit cell SOC. We refer to the inter-unit cell SOC as external SOC, and to the intra unit cell SOC as internal SOC. The form of the SOC Hamiltonians is however unchanged as compared to graphene,

$$H_{R,\beta/\gamma} = i\lambda_{\mathrm{R,int}} \overset{.}{\underset{\langle i,j \rangle}{\sum}} p_{z,i}^{\dagger} \left(\boldsymbol{\sigma} \times \hat{\mathbf{d}}_{ij} \right) \cdot \hat{\mathbf{z}} p_{z,j} + i\lambda_{\mathrm{R,ext}} \overset{..}{\underset{\langle i,j \rangle}{\sum}} p_{z,i}^{\dagger} \left(\boldsymbol{\sigma} \times \hat{\mathbf{d}}_{ij} \right) \cdot \hat{\mathbf{z}} p_{z,j}, \tag{4.42}$$

$$H_{I,\beta/\gamma} = i\lambda_{\mathrm{I,int}} \overset{.}{\underset{\langle\langle i,j \rangle\rangle}{\sum}} v_{ij} p_{z,i}^{\dagger} \sigma_z p_{z,j} + i\lambda_{\mathrm{I,ext}} \overset{..}{\underset{\langle\langle i,j \rangle\rangle}{\sum}} v_{ij} p_{z,i}^{\dagger} \sigma_z p_{z,j}. \tag{4.43}$$

Here, the single (double) dot indicates that the sum is taken over sites within the same (belonging to different) unit cells. In Table 4.4 we have listed the expression for the SOC hopping parameters.

5. EFFECTS OF SPIN-ORBIT COUPLING IN GRAPHYNES

5.1 Spin-orbit coupling in α-graphyne

Since α-graphyne can effectively be described by the same Hamiltonian as graphene, the SOC has the same effect. The Rashba SOC leads to trigonal warping and lifts the spin-degeneracy[34, 35], see also Fig. 5.1(a). The intrinsic SOC opens a topologically non-trivial gap, but respects the spin degeneracy, see Fig. 5.1(b). When both Rashba and intrinsic SOC are present, the spin-degeneracy is lifted, the electron-hole symmetry is broken, and the Rashba SOC tends to close the gap induced by the intrinsic SOC. The main difference comparing to graphene is the reduced Fermi velocity and the larger band gap due to the stronger intrinsic SOC in graphynes.

5.2 Internal and external spin-orbit coupling

As shown in Chapter 3, both β and γ graphyne can be described in terms of the same six-site model, and Eqs. (3.4) and (3.6) can be rewritten in a short-hand notation as

$$H_0 = t_{\text{int}} \sum_{\langle i,j \rangle} \dot{p}_{z,i}^\dagger p_{z,j} + t_{\text{ext}} \sum_{\langle i,j \rangle} \ddot{p}_{z,i}^\dagger p_{z,j}.$$ (5.1)

The band structure obtained from this Hamiltonian exhibits six Dirac cones at the line connecting the Γ and M points if the condition $-2 < t_{\text{ext}}/t_{\text{int}} < -1$ is satisfied. This is realized for β but not for γ-graphyne, see Figs. 3.3(b) and 3.3(c). We show below that the intrinsic SOC can open a non-trivial gap
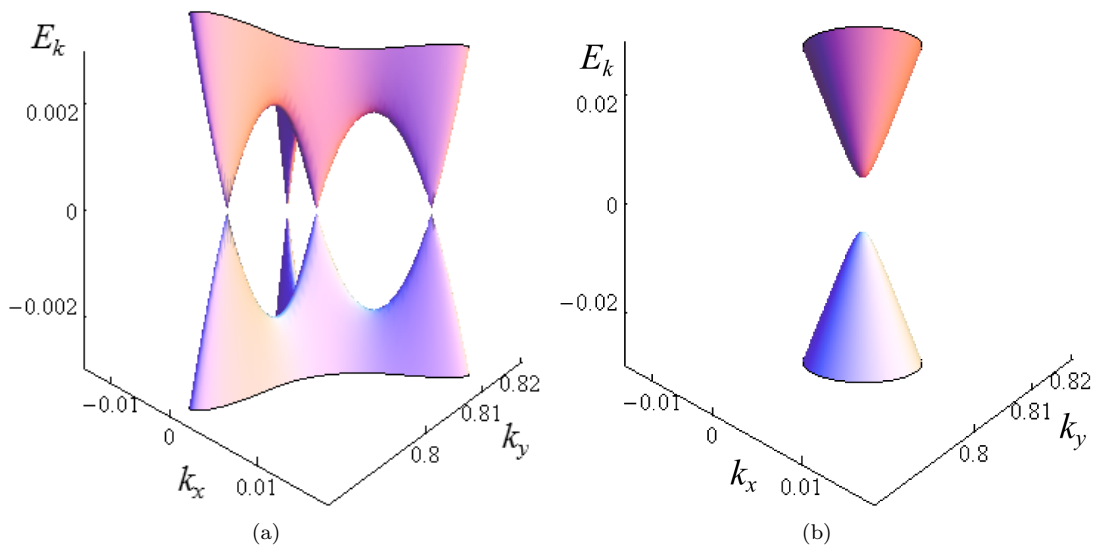

Fig. 5.1: Band structure of α-graphyne with SOC, zoomed in on the K point. (a)$\lambda_I = 0$eV and $\lambda_R = 0.5$eV. (b) $\lambda_I = 0.05$eV and $\lambda_R = 0$eV.

in β-graphyne, whereas the Rashba SOC can be used to open or close a trivial gap in β and γ-graphyne. In Eqs. (4.42) and (4.43), we have made a distinction between external and internal SOC. To obtain a better understanding of the effect of both terms, we discuss them separately in the following.

5.2.1 Internal Rashba spin-orbit coupling

The internal Rashba SOC leads to very interesting phases characterized by the presence of Dirac cones at different points in the BZ. First, we discuss the regime that applies to β-graphyne, after which we consider the regime that describes γ-graphyne. At the end we also comment on the other regimes. Part of the phase-diagram is shown in Fig. 5.2. The red dashed line therein corresponds to β-graphyne, whereas the blue solid line corresponds to γ-graphyne.

For the regime $-1.19 < t_{ext}/t_{int} < -1$ that applies to β-graphyne, the system goes through three different phases. Initially, the internal Rashba SOC splits each Dirac cone into a pair of Dirac cones located at a line perpendicular to the line connecting the Γ-M points, see region I in Fig. 5.2. Upon increasing the coupling these pairs move towards the boundary of the BZ where they eventually annihilate with another pair at the line connecting K and K' points. As a result, the system system becomes gapped, see region II in Fig. 5.2. If the internal Rashba SOC is even further increased, the system undergoes another phase transition, with six new pairs of Dirac cones emerging alon the lines connecting Γ and M points, see region III in Fig. 5.2.

Next, we discuss the regime $-1 < t_{ext}/t_{int} < -0.8$ that describes γ-graphyne. The system is initially gapped, see also region II in Fig. 5.2. However, when the internal Rashba SOC is sufficiently large, six pairs of Dirac cones appear along the lines connecting Γ-M points, see region III in Fig. 5.2.

Having studied the regimes that apply to β- and γ-graphyne, we now consider the regime for which $-1.26 < t_{ext}/t_{int} < -1.19$. As for β-graphyne, initially the internal Rashba SOC splits each Dirac cone into a pair of Dirac cones located along a line perpendicular to Γ-M, see region I in Fig. 5.2. When the internal Rashba SOC is even further increased six additional pairs of Dirac cones emerge along the line connecting Γ-M, see region IV in Fig. 5.2. Eventually, when the coupling is even further increased the

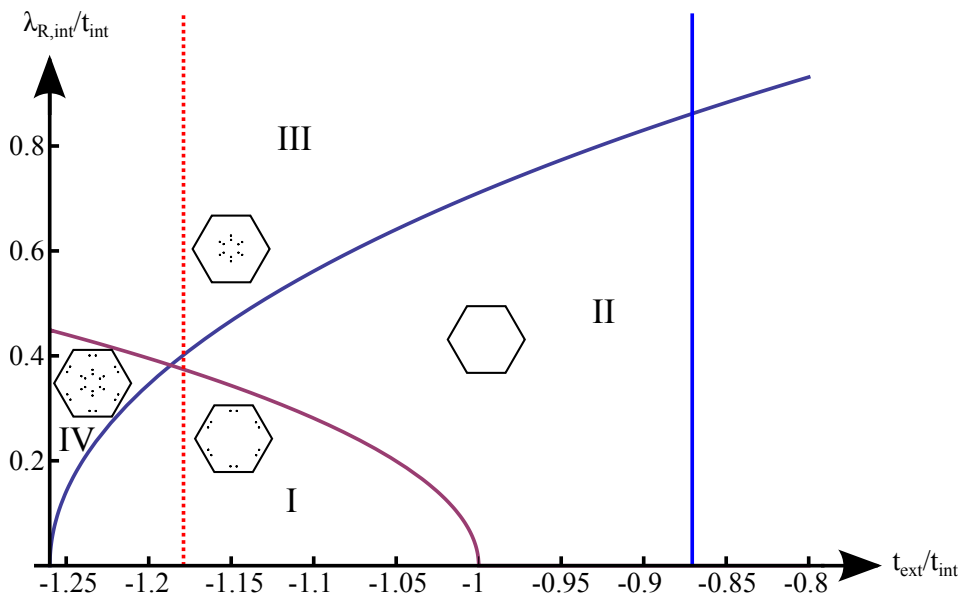*Fig. 5.2:* Phase diagram for the effective Hamiltonian (5.1) with internal Rashba SOC . In region I the system exhibits 12 Dirac cones, region II corresponds to the gapped phase, region III corresponds to the system where only pairs of Dirac cones along the line Γ-M are present, and region IV corresponds to a system with six pairs of cones along the line Γ-M and six pairs on lines perpendicular to Γ-M.
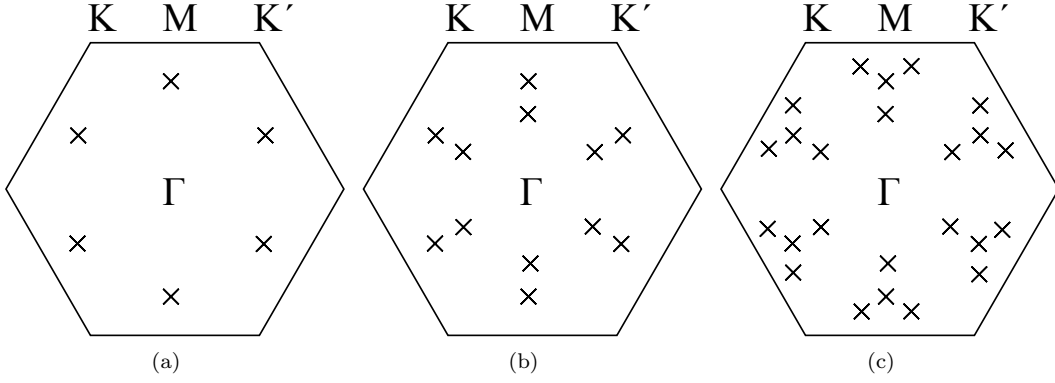
Fig. 5.3: Sketches of the phases corresponding to the regime $t_{ext}/t_{int} < -2^{1/3}$. Each cross denotes a Dirac cone and we have taken $t_{ext}/t_{int} = -1.3$. Panel (a) displays the BZ for $\lambda_{R,int} = \lambda_{R,ext} = 0$, panel (b) displays the BZ for $\lambda_{R,int}/t_{int} = 0.1$ or $\lambda_{R,ext}/t_{int} = 0.1$, and panel (c) displays the BZ for $\lambda_{R,int}/t_{int} = .4$ or $\lambda_{R,ext}/t_{int} = 0.8$.

six pairs of Dirac cones located at lines perpendicular to the Γ-M points annihilate at the boundary of the BZ, see region III in Fig. 5.2. Finally, when $-2 < t_{ext}/t_{int} < -1.26$ another curious phenomenon occurs (not shown in Fig. 5.2). First, each Dirac cone splits into a pair along the connecting the Γ and M points, see Figs. 5.3(a) and 5.3(b). When the coupling is even further increased, each of the cones closest tho the M points splits into three cones, see Fig. 5.3(c) for a sketch of the situation.

5.2.2 External Rashba spin-orbit coupling

As for the internal Rashba SOC, we first discuss the regimes that apply to β- and γ-graphyne. At the end we shortly comment on the other regimes. The relevant phase-diagram is shown in Fig. 5.4, where again the red dashed line corresponds to β-graphyne and the blue solid line corresponds to γ-graphyne.
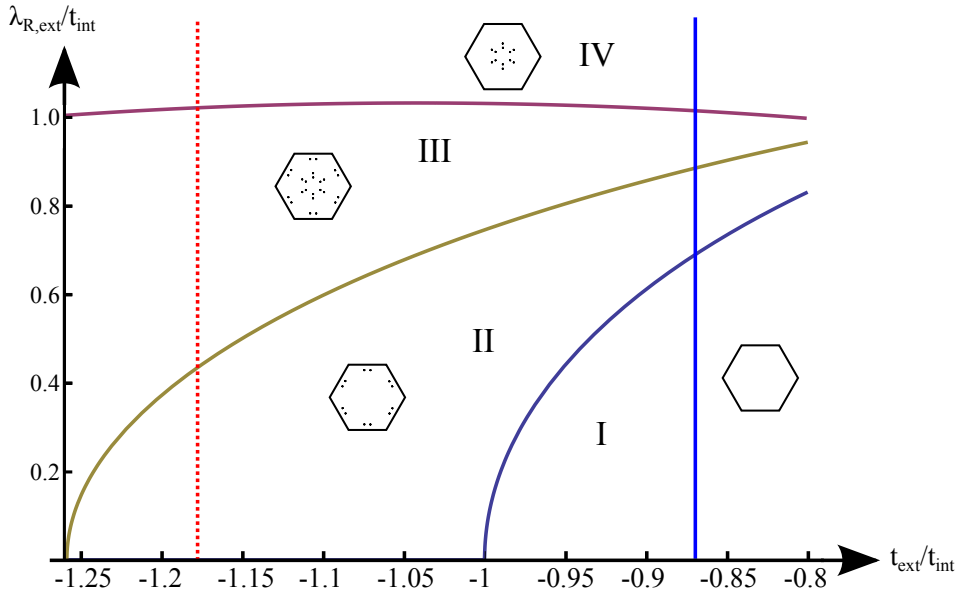
Fig. 5.4: Phase diagram for the effective model (5.1) with external Rashba SOC. Region I corresponds to a gapped system, region II exhibits six pairs of Dirac cones along a line perpendicular to the line connecting Γ and M, region III exhibits six Dirac cones along a line perpendicular to the line connecting Γ and M, and six pairs of Dirac cones along the lines connecting Γ and M, and region IV shows the system with only six pairs of Dirac cones along the line connecting Γ and M.

First, we consider the regime $-1.26 < t_{ext}/t_{int} < -1$ that applies to β-graphyne. Initially, the system exhibits six Dirac cones along the lines connecting Γ and M points. As the external Rashba SOC is switched on, each of these Dirac cones splits into a pair of Dirac cones located along lines perpendicular to the line connecting Γ and M points, see region II in Fig. 5.4. At an intermediate value of the external Rashba SOC parameter six additional pairs of Dirac cones emerge located along the lines connecting Γ and M points. When the coupling is even further increased the pairs perpendicular to the lines connecting the Γ and M points eventually merge and vanish along the lines connecting the K (K') and Γ points, see region IV in Fig. 5.4.

We now move on to discuss the case $-1 < t_{ext}/t_{int} < -0.8$, the relevant regime for γ-graphyne. For $-1 < t_{ext}/t_{int}$ the system is gapped, and remains to be such for small values of the external Rashba SOC, see region I in Fig. 5.4. However, at an intermediate value of the coupling six pairs of Dirac cones emerge along the line connecting K and K' points, see region II in Fig. 5.4. For increasing values of the coupling parameter γ-graphyne undergoes the same phase transitions as β-graphyne. Hence, subsequently it will enter region III and IV, see Fig. 5.4. Finally, in the regime $-2 < t_{ext}/t_{int} < -1$ (not shown in Fig. 5.4) the external Rashba SOC acts in the same way as the internal Rashba SOC does, see also Fig. 5.3.

5.2.3   Intrinsic spin-orbit coupling

Whereas the internal and external Rashba SOC lead to a qualitative difference in the band structure, such a difference is absent when studying the intrinsic SOC. It is found that if the system exhibits Dirac cones, $-2 < t_{\text{ext}}/t_{\text{int}} < -1$, both the internal and external intrinsic SOC open the gap located between the Γ and M points, see Fig. 5.5(a) and Fig. 5.5(b). However, if we combine internal and external intrinsic SOC, both the magnitudes and the signs of the couplings $\lambda_{\text{I,int}}$ and $\lambda_{\text{I,ext}}$ play an important role. It turns out that if both couplings have the same sign, the two contributions tend to cancel each
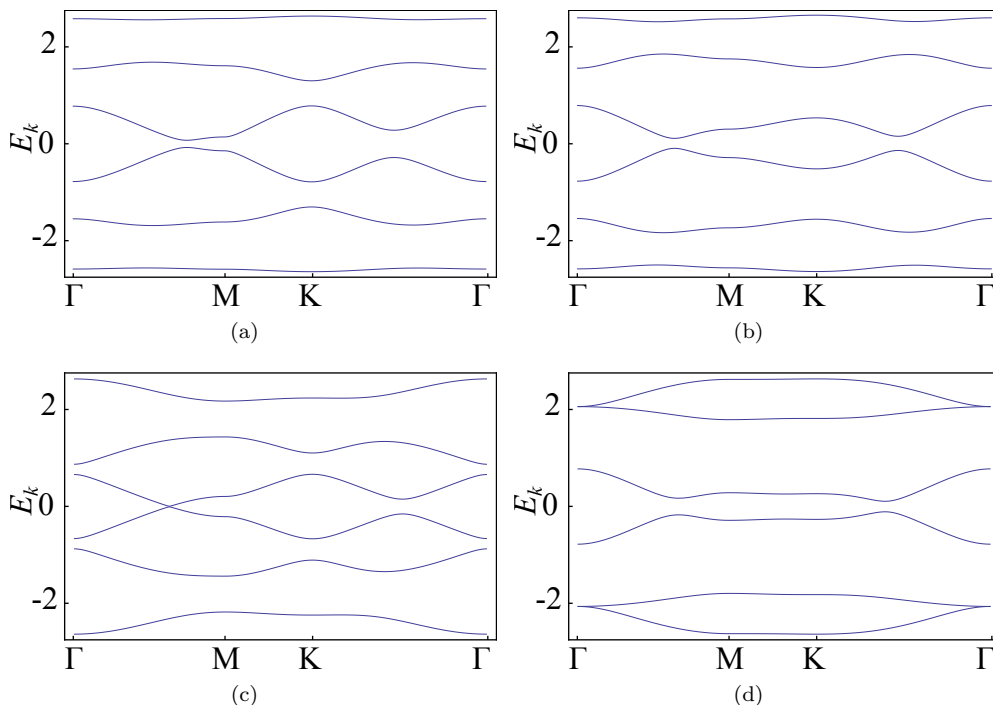
Fig. 5.5: Band structure for β-graphyne with different values of $\lambda_{\text{I,int}}$ and $\lambda_{\text{I,ext}}$, along the high-symmetry lines. (a) $\lambda_{\text{I,ext}} = 0.15$eV and $\lambda_{\text{I,int}} = 0$eV. (b) $\lambda_{\text{I,ext}} = 0$eV and $\lambda_{\text{I,int}} = 0.3$eV. (c) $\lambda_{\text{I,ext}} = 0.15$eV and $\lambda_{\text{I,int}} = 0.3$eV. (d) $\lambda_{\text{I,ext}} = 0.15$eV and $\lambda_{\text{I,int}} = -0.3$eV.

other, see Fig. 5.5(c). On the other hand, if both couplings have opposite sign the two contributions enhance the gap located at the line connecting Γ and M points, see Fig. 5.5.

Although at first it might be surprising that for opposite sign of the coupling parameters $\lambda_{\mathrm{I,int}}$ and $\lambda_{\mathrm{I,ext}}$ the gap is enhanced, this results from the fact that we have eliminated the p_z-orbitals located at the edges. For β-graphyne with orbitals at the edges included, the intrinsic SOC is governed by the coupling parameters $\lambda_{I,2}$ and $\lambda_{I,3}$ that have both the same sign, see Table 4.2. Then, if we eliminate the p_z-orbitals located at the edges, the intrinsic SOC is governed by the coupling parameters $\lambda_{\mathrm{I,int}}$ and $\lambda_{\mathrm{I,ext}}$. However, inspection of Table 4.4 shows that the coupling parameter describing the internal intrinsic SOC has an overall minus sign, whereas the external intrinsic SOC does not have it. Hence, a sign difference in the value of the parameters $\lambda_{\mathrm{I,int}}$ and $\lambda_{\mathrm{I,ext}}$ corresponds to the situation that in the full model containing both orbitals at edges and vertices the parameters $\lambda_{I,2}$ and $\lambda_{I,3}$ have the same sign.

5.3 Spin-orbit coupling in β-graphyne

As for graphene and α-graphyne, we find that the intrinsic SOC respects the spin degeneracy, but opens a gap, whereas the Rashba SOC lifts the spin degeneracy, but does not open a gap. If we include both terms, the spin-degeneracy is lifted, the electron-hole symmetry is broken and the Rashba SOC tends to close the gap produced by the intrinsic SOC. To study the precise effects of the Rashba SOC, we need to know the values of $\lambda_{\mathrm{R,ext}}$ and $\lambda_{\mathrm{R,int}}$. Since we do not know these values, we need to resort to some rough estimates. Inspection of Table 4.4 indicates that in β-graphyne the internal Rashba SOC dominates. This can be understood from the fact that the internal Rashba SOC arises from the hoppings through the acetylene bond. Since there are three as many possibilities to flip spin, one expects that this term dominates. However, irrespective of these precise values, we find that for small values of the Rashba SOC parameters the Dirac cones split into pairs along the direction perpendicular to the line connecting the Γ and M points (see region I in Fig. 5.2 and Fig. 5.6(a). Upon increasing the value $\lambda_{\mathrm{R,int}}$ each pair will move towards the boundary of the BZ where it eventually merges with another pair at the line connecting the K and K' points and vanishes (see region II in Fig. 5.2 and Figs. 5.6(b) and (c)). On the other hand, at an intermediate value of $\lambda_{\mathrm{R,int}}$ we find that a new pair of Dirac cones emerges along the line connecting the Γ and M points. It should be stressed that the order of these Lifshitz transitions depends greatly on the precise value of the hopping parameters, so when the external hopping parameter is larger, it is more likely that the additional pair emerges before the other pairs annihilate. In fact, as shown in Figs. 5.6(e)-(h), the external Rashba SOC alone creates precisely the effect previously described, therefore opening up the possibility to control the Lifshitz phase transitions with either of the two types of Rashba SOC allowed here.
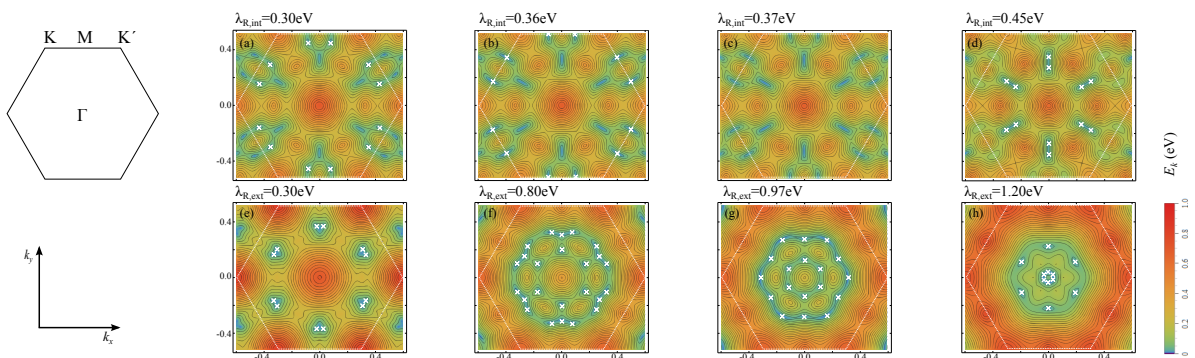
Fig. 5.6: Band structure in the presence of the Rashba SOC for $t_{\mathrm{ext}}/t_{\mathrm{int}} = -1.18$. The panels in the upper (lower) row display the Lifshitz transitions driven by the internal (external) Rashba SOC. The BZ is represented by a white line, the Dirac cones are labeled by white crosses in the plots. The high-symmetry points in the BZ are shown in the upper left panel and momentum is in units with the lattice constant set to one.
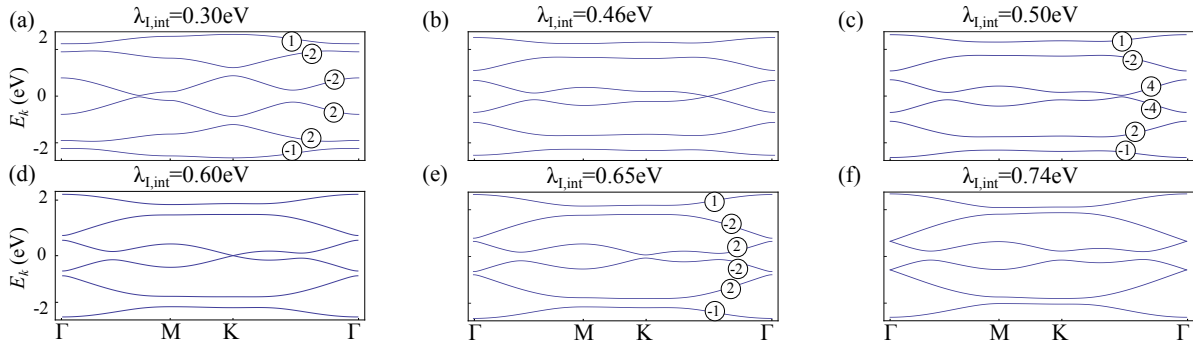
Fig. 5.7: The six panels display the band structure along high-symmetry lines for β-graphyne with the internal intrinsic SOC. The numbers in the circles denote the Chern numbers for the respective bands with spin up.

The intrinsic SOC leads to the formation of a topologically non-trivial bandgap in β-graphyne, see Fig. 5.7. The magnitude of this bandgap depends on the precise values of the intrinsic SOC parameters. We will specifically focus on the internal intrinsic SOC, which is governed by the parameter $\lambda_{\mathrm{I,int}}$. All Chern numbers have been calculated using lattice gauge theory, and the details are presented in Appendix E.5. For an infinitesimal value of this coupling, topologically non-trivial bands arise with the corresponding total Chern number at half-filling $C_\uparrow = 3$ for spin-up electrons [Fig. 5.7(a)], as opposed to graphene, where the intrinsic SOC produces $C_\uparrow = 1$. This value of the total Chern number in β-graphyne is a result of the following values of Chern numbers for the six bands $\{-1, 2, 2, -2, -2, 1\}$. Since the $\mathbb{Z}_2$ invariant is given by the parity of the spin Chern number, $\nu = C_\uparrow \pmod 2$, β-graphyne is a topologically nontrivial insulator. On the other hand, when TRS is broken, for instance by a weak magnetic field, the system turns into a Chern insulator with Chern number $C = 3$, implying that the Hall conductivity $\sigma_{\mathrm{Hall}} = 3e^2/h$, which differs from graphene where under the same circumstances $\sigma_{\mathrm{Hall}} = e^2/h$. Furthermore, at a critical value $\lambda_{\mathrm{I,int}}^{\mathrm{crit}} = 0.46\mathrm{eV}$, the bandgap at the Fermi level closes at the $\Gamma - K$ line [Fig. 5.7(b)] and reopens yielding the Chern numbers $\{-1, 2, -4, 4, -2, 1\}$, and $C_\uparrow = -3$ [Fig. 5.7(c)]. In addition, for even stronger internal intrinsic SOC, $\lambda_{\mathrm{I,int}} = 0.6\mathrm{eV}$, the bandgap closes at the K and K' points [Fig. 5.7(d)], and upon further increase of this coupling the system enters a topologically nontrivial insulating state with Chern numbers $\{-1, 2, -2, 2, -2, 1\}$ [Fig. 5.7(e)]. Finally, for $\lambda_{\mathrm{I,int}} = 0.74\mathrm{eV}$, the bandgap closes at the Γ point [Fig. 5.7(f)], and for even stronger $\lambda_{\mathrm{I,int}}$ an insulator with Chern numbers $\{-1, 1, -1, 1, -1, 1\}$ appears.

5.4   Spin-orbit coupling in γ-graphyne

Whereas β-graphyne exhibits Dirac cones and the Rashba SOC can destroy the Dirac behavior by opening a gap when the cones merge, we find that in γ-graphyne the situation is completely reversed. First of all, we note that in γ-graphyne the external SOC dominates, simply because by hopping through the acetylene bond one can flip the spin three times as many as compared to hopping though the single bond. The relevant phase-diagram is given in Fig. 5.4. This then tells us that when the coupling parameter $\lambda_{\mathrm{R,ext}}$ is increased, six new pairs emerge along the line connecting K and K', see region II in Fig. 5.4. When the coupling parameter is further increased, we find that six additional pairs of Dirac cones emerge on the line connecting Γ and M, see region III in Fig. 5.4. The intrinsic SOC leads to the deformation of the band structure, but does not open a non-trivial gap.

6. CONCLUSIONS AND OUTLOOK

In this thesis we studied the effects of spin-orbit coupling in graphynes using TB theory. In order to do so, we first reviewed the TB theory of graphynes without spin-orbit coupling involved. With spin-orbit coupling one has to modify the TB theory, since now the p_z-orbitals couple to the σ-orbitals. As one integrates out the contributions from the σ-orbitals one obtains an effective Hamiltonian describing spin-orbit coupling in graphynes. Crucial in this procedure is the fact that we were able to decompose the Hamiltonian describing the σ-orbitals into a dominant part and a subdominant part in such a way that the effective Hamiltonian can still be interpreted as a hopping Hamiltonian. It should be stressed that this method is very general and therefore not limited to the cases we considered. Furthermore, we also studied another mechanism of the SOC due to d-orbitals. However, though the underlying mechanism is quite different, the effective Hamiltonian still has the same form as the one due to the σ-orbitals.

The most interesting question is what are the effects of the SOC on the electronic band structure in graphynes. In particular, whether SOC can induce topological states in the system, as well as whether it is possible to tune the Dirac cones. First of all, for α-graphyne the physics is precisely the same as for graphene. The only difference with respect to graphene is the value of the intrinsic SOC parameter in α-graphyne, which is expected to be stronger due to the charge inhomogeneity present in graphynes.

Among the graphynes studied, β-graphyne seems to show the richest behavior in terms of the tunability of its band structure. We here demonstrated that such rich behavior in β-graphyne is due to the conspiracy of its lattice structure with a relatively large unit cell and the effects of the intrinsic and Rashba SOCs. The latter interaction allows for the tuning of the position and the number of Dirac cones in the band structure, therefore opening up the possibility to manipulate the transport properties of the system. Furthermore, we showed that in β-graphyne the Dirac cones can be located at all high-symmetry points in the BZ and a plethora of Lifshitz phase transitions between semi-metallic phases can be achieved.

Not only the Rashba SOC induces interesting effects, but the intrinsic SOC also does so. Indeed, the latter yields topologically nontrivial bands, some of which possess high Chern number. Moreover, when time-reversal symmetry is weakly broken and the SOC is tuned by the presence of heavy adatoms, such as Bi and Sn, a series of topological phase transitions between different Chern insulators is expected to occur. The topological bandgap closings are at Γ, M, K as well as at points in between, and this system therefore may interpolate between graphene where topological phase transitions occur at the K and K' points, and HgTe/CdTe quantum wells with the topological band gap at the Γ point [29].

Although both β- and γ-graphyne can be described by the same effective model, their physics is very different. First of all, γ-graphyne corresponds to a gapped system. As a result, the intrinsic SOC does not drive this system into a topologically insulating state for an arbitrary value of the intrinsic SOC. However, the Rashba SOC does lead to a very interesting behavior. Whereas in β-graphyne the internal Rashba SOC may open a gap, here the situation is completely reversed. The external Rashba can close the gap in γ-graphyne. Analogously to β-graphyne, the positions of the emergent Dirac cones in γ-graphyne can be controlled by the strength of the Rashba SOC.

Finally, we hope that our results will motivate *ab initio* studies of the spin-orbit effects in the graphyne family of carbon allotropes.

ACKNOWLEDGEMENTS

APPENDIX

A. LOW ENERGY TIGHT-BINDING HAMILTONIAN

Here, we outline the method used in this thesis to derive effective Hamiltonians. Suppose we are given a system such that we can split the spinor Ψ into a high-energy component Ψ_h and a low-energy component Ψ_l. Then, we may write the Hamiltonian matrix in a block form

$$H(\mathbf{k}) = \begin{pmatrix} H_{ll}(\mathbf{k}) & H_{lh}(\mathbf{k}) \\ H_{lh}^\dagger(\mathbf{k}) & H_{hh}(\mathbf{k}) \end{pmatrix}. \tag{A.1}$$

Using this decomposition, the Schrödinger equation reads

$$E\Psi_l(\mathbf{k}) = H_{ll}(\mathbf{k})\Psi_l(\mathbf{k}) + H_{lh}(\mathbf{k})\Psi_h(\mathbf{k}) \tag{A.2}$$

$$E\Psi_h(\mathbf{k}) = H_{lh}^\dagger(\mathbf{k})\Psi_l(\mathbf{k}) + H_{hh}(\mathbf{k})\Psi_h(\mathbf{k}). \tag{A.3}$$

We can then use Eq. (A.3) to eliminate $\Psi_h(\mathbf{k})$ in Eq. (A.2). Since $H_{lh}^\dagger(\mathbf{k})\Psi_l(\mathbf{k}) = (-H_{hh}(\mathbf{k})+E)\Psi_h(\mathbf{k})$, up to first order in E we obtain $\Psi_h(\mathbf{k}) = -H_{hh}^{-1}(\mathbf{k})(1 + EH_{hh}^{-1}(\mathbf{k}))H_{lh}^\dagger(\mathbf{k})\Psi_l(\mathbf{k})$. Therefore, Eq. (A.2) reduces to

$$(H_{ll}(\mathbf{k}) - H_{lh}(\mathbf{k})H_{hh}^{-1}(\mathbf{k})H_{lh}^\dagger(\mathbf{k}))\Psi_l(\mathbf{k}) = E(\mathbb{I} + H_{lh}(\mathbf{k})H_{hh}^{-2}(\mathbf{k})H_{lh}^\dagger(\mathbf{k}))\Psi_l(\mathbf{k}). \tag{A.4}$$

If we now introduce $S(\mathbf{k}) = \mathbb{I} + H_{lh}(\mathbf{k})H_{hh}^{-2}(\mathbf{k})H_{lh}^\dagger(\mathbf{k})$, and define $\phi(\mathbf{k}) = S^{1/2}(\mathbf{k})\Psi_l(\mathbf{k})$, we find the eigenvalue equation

$$(H_{ll}(\mathbf{k}) - H_{lh}(\mathbf{k})H_{hh}^{-1}(\mathbf{k})H_{lh}^\dagger(\mathbf{k}))S^{-1/2}(\mathbf{k})\phi(\mathbf{k}) = ES^{1/2}(\mathbf{k})\phi(\mathbf{k}). \tag{A.5}$$

By multiplying Eq. (A.5) on both sides with $S^{-1/2}(\mathbf{k})$ we find

$$H_{\text{eff}}(\mathbf{k})\phi(\mathbf{k}) = E\phi(\mathbf{k}), \tag{A.6}$$

with $H_{\text{eff}}(\mathbf{k})$ given by

$$H_{\text{eff}}(\mathbf{k}) = S^{-1/2}(\mathbf{k})(H_{ll}(\mathbf{k}) - H_{lh}(\mathbf{k})H_{hh}^{-1}(\mathbf{k})H_{lh}^\dagger(\mathbf{k}))S^{-1/2}(\mathbf{k}) \tag{A.7}$$

In various cases we consider in this thesis the matrix S happens to be diagonal, which greatly simplifies the expressions. It turns out that we can Fourier transform the effective Hamiltonian back to real space, and obtain an effective real space Hamiltonian. Note that several papers adopt a different approach, where they write down the transfer equations, then integrate out the high-energy contributions, see for example Ref. [16]. The drawback of their method lies in the fact that this can lead to a non-hermitean Hamiltonian, this happens for example in the context of $6, 6, 12$ graphyne [31].

B. EFFECTIVE HAMILTONIAN WITHOUT SPIN-ORBIT COUPLING

In the main text we have pointed out that the orbitals located at the vertices correspond to the low-energy states, whereas the orbitals at the edges give rise to high-energy states. This can be seen from the relation $|t_1| < |t_2| < |t_3|$, because the vertices are coupled by the parameter t_3, whereas the edges are coupled by the parameter t_2. Therefore, we can apply the low-energy approximation to the graphynes we consider. Then, we are able to accurately describe α-graphyne in terms of a two-site model, and β- and γ-graphyne by a six-site model. In the following we make use of three normalized NN vectors $\mathbf{d}_i$, $i = 1, 2, 3$ given by

$$
\begin{aligned}
\mathbf{d}_1 &= (-1/2, \sqrt{3}/2), \\
\mathbf{d}_2 &= (1, 0) \\
\mathbf{d}_3 &= (-1/2, -\sqrt{3}/2).
\end{aligned}
\tag{B.1}
$$

We denote the different bond lengths by l_i, $i = 1, 2, 3$, corresponding to the vertex-vertex, vertex-edge, and edge-edge bonds, respectively. Furthermore we define $l_4 = 2l_2 + l_3$.

B.1 Effective Hamiltonian for α-graphyne

By performing a Fourier transformation on Eq. (3.1) we obtain

$$
H^\alpha = \int \mathrm{d}k\, \Psi^\dagger(\mathbf{k}) H(\mathbf{k}) \Psi(\mathbf{k}),
$$

where $H(\mathbf{k})$ is given by Eq. (A.1),

$$
\Psi(k) = (A(\mathbf{k}), B(\mathbf{k}), a^1(\mathbf{k}), a^2(\mathbf{k}), a^3(\mathbf{k}), b^1(\mathbf{k}), b^2(\mathbf{k}), b^3(\mathbf{k}))^T,
\tag{B.2}
$$

and $H_{ll}(\mathbf{k})$, $H_{hl}(\mathbf{k})$, and $H_{hh}(\mathbf{k})$ are given by

$$
H_{ll}(\mathbf{k}) = 0,
$$

$$
H_{lh}(\mathbf{k}) = t_{\alpha,1}
\begin{pmatrix}
e^{il_2 \mathbf{k} \cdot \mathbf{d}_1} & e^{il_2 \mathbf{k} \cdot \mathbf{d}_2} & e^{il_2 \mathbf{k} \cdot \mathbf{d}_3} & 0 & 0 & 0 \\
0 & 0 & 0 & e^{-il_2 \mathbf{k} \cdot \mathbf{d}_1} & e^{-il_2 \mathbf{k} \cdot \mathbf{d}_2} & e^{-il_2 \mathbf{k} \cdot \mathbf{d}_3}
\end{pmatrix},
$$

$$
H_{hh}(\mathbf{k}) = t_{\alpha,2}
\begin{pmatrix}
0 & diag(e^{il_3 \mathbf{k} \cdot \mathbf{d}_1}, e^{il_3 \mathbf{k} \cdot \mathbf{d}_2}, e^{il_3 \mathbf{k} \cdot \mathbf{d}_3}) \\
diag(e^{-il_3 \mathbf{k} \cdot \mathbf{d}_1}, e^{-il_3 \mathbf{k} \cdot \mathbf{d}_2}, e^{-il_3 \mathbf{k} \cdot \mathbf{d}_3}) & 0
\end{pmatrix}.
$$

If we now follow the method outlined in App. A, we obtain

$$
(H_{ll}(\mathbf{k}) - H_{lh}(\mathbf{k}) H_{hh}^{-1}(\mathbf{k}) H_{lh}^\dagger(\mathbf{k})) = -t_{\alpha,1}^2/t_{\alpha,2}
\begin{pmatrix}
0 & f(\mathbf{k}) \\
f^*(\mathbf{k}) & 0
\end{pmatrix},
$$

with $f(\mathbf{k}) = \sum_{j=1}^3 e^{i\mathbf{k} \cdot \mathbf{d}_j l_4}$, and S is given by

$$
S = \mathbb{I}(1 + 3t_{\alpha,1}^2/t_{\alpha,2}^2).
$$

Hence, the effective Hamiltonian is given by

$$
H_{\text{eff}}^\alpha(\mathbf{k}) = -\frac{t_{\alpha,1}^2 t_{\alpha,2}}{t_{\alpha,2}^2 + 3t_{\alpha,1}^2}
\begin{pmatrix}
0 & f(\mathbf{k}) \\
f^*(\mathbf{k}) & 0
\end{pmatrix},
$$

and leads to Eq. (3.2) after performing an inverse Fourier transformation to obtain the real-space Hamiltonian.

B.2 Effective Hamiltonian for β-graphyne

In momentum space the Hamiltonian Eq. (3.3) reads

$$H^\beta = \int d\mathbf{k} \Psi^\dagger(\mathbf{k}) H(\mathbf{k}) \Psi(\mathbf{k}),$$

where $H(\mathbf{k})$ is given by Eq. (A.1),

$$\Psi(\mathbf{k}) = (A(\mathbf{k}), B(\mathbf{k}), C(\mathbf{k}), D(\mathbf{k}), E(\mathbf{k}), F(\mathbf{k}), a^1(\mathbf{k}), b^1(\mathbf{k}), c^1(\mathbf{k}), d^1(\mathbf{k}), e^1(\mathbf{k}), f^1(\mathbf{k}),$$
$$a^2(\mathbf{k}), b^2(\mathbf{k}), c^2(\mathbf{k}), d^2(\mathbf{k}), e^2(\mathbf{k}), f^2(\mathbf{k}))^T.$$

Here $H_{ll}(\mathbf{k})$ is given by

$$H_{ll}(\mathbf{k}) = t_{\beta,1} \begin{pmatrix} 0 & diag(e^{i\mathbf{k}\cdot\mathbf{d}_1 l_1}, e^{-i\mathbf{k}\cdot\mathbf{d}_2 l_1}, e^{i\mathbf{k}\cdot\mathbf{d}_3 l_1}) \\ diag(e^{-i\mathbf{k}\cdot\mathbf{d}_1 l_1}, e^{i\mathbf{k}\cdot\mathbf{d}_2 l_1}, e^{-i\mathbf{k}\cdot\mathbf{d}_3 l_1}) & 0 \end{pmatrix}.$$

The matrix $H_{lh}(\mathbf{k})$, which couples electrons at the vertices to the electrons belonging to the acetylene linkage can be further decomposed as

$$H_{lh}(\mathbf{k}) = t_{\beta,2} \begin{pmatrix} H_{lh}^1(\mathbf{k}) & H_{lh}^2(\mathbf{k}) \end{pmatrix}.$$

Where $H_{lh}^1(\mathbf{k})$ and $H_{lh}^2(\mathbf{k})$ are given by

$$H_{lh}^1(\mathbf{k}) = diag(e^{i\mathbf{k}\cdot\mathbf{d}_3 l_2}, e^{-i\mathbf{k}\cdot\mathbf{d}_3 l_2}, e^{i\mathbf{k}\cdot\mathbf{d}_2 l_2}, e^{-i\mathbf{k}\cdot\mathbf{d}_2 l_2}, e^{i\mathbf{k}\cdot\mathbf{d}_1 l_2}, e^{-i\mathbf{k}\cdot\mathbf{d}_1 l_2}),$$
$$H_{lh}^2(\mathbf{k}) = diag(e^{i\mathbf{k}\cdot\mathbf{d}_2 l_2}, e^{-i\mathbf{k}\cdot\mathbf{d}_1 l_2}, e^{i\mathbf{k}\cdot\mathbf{d}_1 l_2}, e^{-i\mathbf{k}\cdot\mathbf{d}_3 l_2}, e^{i\mathbf{k}\cdot\mathbf{d}_3 l_2}, e^{-i\mathbf{k}\cdot\mathbf{d}_2 l_2}).$$

Finally we decompose the matrix $H_{hh}(\mathbf{k})$ as

$$H_{hh}(\mathbf{k}) = t_{\beta,3} \begin{pmatrix} H_1(\mathbf{k}) & 0 \\ 0 & H_2(\mathbf{k}) \end{pmatrix}.$$

The matrix $H_1(\mathbf{k})$ is given by

$$H_1(\mathbf{k}) = diag(U_3(\mathbf{k}), U_2(\mathbf{k}), U_1(\mathbf{k})),$$

with

$$U_i(\mathbf{k}) = \begin{pmatrix} 0 & e^{i\mathbf{k}\cdot\mathbf{d}_i l_3} \\ e^{-i\mathbf{k}\cdot\mathbf{d}_i l_3} & 0 \end{pmatrix}.$$

The matrix $H_2(\mathbf{k})$ is given by

$$H_2(\mathbf{k}) = \begin{pmatrix} 0 & 0 & 0 & e^{i\mathbf{k}\cdot\mathbf{d}_2 l_3} \\ 0 & U_1(-\mathbf{k}) & 0 & 0 \\ 0 & 0 & U_3(-\mathbf{k}) & 0 \\ e^{-i\mathbf{k}\cdot\mathbf{d}_2 l_3} & 0 & 0 & 0 \end{pmatrix}.$$

If we now do the low-energy approximation we find that $S = (1 + 2t_{\beta,2}^2/t_{\beta,3}^2)\mathbb{I}$. Furthermore if change the basis to $\tilde{\Psi} = (A, C, E, B, D, F)$, then $H_{ll}(\mathbf{k}) - H_{lh}(\mathbf{k}) H_{hh}^{-1}(\mathbf{k}) H_{lh}^\dagger(\mathbf{k})$ reads

$$H_{ll}(\mathbf{k}) - H_{lh}(\mathbf{k}) H_{hh}^{-1}(\mathbf{k}) H_{lh}^\dagger(\mathbf{k}) = \begin{pmatrix} 0 & U(\mathbf{k}) \\ U^\dagger(\mathbf{k}) & 0 \end{pmatrix},$$

and $U(\mathbf{k})$ reads

$$U(\mathbf{k}) = \begin{pmatrix} \frac{t_{\beta,2}^2}{t_{\beta,3}} e^{i\mathbf{k}\cdot\mathbf{d}_3 l_4} & t_{\beta,1} e^{i\mathbf{k}\cdot\mathbf{d}_1 l_1} & \frac{t_{\beta,2}^2}{t_{\beta,3}} e^{i\mathbf{k}\cdot\mathbf{d}_2 l_4} \\ \frac{t_{\beta,2}^2}{t_{\beta,3}} e^{i\mathbf{k}\cdot\mathbf{d}_1 l_4} & \frac{t_{\beta,2}^2}{t_{\beta,3}} e^{i\mathbf{k}\cdot\mathbf{d}_2 l_4} & t_{\beta,1} e^{i\mathbf{k}\cdot\mathbf{d}_3 l_1} \\ t_{\beta,1} e^{i\mathbf{k}\cdot\mathbf{d}_2 l_1} & \frac{t_{\beta,2}^2}{t_{\beta,3}} e^{i\mathbf{k}\cdot\mathbf{d}_3 l_4} & \frac{t_{\beta,2}^2}{t_{\beta,3}} e^{i\mathbf{k}\cdot\mathbf{d}_1 l_4} \end{pmatrix}.$$

If we perform an inverse Fourier transformation, we obtain Eq. (3.4), the real-space β-graphyne Hamiltonian.

B.3 Effective Hamiltonian for γ-graphyne

By applying a Fourier transformation on Eq. (3.5) we obtain

$$H^\gamma = \int d\mathbf{k}\Psi^\dagger(\mathbf{k})H(\mathbf{k})\Psi(\mathbf{k}),$$

where $H_\mathbf{k}$ is given by Eq. (A.1),

$$\Psi(\mathbf{k}) = (A(\mathbf{k}), C(\mathbf{k}), E(\mathbf{k}), B(\mathbf{k}), D(\mathbf{k}), F(\mathbf{k}), a(\mathbf{k}), c(\mathbf{k}), e(\mathbf{k}), b(\mathbf{k}), d(\mathbf{k}), f(\mathbf{k}))^T.$$

The matrix $H_{ll}(\mathbf{k})$ reads

$$H_{ll}(\mathbf{k}) = t_{\gamma,1}\begin{pmatrix} 0 & U_{ll}(\mathbf{k}) \\ U_{ll}^\dagger(\mathbf{k}) & 0 \end{pmatrix},$$

with $U_{ll}(\mathbf{k})$ given by

$$U_{ll}(\mathbf{k}) = \begin{pmatrix} e^{i\mathbf{k}\cdot\mathbf{d}_3 l_1} & 0 & e^{i\mathbf{k}\cdot\mathbf{d}_2 l_1} \\ e^{i\mathbf{k}\cdot\mathbf{d}_1 l_1} & e^{i\mathbf{k}\cdot\mathbf{d}_2 l_1} & 0 \\ 0 & e^{i\mathbf{k}\cdot\mathbf{d}_3 l_1} & e^{i\mathbf{k}\cdot\mathbf{d}_1 l_1} \end{pmatrix}.$$

Furthermore, we find

$$H_{lh} = t_{\gamma,2}diag(e^{i\mathbf{k}\cdot\mathbf{d}_1 l_2}, e^{-i\mathbf{k}\cdot\mathbf{d}_2 l_2}, e^{i\mathbf{k}\cdot\mathbf{d}_3 l_2}, e^{-i\mathbf{k}\cdot\mathbf{d}_1 l_2}, e^{i\mathbf{k}\cdot\mathbf{d}_2 l_2}, e^{i\mathbf{k}\cdot\mathbf{d}_3 l_2}).$$

Finally $H_{hh}(\mathbf{k})$ reads

$$H_{hh}(\mathbf{k}) = t_{\gamma,3}\begin{pmatrix} 0 & diag(e^{i\mathbf{k}\cdot\mathbf{d}_1 l_3}, e^{-i\mathbf{k}\cdot\mathbf{d}_2 l_3}, e^{i\mathbf{k}\cdot\mathbf{d}_3 l_3}) \\ diag(e^{-i\mathbf{k}\cdot\mathbf{d}_1 l_3}, e^{i\mathbf{k}\cdot\mathbf{d}_2 l_3}, e^{-i\mathbf{k}\cdot\mathbf{d}_3 l_3}) & 0 \end{pmatrix},$$

Therefore, we find $S = (1 + t_{\gamma,2}^2/t_{\gamma,3}^2)\mathbb{I}$, and

$$H_{ll}(\mathbf{k}) - H_{lh}(\mathbf{k})H_{hh}^{-1}(\mathbf{k})H_{lh}^\dagger(\mathbf{k}) = \begin{pmatrix} 0 & U(\mathbf{k}) \\ U^\dagger(\mathbf{k}) & 0 \end{pmatrix},$$

and $U(\mathbf{k})$ reads

$$U(\mathbf{k}) = \begin{pmatrix} t_{\gamma_1}e^{i\mathbf{k}\cdot\mathbf{d}_3 l_4} & \frac{-t_{\gamma,2}^2}{t_{\gamma,3}}e^{i\mathbf{k}\cdot\mathbf{d}_1 l_1} & t_{\gamma_1}e^{i\mathbf{k}\cdot\mathbf{d}_2 l_4} \\ t_{\gamma_1}e^{i\mathbf{k}\cdot\mathbf{d}_1 l_4} & t_{\gamma_1}e^{i\mathbf{k}\cdot\mathbf{d}_2 l_4} & \frac{-t_{\gamma,2}^2}{t_{\gamma,3}}e^{i\mathbf{k}\cdot\mathbf{d}_3 l_1} \\ \frac{-t_{\gamma,2}^2}{t_{\gamma,3}}e^{i\mathbf{k}\cdot\mathbf{d}_2 l_1} & t_{\gamma_1}e^{i\mathbf{k}\cdot\mathbf{d}_3 l_4} & t_{\gamma_1}e^{i\mathbf{k}\cdot\mathbf{d}_1 l_4} \end{pmatrix}.$$

As a result, after an inverse Fourier transformation, we end up with the effective Hamiltonian Eq. (3.6).

C. TIGHT-BINDING MODELS WITH σ-ORBITALS

In this appendix we present the TB models containing σ-orbitals used to derive the SOC Hamiltonians. To denote different σ-orbitals on each site, we introduce a subscript $j = 1, 2, 3$. Different sites are labeled by a superscript (the same as for p_z-orbitals), see Fig. 3.1.

C.1   Tight-binding models with σ-orbitals for α-graphyne

The labeling of the different σ-orbitals is shown in Fig. C.1. Combining this labeling with the definition of the dominant NN hoppings $(V_2, \ldots, V_4)$ as given in Fig. 4.1(a), we find that H^α_{NN} reads

$$H^\alpha_{NN} = \left\{ V_2 \sum_{\langle i,j \rangle} \left(A^\dagger_{1,i} a^1_{1,j} + A^\dagger_{2,i} a^2_{2,j} + A^\dagger_{3,i} a^3_{3,j} + B^\dagger_{1,i} b^1_{1,j} + B^\dagger_{2,i} b^2_{2,j} + B^\dagger_{3,i} b^3_{3,j} \right) + V_3 \sum_{\langle i,j \rangle} \left[(a^1_{3,i})^\dagger b^1_{3,j} \right. \right.$$

$$\left. \left. + (a^2_{1,i})^\dagger b^2_{1,j} + (a^3_{2,i})^\dagger b^3_{2,j} \right] + V_4 \sum_{\langle i,j \rangle} \left[(a^1_{2,i})^\dagger b^1_{2,j} + (a^2_{3,i})^\dagger b^2_{3,j} + (a^3_{1,i})^\dagger b^3_{1,j} \right] \right\} + h.c. \tag{C.1}$$
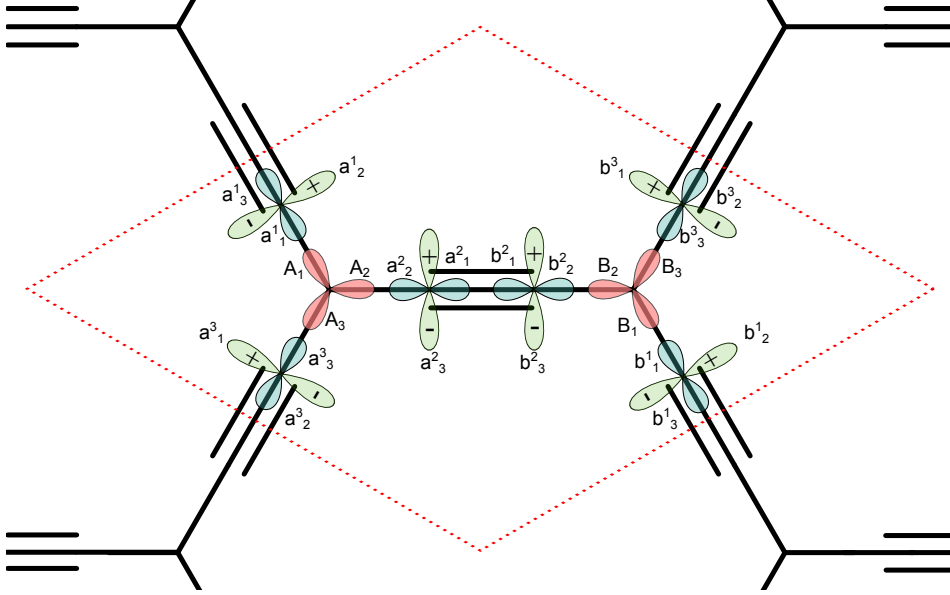

Fig. C.1: Labeling used for the α-graphyne TB model (C.1) and (C.2).

The on-site energies $(\varepsilon_2, \ldots, \varepsilon_4)$ and hoppings (V_6, V_9) are included in H^α_{onsite}, which is given by

$$
\begin{aligned}
H^\alpha_{onsite} = \Bigg\{ & \frac{\varepsilon_2}{2} \sum_i \left(A^\dagger_{1,i} A_{1,i} + A^\dagger_{2,i} A_{2,i} + A^\dagger_{3,i} A_{3,i} + B^\dagger_{1,i} B_{1,i} + B^\dagger_{2,i} B_{2,i} + B^\dagger_{3,i} B_{3,i} \right) \\
& + \frac{\varepsilon_3}{2} \sum_i \left[(a^1_{3,i})^\dagger a^1_{3,i} + (a^2_{1,i})^\dagger a^2_{1,i} + (a^3_2)^\dagger a^3_2 + (b^1_{3,i})^\dagger b^1_{3,i} + (b^2_{1,i})^\dagger b^2_{1,i} + (b^3_{2,i})^\dagger b^3_{2,i} \right] \\
& + \frac{\varepsilon_4}{2} \sum_i \left[(a^1_{1,i})^\dagger a^1_{1,i} + (a^2_{2,i})^\dagger a^2_{2,i} + (a^3_{3,i})^\dagger a^3_{3,i} + (b^1_{1,i})^\dagger b^1_{1,i} + (b^2_{2,i})^\dagger b^2_{2,i} + (b^3_{3,i})^\dagger b^3_{3,i} \right] \\
& + V_6 \sum_i \left(A^\dagger_{1,i} A_{2,i} + A^\dagger_{2,i} A_{3,i} + A^\dagger_{3,i} A_{1,i} + B^\dagger_{1,i} B_{2,i} + B^\dagger_{2,i} B_{3,i} + B^\dagger_{3,i} B_{1,i} \right) \\
& + V_9 \sum_i \left[(a^1_{1,i})^\dagger a^1_{3,i} + (a^2_{2,i})^\dagger a^2_{1,i} + (a^3_{3,i})^\dagger a^3_{2,i} + (b^1_{1,i})^\dagger b^1_{3,i} + (b^2_{2,i})^\dagger b^2_{1,i} + (b^3_{3,i})^\dagger b^3_{2,i} \right] \Bigg\} + h.c. \quad \text{(C.2)}
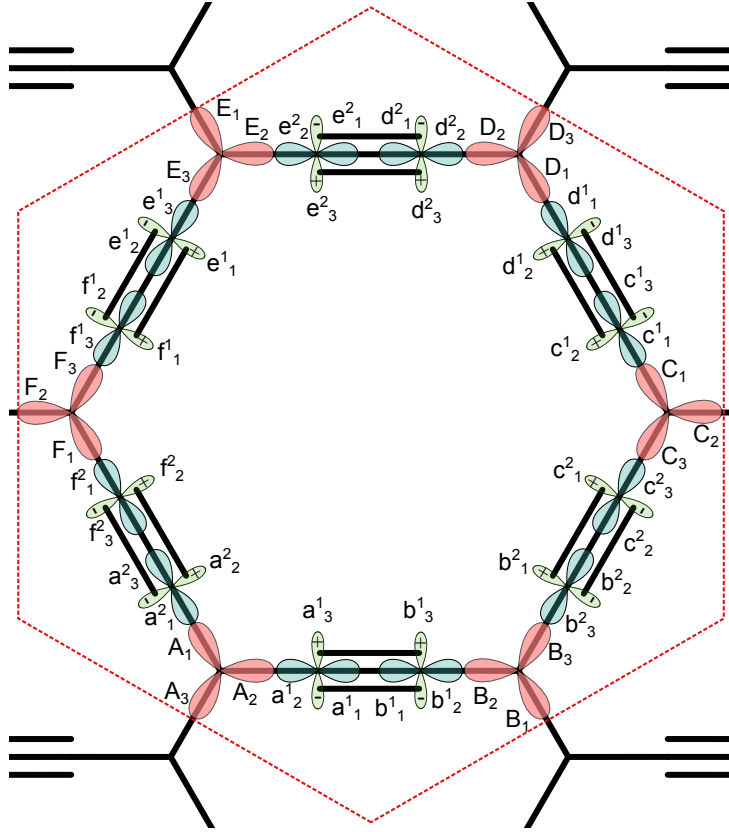\end{aligned}
$$

Fig. C.2: Labeling of orbitals used in the β-graphyne TB model (C.3) and (C.4).

C.2 Tight-binding models with σ-orbitals for β-graphyne

The labeling of the different σ-orbitals is shown in Fig. C.2, together with the definition of the dominant NN hoppings $(V_1, \ldots, V_4)$ shown in Fig. 4.1(b) we find

$$
\begin{aligned}
H_{\mathrm{NN}}^{\beta} = \Bigg\{ &V_1 \sum_{\langle i,j \rangle} \left(A_{3,i}^{\dagger} D_{3,j} + B_{1,i}^{\dagger} E_{1,j} + C_{2,i}^{\dagger} F_{2,j} \right) + V_2 \sum_{\langle i,j \rangle} \left(A_{1,i}^{\dagger} a_{1,j}^2 + A_{2,i}^{\dagger} a_{2,j}^1 + B_{2,i}^{\dagger} b_{2,j}^1 + B_{3,i}^{\dagger} b_{3,j}^2 + C_{1,i}^{\dagger} c_{1,j}^1 \right. \\
&\left. + C_{3,i}^{\dagger} c_{3,j}^2 + D_{1,i}^{\dagger} d_{1,j}^1 + D_{2,i}^{\dagger} d_{2,j}^2 + E_{2,i}^{\dagger} e_{2,j}^2 + E_{3,i}^{\dagger} e_{3,j}^1 + F_{1,i}^{\dagger} f_{1,j}^2 + F_{3,i}^{\dagger} f_{3,j}^1 \right) + V_3 \sum_{\langle i,j \rangle} \left[(a_{1,i}^1)^{\dagger} b_{1,j}^1 \right. \\
&+ (a_{3,i}^2)^{\dagger} f_{3,j}^2 + (c_{3,i}^1)^{\dagger} d_{3,j}^1 + (c_{2,i}^2)^{\dagger} b_{2,j}^1 + (e_{2,i}^1)^{\dagger} f_{2,j}^1 + (e_{1,i}^2)^{\dagger} d_{1,j}^2 \left. \right] + V_4 \sum_{\langle i,j \rangle} \left[(a_{3,i}^1)^{\dagger} b_{3,j}^1 + (a_{2,i}^2)^{\dagger} f_{2,j}^2 \right. \\
&+ (c_{2,i}^1)^{\dagger} d_{2,j}^1 + (c_{1,i}^2)^{\dagger} b_{1,j}^2 + (e_{1,i}^1)^{\dagger} f_{1,j}^1 + (e_{3,i}^2)^{\dagger} d_{3,j}^2 \left. \right] \Bigg\} + h.c.
\end{aligned}
\tag{C.3}
$$

The term describing the on-site energies $(\varepsilon_1, \ldots, \varepsilon_5)$ and hoppings $(V_5, \ldots, V_9)$ reads

$$
\begin{aligned}
H_{\mathrm{onsite}}^{\beta} = \Bigg\{ &\frac{\varepsilon_1}{2} \sum_i \left(A_{3,i}^{\dagger} A_{3,i} + B_{1,i}^{\dagger} B_{1,i} + C_{2,i}^{\dagger} C_{2,i} + D_{3,i}^{\dagger} D_{3,i} + E_{1,i}^{\dagger} E_{1,i} + F_{2,i}^{\dagger} F_{2,i} \right) + \frac{\varepsilon_2}{2} \sum_i \left(A_{1,i}^{\dagger} A_{1,i} + A_{2,i}^{\dagger} A_{2,i} \right. \\
&+ B_{2,i}^{\dagger} B_{2,i} + B_{3,i}^{\dagger} B_{3,i} + C_{1,i}^{\dagger} C_{1,i} + C_{3,i}^{\dagger} C_{3,i} + D_{1,i}^{\dagger} D_{1,i} + D_{2,i}^{\dagger} D_{2,i} + E_{2,i}^{\dagger} E_{2,i} + E_{3,i}^{\dagger} E_{3,i} + F_{1,i}^{\dagger} F_{1,i} \\
&+ F_{3,i}^{\dagger} F_{3,i} \big) + \frac{\varepsilon_3}{2} \sum_i \left[(a_{1,i}^1)^{\dagger} a_{1,i}^1 + (a_{3,i}^2)^{\dagger} a_{3,i}^2 + (b_{1,i}^1)^{\dagger} b_{1,i}^1 + (b_{2,i}^2)^{\dagger} b_{2,i}^2 + (c_{3,i}^1)^{\dagger} c_{3,i}^1 + (c_{2,i}^2)^{\dagger} c_{2,i}^2 \right. \\
&+ (d_{3,i}^1)^{\dagger} d_{3,i}^1 + (d_{1,i}^2)^{\dagger} d_{1,i}^2 + (e_{2,i}^1)^{\dagger} e_{2,i}^1 + (e_{1,i}^2)^{\dagger} e_{1,i}^2 + (f_{2,i}^1)^{\dagger} f_{2,i}^1 + (f_{3,i}^2)^{\dagger} f_{3,i}^2 \left. \right] + \frac{\varepsilon_4}{2} \sum_i \left[(a_{2,i}^1)^{\dagger} a_{2,i}^1 \right. \\
&+ (a_{1,i}^2)^{\dagger} a_{1,i}^2 + (b_{2,i}^1)^{\dagger} b_{2,i}^1 + (b_{3,i}^2)^{\dagger} b_{3,i}^2 + (c_{1,i}^1)^{\dagger} c_{1,i}^1 + (c_{3,i}^2)^{\dagger} c_{3,i}^2 + (d_{1,i}^1)^{\dagger} d_{1,i}^1 + (d_{2,i}^2)^{\dagger} d_{2,i}^2 + (e_{3,i}^1)^{\dagger} e_{3,i}^1 \\
&+ (e_{2,i}^2)^{\dagger} e_{2,i}^2 + (f_{3,i}^1)^{\dagger} f_{3,i}^1 + (f_{1,i}^2)^{\dagger} f_{1,i}^2 \left. \right] + \frac{\varepsilon_5}{2} \sum_i \left[(a_{3,i}^1)^{\dagger} a_{3,i}^1 + (a_{2,i}^2)^{\dagger} a_{2,i}^2 + (b_{3,i}^1)^{\dagger} b_{3,i}^1 + (b_{1,i}^2)^{\dagger} b_{1,i}^2 \right. \\
&+ (c_{2,i}^1)^{\dagger} c_{2,i}^1 + (c_{1,i}^2)^{\dagger} c_{1,i}^2 + (d_{2,i}^1)^{\dagger} d_{2,i}^1 + (d_{3,i}^2)^{\dagger} d_{3,i}^2 + (e_{1,i}^1)^{\dagger} e_{1,i}^1 + (e_{3,i}^2)^{\dagger} e_{3,i}^2 + (f_{1,i}^1)^{\dagger} f_{1,i}^1 + (f_{2,i}^2)^{\dagger} f_{2,i}^2 \left. \right] \\
&+ V_5 \sum_i \left[A_{3,i}^{\dagger} (A_{1,i} + A_{2,i}) + B_{1,i}^{\dagger} (B_{2,i} + B_{3,i}) + C_{2,i}^{\dagger} (C_{1,i} + C_{3,i}) + D_{3,i}^{\dagger} (D_{1,i} + D_{2,i}) + E_{1,i}^{\dagger} (E_{2,i} \right. \\
&+ E_{3,i}) + F_{2,i}^{\dagger} (F_{1,i} + F_{3,i}) \left. \right] + V_6 \sum_i \left[A_{1,i}^{\dagger} A_{2,i} + B_{2,i}^{\dagger} B_{3,i} + C_{1,i}^{\dagger} C_{3,i} + D_{1,i}^{\dagger} D_{2,i} + E_{2,i}^{\dagger} E_{3,i} + F_{1,i}^{\dagger} F_{3,i} \right] \\
&+ V_7 \sum_i \left[(a_{2,i}^1)^{\dagger} a_{3,i}^1 + (a_{1,i}^2)^{\dagger} a_{2,i}^2 + (b_{2,i}^1)^{\dagger} b_{3,i}^1 + (b_{3,i}^2)^{\dagger} b_{1,i}^2 + (c_{1,i}^1)^{\dagger} c_{2,i}^1 + (c_{3,i}^2)^{\dagger} c_{1,i}^2 + (d_{1,i}^1)^{\dagger} d_{2,i}^1 \right. \\
&+ (d_{2,i}^2)^{\dagger} d_{3,i}^2 + (e_{1,i}^1)^{\dagger} e_{3,i}^1 + (e_{2,i}^2)^{\dagger} e_{3,i}^2 + (f_{3,i}^1)^{\dagger} f_{1,i}^1 + (f_{1,i}^2)^{\dagger} f_{2,i}^2 \left. \right] + V_8 \sum_i \left[(a_{1,i}^1)^{\dagger} a_{3,i}^1 + (a_{3,i}^2)^{\dagger} a_{2,i}^2 \right. \\
&+ (b_{1,i}^1)^{\dagger} b_{3,i}^1 + (b_{2,i}^2)^{\dagger} b_{1,i}^2 + (c_{3,i}^1)^{\dagger} c_{2,i}^1 + (c_{2,i}^2)^{\dagger} c_{1,i}^2 + (d_{3,i}^1)^{\dagger} d_{2,i}^1 + (d_{1,i}^2)^{\dagger} d_{3,i}^2 + (e_{1,i}^1)^{\dagger} e_{2,i}^1 + (e_{1,i}^2)^{\dagger} e_{3,i}^2 \\
&+ (f_{2,i}^1)^{\dagger} f_{1,i}^1 + (f_{3,i}^2)^{\dagger} f_{2,i}^2 \left. \right] + V_9 \sum_i \left[(a_{1,i}^1)^{\dagger} a_{2,i}^1 + (a_{3,i}^2)^{\dagger} a_{1,i}^2 + (b_{1,i}^1)^{\dagger} b_{2,i}^1 + (b_{2,i}^2)^{\dagger} b_{3,i}^2 + (c_{3,i}^1)^{\dagger} c_{1,i}^1 \right. \\
&+ (c_{2,i}^2)^{\dagger} c_{3,i}^2 + (d_{3,i}^1)^{\dagger} d_{1,i}^1 + (d_{1,i}^2)^{\dagger} d_{2,i}^2 + (e_{3,i}^1)^{\dagger} e_{2,i}^1 + (e_{1,i}^2)^{\dagger} e_{2,i}^2 + (f_{2,i}^1)^{\dagger} f_{3,i}^1 + (f_{3,i}^2)^{\dagger} f_{1,i}^2 \left. \right] \Bigg\} + h.c.
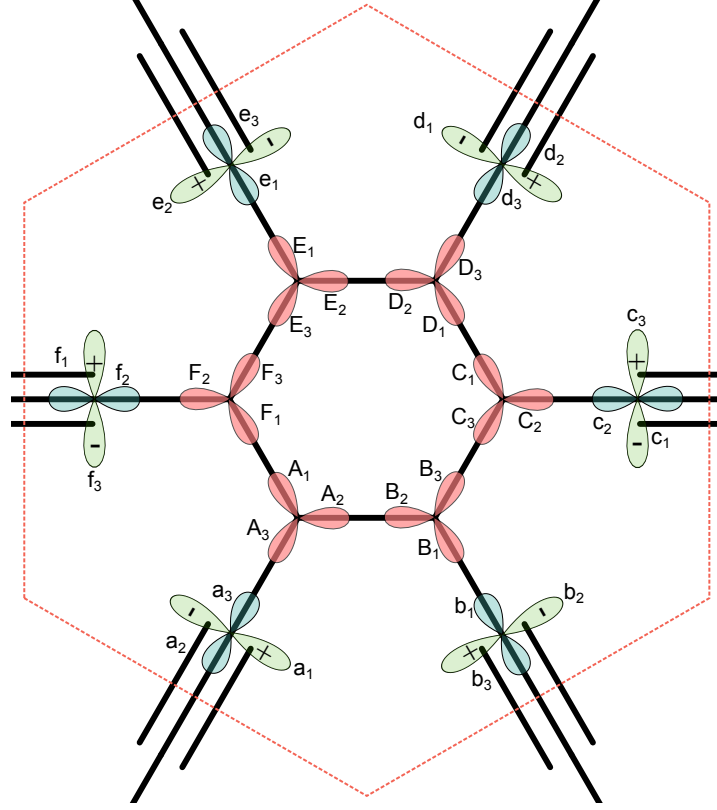\end{aligned}
\tag{C.4}
$$

Fig. C.3: Labeling of orbitals used in the γ-graphyne TB model (C.5) and (C.6).

C.3   Tight-binding models with σ-orbitals for γ-graphyne

The labeling for γ-graphyne is shown in Fig. C.3. The definition of the dominant NN hoppings $(V_1, \ldots, V_4)$ shown in Fig. 4.1(c) leads to

$$
\begin{aligned}
H_{NN}^{\gamma} = \Bigg\{ & V_1 \sum_{\langle i,j \rangle} \left(A_{1,i}^{\dagger} F_{1,j} + A_{2,i}^{\dagger} B_{2,j} + C_{1,i}^{\dagger} D_{1,j} + C_{3,i}^{\dagger} B_{3,j} + E_{2,i}^{\dagger} D_{2,j} + E_{3,i}^{\dagger} F_{3,j} \right) + V_2 \sum_{\langle i,j \rangle} \left(A_{3,i}^{\dagger} a_{3,j} + B_{1,i}^{\dagger} b_{1,j} \right. \\
& + C_{2,i}^{\dagger} c_{2,j} + D_{3,i}^{\dagger} d_{3,j} + E_{1,i}^{\dagger} e_{1,j} + F_{2,i}^{\dagger} f_{2,j} \Big) + V_3 \sum_{\langle i,j \rangle} \left(a_{2,i}^{\dagger} d_{2,j} + b_{3,i}^{\dagger} e_{3,j} + c_{1,i}^{\dagger} f_{1,j} \right) + V_4 \sum_{\langle i,j \rangle} \Big(a_{1,i}^{\dagger} d_{1,j} \\
& + b_{2,i}^{\dagger} e_{2,j} + c_{3,i}^{\dagger} f_{3,j} \Big) \Bigg\} + h.c.
\end{aligned}
\tag{C.5}
$$

The onsite hoppings (V_5, V_6) and energies $(\varepsilon_1, \ldots, \varepsilon_5)$ yield

$$
\begin{aligned}
H^\gamma_{onsite} = \Bigg\{ & \frac{\varepsilon_1}{2} \sum_i \big(A^\dagger_{1,i} A_{1,i} + A^\dagger_{2,i} A_{2,i} + B^\dagger_{2,i} B_{2,i} + B^\dagger_{3,i} B_{3,i} + C^\dagger_{1,i} C_{1,i} + C^\dagger_{3,i} C_{3,i} + D^\dagger_{1,i} D_{1,i} + D^\dagger_{2,i} D_{2,i} \\
& + E^\dagger_{2,i} E_{2,i} + E^\dagger_{3,i} E_{3,i} + F^\dagger_{1,i} F_{1,i} + F^\dagger_{3,i} F_{3,i} \big) + \frac{\varepsilon_2}{2} \sum_i \big(A^\dagger_{3,i} A_{3,i} + B^\dagger_{1,i} B_{1,i} + C^\dagger_{2,i} C_{2,i} + D^\dagger_{3,i} D_{3,i} \\
& + E^\dagger_{1,i} E_{1,i} + F^\dagger_{2,i} F_{2,i} \big) + \frac{\varepsilon_3}{2} \sum_i \big(a^\dagger_{2,i} a_{2,i} + b^\dagger_{3,i} b_{3,i} + c^\dagger_{1,i} c_{1,i} + d^\dagger_{2,i} d_{2,i} + e^\dagger_{3,i} e_{3,i} + f^\dagger_{1,i} f_{1,i} \big) \\
& + \frac{\varepsilon_4}{2} \sum_i \big(a^\dagger_{3,i} a_{3,i} + b^\dagger_{1,i} b_{1,i} + c^\dagger_{2,i} c_{2,i} + d^\dagger_{3,i} d_{3,i} + e^\dagger_{1,i} e_{1,i} + f^\dagger_{2,i} f_{2,i} \big) + \frac{\varepsilon_5}{2} \sum_i \big(a^\dagger_{1,i} a_{1,i} + b^\dagger_{2,i} b_{2,i} + c^\dagger_{3,i} c_{3,i} \\
& + d^\dagger_{1,i} d_{1,i} + e^\dagger_{2,i} e_{2,i} + f^\dagger_{3,i} f_{3,i} \big) + V_5 \sum_i \big[A^\dagger_{3,i} (A_{1,i} + A_{2,i}) + B^\dagger_{1,i} (B_{2,i} + B_{3,i}) + C^\dagger_{2,i} (C_{1,i} + C_{3,i}) \\
& + D^\dagger_{3,i} (D_{1,i} + D_{2,i}) + E^\dagger_{1,i} (E_{2,i} + E_{3,i}) + F^\dagger_{2,i} (F_{1,i} + F_{3,i}) \big] + V_6 \sum_i \big(A^\dagger_{1,i} A_{2,i} + B^\dagger_{2,i} B_{3,i} + C^\dagger_{1,i} C_{3,i} \\
& + D^\dagger_{1,i} D_{2,i} + E^\dagger_{2,i} E_{3,i} + F^\dagger_{1,i} F_{3,i} \big) \Bigg\} + h.c.
\end{aligned}
\tag{C.6}
$$

D. SPIN-ORBIT COUPLING HAMILTONIANS

The SOC Hamiltonians $H_E^{z;\sigma}$ and $H_L^{z;\sigma}$ given in Eqs. (4.6) and (4.7) are in terms of the p_x, p_y, and s orbitals. Since we would like to compute the effective SOC Hamiltonians based on Eq. (4.18), we need to rewrite Eqs. (4.6) and (4.7) in terms of the hybrid orbitals. In Table D.1 we provide the convention we used for the change of basis.

D.1 α-graphyne

For α-graphyne the Hamiltonians (4.6) and (4.7) in terms of the orbitals read

$$
\begin{aligned}
H_L^{z;\sigma} = {}& i\xi_{p2} \sum_i \Big[A_i^\dagger (2^{-1/2}\sigma_x + 6^{-1/2}\sigma_y) A_{1,i} + A_i^\dagger (-(2/3)^{1/2}\sigma_y) A_{2,i} + A_i^\dagger (-2^{-1/2}\sigma_x + 6^{-1/2}\sigma_y) A_{3,i} \\
& B_i^\dagger (-2^{-1/2}\sigma_x - 6^{-1/2}\sigma_y) B_{1,i} + B_i^\dagger ((2/3)^{1/2}\sigma_y) B_{2,i} + B_i^\dagger (2^{-1/2}\sigma_x - 6^{-1/2}\sigma_y) B_{3,i} \Big] \\
& + i\xi_{p1} \sum_i \Big[(a_i^1)^\dagger 2^{-1/2}(-\sqrt{3}\sigma_x/2 - \sigma_y/2) a_{1,i}^1 + (a_i^1)^\dagger (\sigma_x/2 - \sqrt{3}\sigma_y/2) a_{2,i}^1 \\
& + (a_i^1)^\dagger 2^{-1/2}(\sqrt{3}\sigma_x/2 + \sigma_y/2) a_{3,i}^1 + (a_i^2)^\dagger (-2^{-1/2}\sigma_y) a_{1,i}^2 + (a_i^2)^\dagger (2^{-1/2}\sigma_y) a_{2,i}^2 + (a_i^2)^\dagger (\sigma_x) a_{3,i}^2 \\
& + (a_i^3)^\dagger (\sigma_x/2 + \sqrt{3}\sigma_y/2) a_{1,i}^3 + (a_i^3)^\dagger 2^{-1/2}(-\sqrt{3}\sigma_x/2 + \sigma_y/2) a_{2,i}^3 + (a_i^3)^\dagger 2^{-1/2}(\sqrt{3}\sigma_x/2 - \sigma_y/2) a_{3,i}^3 \\
& + (b_i^1)^\dagger 2^{-1/2}(\sqrt{3}\sigma_x/2 + \sigma_y/2) b_{1,i}^1 + (b_i^1)^\dagger (\sigma_x/2 - \sqrt{3}\sigma_y/2) b_{2,i}^1 + (b_i^1)^\dagger 2^{-1/2}(-\sqrt{3}\sigma_x/2 - \sigma_y/2) b_{3,i}^1 \\
& + (b_i^2)^\dagger 2^{-1/2}(\sigma_y) b_{1,i}^2 - (b_i^2)^\dagger 2^{-1/2}(\sigma_y) b_{2,i}^2 + (b_i^2)^\dagger (\sigma_x) b_{3,i}^2 \\
& + (b_i^3)^\dagger (\sigma_x/2 + \sqrt{3}\sigma_y/2) b_{1,i}^3 + (b_i^3)^\dagger 2^{-1/2}(\sqrt{3}\sigma_x/2 - \sigma_y/2) b_{2,i}^3 + (b_i^3)^\dagger 2^{-1/2}(-\sqrt{3}\sigma_x/2 + \sigma_y/2) b_{3,i}^3 \Big],
\end{aligned}
\tag{D.1}
$$

and

$$
\begin{aligned}
H_E^{z;\sigma} = {}& \xi_{sp2} 3^{-1/2} \sum_i \Big[A_i^\dagger (A_{1,i} + A_{2,i} + A_{3,i}) + B_i^\dagger (B_{1,i} + B_{2,i} + B_{3,i}) \Big] + \xi_{sp1} 2^{-1/2} \sum_i \Big[(a_i^1)^\dagger (a_{1,i}^1 + a_{3,i}^1) \\
& + (a_i^2)^\dagger (a_{1,i}^2 + a_{2,i}^2) + (a_i^3)^\dagger (a_{2,i}^3 + a_{3,i}^3) + (b_i^1)^\dagger (b_{1,i}^1 + b_{3,i}^1) + (b_i^2)^\dagger (b_{1,i}^2 + b_{2,i}^2) + (b_i^3)^\dagger (b_{2,i}^3 + b_{3,i}^3) \Big].
\end{aligned}
\tag{D.2}
$$

	sp^2						sp						p					
s	$1/\sqrt{3}$	$1/\sqrt{3}$	$1/\sqrt{3}$	$1/\sqrt{3}$	$1/\sqrt{3}$	$1/\sqrt{3}$	$1/\sqrt{2}$	$1/\sqrt{2}$	$1/\sqrt{2}$	$1/\sqrt{2}$	$1/\sqrt{2}$	$1/\sqrt{2}$	0	0	0	0	0	0
p_x	$1/\sqrt{6}$	$-\sqrt{2/3}$	$1/\sqrt{6}$	$-1/\sqrt{6}$	$\sqrt{2/3}$	$-1/\sqrt{6}$	$1/\sqrt{8}$	$-1/\sqrt{2}$	$1/\sqrt{8}$	$-1/\sqrt{8}$	$1/\sqrt{2}$	$-1/\sqrt{8}$	$-\sqrt{3}/2$	$\sqrt{3}/2$	0	$\sqrt{3}/2$	$-\sqrt{3}/2$	0
p_y	$1/\sqrt{2}$	0	$-1/\sqrt{2}$	$-1/\sqrt{2}$	0	$1/\sqrt{2}$	$\sqrt{3/8}$	0	$-\sqrt{3/8}$	$-\sqrt{3/8}$	0	$\sqrt{3/8}$	$-1/2$	$-1/2$	1	$1/2$	$1/2$	-1

Tab. D.1: Overlap between two sets of basis.

D.2 β-graphyne

Similarly, for β-graphyne we find

$$
\begin{aligned}
H_L^{z,\sigma} = i\xi_{p2} \sum_i \Big[& A_i^\dagger(2^{-1/2}\sigma_x + 6^{-1/2}\sigma_y)A_{1,i} + A_i^\dagger(-(2/3)^{1/2}\sigma_y)A_{2,i} + A_i^\dagger(-2^{-1/2}\sigma_x + 6^{-1/2}\sigma_y)A_{3,i} \\
& + B_i^\dagger(-2^{-1/2}\sigma_x - 6^{-1/2}\sigma_y)B_{1,i} + B_i^\dagger((2/3)^{1/2}\sigma_y)B_{2,i} + B_i^\dagger(2^{-1/2}\sigma_x - 6^{-1/2}\sigma_y)B_{3,i} \\
& + C_i^\dagger(2^{-1/2}\sigma_x + 6^{-1/2}\sigma_y)C_{1,i} + C_i^\dagger(-(2/3)^{1/2}\sigma_y)C_{2,i} + C_i^\dagger(-2^{-1/2}\sigma_x + 6^{-1/2}\sigma_y)C_{3,i} \\
& + D_i^\dagger(-2^{-1/2}\sigma_x - 6^{-1/2}\sigma_y)D_{1,i} + D_i^\dagger((2/3)^{1/2}\sigma_y)D_{2,i} + D_i^\dagger(2^{-1/2}\sigma_x - 6^{-1/2}\sigma_y)D_{3,i} \\
& + E_i^\dagger(2^{-1/2}\sigma_x + 6^{-1/2}\sigma_y)E_{1,i} + E_i^\dagger(-(2/3)^{1/2}\sigma_y)E_{2,i} + E_i^\dagger(-2^{-1/2}\sigma_x + 6^{-1/2}\sigma_y)E_{3,i} \\
& + F_i^\dagger(-2^{-1/2}\sigma_x - 6^{-1/2}\sigma_y)F_{1,i} + F_i^\dagger((2/3)^{1/2}\sigma_y)F_{2,i} + F_i^\dagger(2^{-1/2}\sigma_x - 6^{-1/2}\sigma_y)F_{3,i} \Big] \\
+ i\xi_{p1} \sum_i \Big[& (a_i^1)^\dagger(-2^{-1/2}\sigma_y)a_{1,i}^1 + (a_i^1)^\dagger(2^{-1/2}\sigma_y)a_{2,i}^1 + (a_i^1)^\dagger(\sigma_x)a_{3,i}^1 + (a_i^2)^\dagger 2^{-1/2}(-\sqrt{3}\sigma_x/2 \\
& - \sigma_y/2)a_{1,i}^2 + (a_i^2)^\dagger(\sigma_x/2 - \sqrt{3}\sigma_y/2)a_{2,i}^2 + (a_i^2)^\dagger 2^{-1/2}(\sqrt{3}\sigma_x/2 + \sigma_y/2)a_{3,i}^2 + (b_i^1)^\dagger 2^{-1/2}\sigma_y b_{1,i}^1 \\
& - (b_i^1)^\dagger 2^{-1/2}\sigma_y b_{2,i}^1 + (b_i^1)^\dagger \sigma_x b_{3,i}^1 + (b_i^2)^\dagger(\sigma_x/2 + \sqrt{3}\sigma_y/2)b_{1,i}^2 + (b_i^2)^\dagger 2^{-1/2}(\sqrt{3}\sigma_x/2 - \sigma_y/2)b_{2,i}^2 \\
& - (b_i^2)^\dagger 2^{-1/2}(\sqrt{3}\sigma_x/2 - \sigma_y/2)b_{3,i}^2 + (c_i^2)^\dagger(\sigma_x/2 + \sqrt{3}\sigma_y/2)c_{1,i}^2 - (c_i^2)^\dagger 2^{-1/2}(\sqrt{3}\sigma_x/2 - \sigma_y/2)c_{2,i}^2 \\
& + (c_i^2)^\dagger 2^{-1/2}(\sqrt{3}\sigma_x/2 - \sigma_y/2)c_{3,i}^2 + (c_i^1)^\dagger 2^{-1/2}(-\sqrt{3}\sigma_x/2 - \sigma_y/2)c_{1,i}^1 - (c_i^1)^\dagger(\sigma_x/2 - \sqrt{3}\sigma_y/2)c_{2,i}^1 \\
& + (c_i^1)^\dagger 2^{-1/2}(\sqrt{3}\sigma_x/2 + \sigma_y/2)c_{3,i}^1 - (d_i^1)^\dagger 2^{-1/2}(-\sqrt{3}\sigma_x/2 - \sigma_y/2)d_{1,i}^1 - (d_i^1)^\dagger(\sigma_x/2 - \sqrt{3}\sigma_y/2)d_{2,i}^1 \\
& - (d_i^1)^\dagger 2^{-1/2}(\sqrt{3}\sigma_x/2 + \sigma_y/2)d_{3,i}^1 - (d_i^2)^\dagger(-2^{-1/2}\sigma_y)d_{1,i}^2 - (d_i^2)^\dagger(2^{-1/2}\sigma_y)d_{2,i}^2 - (d_i^2)^\dagger(\sigma_x)d_{3,i}^2 \\
& - (e_i^1)^\dagger(\sigma_x/2 + \sqrt{3}\sigma_y/2)e_{1,i}^1 - (e_i^1)^\dagger 2^{-1/2}(\sqrt{3}\sigma_x/2 - \sigma_y/2)e_{2,i}^1 + (e_i^1)^\dagger 2^{-1/2}(\sqrt{3}\sigma_x/2 - \sigma_y/2)e_{3,i}^1 \\
& - (e_i^2)^\dagger 2^{-1/2}\sigma_y e_{1,i}^2 + (e_i^2)^\dagger 2^{-1/2}\sigma_y e_{2,i}^2 - (e_i^2)^\dagger \sigma_x e_{3,i}^2 \\
& - (f_i^1)^\dagger(\sigma_x/2 + \sqrt{3}\sigma_y/2)f_{1,i}^1 + (f_i^1)^\dagger 2^{-1/2}(\sqrt{3}\sigma_x/2 - \sigma_y/2)f_{2,i}^1 - (f_i^1)^\dagger 2^{-1/2}(\sqrt{3}\sigma_x/2 - \sigma_y/2)f_{3,i}^1 \\
& (f_i^2)^\dagger 2^{-1/2}(\sqrt{3}\sigma_x/2 + \sigma_y/2)f_{1,i}^2 + (f_i^2)^\dagger(\sigma_x/2 - \sqrt{3}\sigma_y/2)f_{2,i}^2 - (f_i^2)^\dagger 2^{-1/2}(\sqrt{3}\sigma_x/2 + \sigma_y/2)f_{3,i}^2 \Big],
\end{aligned}
\tag{D.3}
$$

and

$$
\begin{aligned}
H_E^{z,\sigma} = \xi_{sp2} 3^{-1/2} \sum_i \Big[& A_i^\dagger(A_{1,i} + A_{2,i} + A_{3,i}) + B_i^\dagger(B_{1,i} + B_{2,i} + B_{3,i}) + C_i^\dagger(C_{1,i} + C_{2,i} + C_{3,i}) + D_i^\dagger(D_{1,i} + D_{2,i} \\
& + D_{3,i}) + E_i^\dagger(E_{1,i} + E_{2,i} + E_{3,i}) + F_i^\dagger(F_{1,i} + F_{2,i} + F_{3,i}) \Big] + \xi_{sp1} 2^{-1/2} \sum_i \Big[(a_i^1)^\dagger(a_{2,i}^1 + a_{1,i}^1) + (a_i^2)^\dagger(a_{1,i}^2 \\
& + a_{3,i}^2) + (b_i^1)^\dagger(b_{2,i}^1 + b_{1,i}^1) + (b_i^2)^\dagger(b_{2,i}^2 + b_{3,i}^2) + (c_i^1)^\dagger(c_{1,i}^1 + c_{3,i}^1) + (c_i^2)^\dagger(c_{2,i}^2 + c_{3,i}^2) + (d_i^1)^\dagger(d_{1,i}^1 + d_{3,i}^1) \\
& + (d_i^2)^\dagger(d_{1,i}^2 + d_{2,i}^2) + (e_i^1)^\dagger(e_{3,i}^1 + e_{2,i}^1) + (e_i^2)^\dagger(e_{1,i}^2 + e_{2,i}^2) + (f_i^1)^\dagger(f_{2,i}^1 + f_{3,i}^1) + (f_i^2)^\dagger(f_{1,i}^2 + f_{3,i}^2) \Big].
\end{aligned}
\tag{D.4}
$$

D.3 γ-graphyne

The SOC Hamiltonians for γ-graphyne are given by

$$
\begin{aligned}
H_L^{z,\sigma} = i\xi_{p2} \sum_i \big[& A_i^\dagger(2^{-1/2}\sigma_x + 6^{-1/2}\sigma_y)A_{1,i} + A_i^\dagger(-(2/3)^{1/2}\sigma_y)A_{2,i} + A_i^\dagger(-2^{-1/2}\sigma_x + 6^{-1/2}\sigma_y)A_{3,i} \\
& + B_i^\dagger(-2^{-1/2}\sigma_x - 6^{-1/2}\sigma_y)B_{1,i} + B_i^\dagger((2/3)^{1/2}\sigma_y)B_{2,i} + B_i^\dagger(2^{-1/2}\sigma_x - 6^{-1/2}\sigma_y)B_{3,i} \\
& + C_i^\dagger(2^{-1/2}\sigma_x + 6^{-1/2}\sigma_y)C_{1,i} + C_i^\dagger(-(2/3)^{1/2}\sigma_y)C_{2,i} + C_i^\dagger(-2^{-1/2}\sigma_x + 6^{-1/2}\sigma_y)C_{3,i} \\
& + D_i^\dagger(-2^{-1/2}\sigma_x - 6^{-1/2}\sigma_y)D_{1,i} + D_i^\dagger((2/3)^{1/2}\sigma_y)D_{2,i} + D_i^\dagger(2^{-1/2}\sigma_x - 6^{-1/2}\sigma_y)D_{3,i} \\
& + E_i^\dagger(2^{-1/2}\sigma_x + 6^{-1/2}\sigma_y)E_{1,i} + E_i^\dagger(-(2/3)^{1/2}\sigma_y)E_{2,i} + E_i^\dagger(-2^{-1/2}\sigma_x + 6^{-1/2}\sigma_y)E_{3,i} \\
& + F_i^\dagger(-2^{-1/2}\sigma_x - 6^{-1/2}\sigma_y)F_{1,i} + F_i^\dagger((2/3)^{1/2}\sigma_y)F_{2,i} + F_i^\dagger(2^{-1/2}\sigma_x - 6^{-1/2}\sigma_y)F_{3,i} \big] \\
+ i\xi_{p1} \sum_i \big[& a_i^\dagger(-\sigma_x/2 - \sqrt{3}\sigma_y/2)a_{1,i} + a_i^\dagger 2^{-1/2}(-\sqrt{3}\sigma_x/2 + \sigma_y/2)a_{2,i} + a_i^\dagger 2^{-1/2}(\sqrt{3}\sigma_x/2 - \sigma_y/2)a_{3,i} \\
& + b_i^\dagger 2^{-1/2}(\sqrt{3}\sigma_x/2 + \sigma_y/2)b_{1,i} + b_i^\dagger(-\sigma_x/2 + \sqrt{3}\sigma_y/2)b_{2,i} + b_i^\dagger 2^{-1/2}(-\sqrt{3}\sigma_x/2 - \sigma_y/2)b_{3,i} \\
& - c_i^\dagger 2^{-1/2}\sigma_y c_{1,i} + c_i^\dagger 2^{-1/2}\sigma_y c_{2,i} + c_i^\dagger \sigma_x c_{3,i} \\
& + d_i^\dagger(-\sigma_x/2 - \sqrt{3}\sigma_y/2)d_{1,i} + d_i^\dagger 2^{-1/2}(\sqrt{3}\sigma_x/2 - \sigma_y/2)d_{2,i} + d_i^\dagger 2^{-1/2}(-\sqrt{3}\sigma_x/2 + \sigma_y/2)d_{3,i} \\
& + e_i^\dagger 2^{-1/2}(-\sqrt{3}\sigma_x/2 - \sigma_y/2)e_{1,i} + e_i^\dagger(-\sigma_x/2 + \sqrt{3}\sigma_y/2)e_{2,i} + e_i^\dagger 2^{-1/2}(\sqrt{3}\sigma_x/2 + \sigma_y/2)b_{3,i} \\
& + f_i^\dagger 2^{-1/2}\sigma_y f_{1,i} - f_i^\dagger 2^{-1/2}\sigma_y f_{2,i} + f_i^\dagger \sigma_x f_{3,i} \big],
\end{aligned}
\tag{D.5}
$$

and

$$
\begin{aligned}
H_E^{z,\sigma} = \xi_{sp2}3^{-1/2} \sum_i \big[& A_i^\dagger(A_{1,i} + A_{2,i} + A_{3,i}) + B_i^\dagger(B_{1,i} + B_{2,i} + B_{3,i}) + C_i^\dagger(C_{1,i} + C_{2,i} + C_{3,i}) + D_i^\dagger(D_{1,i} + D_{2,i} \\
& + D_{3,i}) + E_i^\dagger(E_{1,i} + E_{2,i} + E_{3,i}) + F_i^\dagger(F_{1,i} + F_{2,i} + F_{3,i}) \big] + \xi_{sp1}2^{-1/2} \sum_i \big[a_i^\dagger(a_{2,i} + a_{3,i}) + b_i^\dagger(b_{1,i} + b_{3,i}) \\
& c_i^\dagger(c_{1,i} + c_{2,i}) + d_i(d_{2,i} + d_{3,i}) + e_i(e_{1,i} + e_{3,i}) + f_i(f_{1,i} + f_{2,i}) \big].
\end{aligned}
\tag{D.6}
$$

E. CALCULATION OF CHERN NUMBERS

The Chern numbers C_n that have been calculated are defined as

$$C_n := \frac{1}{2\pi i} \int_{BZ} d^2k \, F_{12}(k), \tag{E.1}$$

where $F_{12}(k)$ is the Berry curvature

$$F_{12}(k) := \partial_1 A_2(k) - \partial_2 A_1(k),$$
$$A_\mu(k) := \langle n(k)|\partial_\mu|n(k)\rangle. \tag{E.2}$$

Here, $|n(k)\rangle$ is a normalized Bloch state belonging to the nth band and $A_\mu(k)$ is the Berry connection. Note that we are implicitly assuming that the nth band is gapped, otherwise this is not a sound definition. The most elementary way to compute this number is by replacing the integral by a summation and the derivative by some discrete differences. This procedure could be cumbersome, hence we us an alternative way of computing the Chern numbers based on lattice gauge theory [36]. First of all, we assume that the BZ is discretized by a set of lattice points $k_l = (k_{l,x}, k_{l,y})$ that are equally spaced, with spacing a. On this discrete set of points, we define a $U(1)$ link variable

$$U_\mu(k_l) := \frac{\langle n(k_l)|n(k_l + \hat{\mu})\rangle}{|\langle n(k_l)|n(k_l + \hat{\mu})\rangle|} \tag{E.3}$$

where $\hat{\mu}$ is defined as the vector pointing in the direction μ with magnitude a. Next, we define the lattice field strength $\tilde{F}_{12}(k_l)$ as

$$\tilde{F}_{12}(k_l) := \log\left[U_1(k_l)U_2(k_l + \hat{1})U_1^{-1}(k_l + \hat{2})U_2^{-1}(k_l)\right]. \tag{E.4}$$

Finally, we define the lattice Chern number as

$$\tilde{C}_n := \frac{1}{2\pi i} \sum_{k_l \in BZ} \tilde{F}_{12}(k_l). \tag{E.5}$$

It still remains to be shown that upon taking the limit $a \to 0$ we find $\tilde{C}_n = C_n$. One can easily prove that the lattice field strength is a gauge invariant quantity. As a result, we may simply assume that the normalized state $|n(k)\rangle$ varies smoothly through the BZ. Suppose now that the lattice spacing $a \ll 1$. Then, we find

$$
\begin{aligned}
\tilde{F}_{12}(k) &= \log\left[U_1(k)U_2(k + \hat{1})U_1^{-1}(k + \hat{2})U_2^{-1}(k)\right] \\
&\approx \log\left\{U_1(k)\left[U_2(k) + a\partial_1 U_2(k)\right]U_1^{-1}(k)\left[1 - aU_1^{-1}(k)\partial_2 U_1(k)\right]U_2^{-1}(k)\right\} \\
&\approx \log\left[(1 + aU_2^{-1}(k)\partial_1 U_2(k) - aU_1^{-1}(k)\partial_2 U_1(k)) + O(a^2)\right] \\
&\approx aU_2^{-1}(k)\partial_1 U_2(k) - aU_1^{-1}(k)\partial_2 U_1(k) \\
&\approx \frac{U_2(k + \hat{1}) - U_2(k)}{U_2(k)} - 1 \leftrightarrow 2 \\
&\approx \left[\frac{\langle n(k + \hat{1})|n(k + \hat{1} + \hat{2})\rangle}{1 + O(a)} - \frac{\langle n(k)|n(k + \hat{2})\rangle}{1 + O(a)}\right](1 + O(a)) - 1 \leftrightarrow 2
\end{aligned} \tag{E.6}
$$

In the fifth line, we used $|\langle n(k)|n(k+\hat{\mu})\rangle| = 1 + O(a)$, as follows from the normalization. Moreover, we used $1/U_2(k) \approx 1 + O(a)$, this follows from the fact that for $a = 0$ we obtain $U_\mu(k) = 1$. On the other hand, we find

$$
\begin{aligned}
F_{12}(k) &\approx \frac{A_2(k+\hat{1}) - A_2(k)}{a} - 1 \leftrightarrow 2 \\
&\approx \frac{\langle n(k+\hat{1})|n(k+\hat{1}+\hat{2})\rangle - \langle n(k+\hat{1})|n(k+\hat{1})\rangle}{a^2} - \frac{\langle n(k)|n(k+\hat{2})\rangle - \langle n(k)|n(k)\rangle}{a^2} - 1 \leftrightarrow 2 \\
&\approx \frac{\langle n(k+\hat{1})|n(k+\hat{1}+\hat{2})\rangle - \langle n(k)|n(k+\hat{2})\rangle}{a^2} - 1 \leftrightarrow 2
\end{aligned}
$$

Hence, $\tilde{F}_{12}(k) \approx F_{12}(k)a^2$. Plugging this into Eq. (E.5), we find

$$
\begin{aligned}
\tilde{C}_n &= \sum_{k_l \in BZ} \tilde{F}_{12}(k_l) \\
&= \sum_{k_l \in BZ} F_{12}(k_l)a^2(1 + O(a))
\end{aligned}
\tag{E.7}
$$

The integral in Eq. (E.1) may be written as a Riemann sum, $C_n = \lim_{a\to 0} \sum_{k_l \in BZ} a^2 F_{12}(k_l)/(2\pi i)$. We then find $C_n = \tilde{C}_n$ upon taking the limit $a \to 0$. By using this method, we have obtained the Chern numbers, as shown in the main text (see also Fig. 3 therein).

BIBLIOGRAPHY

[1] A. H. Castro Neto, F, Guinea, N. M. R. Peres, K. S. Novoselov, and A. K. Geim, Rev. mod. Phys **81**, 109 (2009).

[2] C. L. Kane and E.J. Mele, Phys. Rev. Lett. **95**, 146802 (2005).

[3] E. Kalesaki, C. Delerue, C. Morais Smith, W. Beugeling, G. Allan, and D. Vanmaekelbergh, Phys. Rev. X **4**, 011010 (2014).

[4] M. Gibertini, A. Singha, V. Pellegrini, M. Polini, G. Vignale, A. Pinczuk, L. N. Pfeiffer, and K.W. West, Phys. Rev. B **79**, 241406 (2009).

[5] K. K. Gomes, W. Mar, W. Ko, F. Guinea, and H. C. Manoharan, Nature (London) **483**, 306 (2012).

[6] R. H. Baughman, H. Eckhardt, M. Kertesz, J. Chem. Phys. **87**, 6687 (1987).

[7] N. Narita, S. Nagai, S. Suzuki, and K. Nakao, Phys. Rev. B **58**, 11009 (1998).

[8] K. Tahara, T. Yoshimura, M. Sonoda, Y. Tobe, and R. V. Williams, J. Org. Chem. **72**, 1437 (2007).

[9] J Kang, J. Li, F. Wu, S.-S. Li, and J.-B. Xia, J. Phys. Chem. C **115**, 20466 (2011).

[10] Q. Yue, S. Chang, J. Kang, J. Tan, S. Qin, and J. Li, J. Chem. Phys. **136**, 244702 (2012).

[11] S. W. Cranford and M. J. Buehler, Carbon **49**, 4111 (2011).

[12] G. X. Li, Y. L. Li, H. B. Liu, Y. B. Guo, Y. J. Li, and D. B. Zhu , Chem. Commun. **46**, 3256 (2010).

[13] D. Malko, C. Neiss, F. Vines, and A. Görling, Phys. Rev. Lett. **108**, 086804 (2012).

[14] H. Huang, W. Duan, and Z. Liu, New. J. Phys. **15**, 023004 (2013).

[15] J.-J. Zheng, X. Zhao, Y. Zhao, and X. Gao, Sci. Reports **3**, 1271 (2013).

[16] B. G. Kim and H. J. Choi, Phys. Rev. B **86**, 115435 (2012).

[17] J.-J Zheng, X. Zhao, S. B. Zhang, and X. Gao, J. Chem. Phys. **138**, 244708 (2013).

[18] H. Zhang , M. Zhao, X. He , Z. Wang , X. Zhang , and X. Liu, J. Phys. Chem. C **115**, 8845 (2011).

[19] H. J. Hwang , Y. Kwon , and H. Lee, J. Phys. Chem. C **115**, 8845 (2011).

[20] J. He, S. Y. Ma, P. Zhou, C. X. Zhang, C. He, and L. Z. Sun, J. Phys. Chem. C **116**, 26313 (2012).

[21] Y. Li, L. Xu, H. Liu, and Y. Li, Chem. Soc. Rev. **43**, 2527 (2014).

[22] H. Min, J. E. Hill, N. A. Sinitsyn, B. R. Sahu, L. Kleinman, and A. H. MacDonald, Phys. Rev. B **74**, 165310 (2006).

[23] S. Konschuh, M. Gmitra, and J. Fabian, Phys. Rev. B **82**, 245412 (2010).

[24] A. Messiah, *Quantum Mechanics*, (North-Holland, Amsterdam, 1965), Vol. 2.

[25] I. Herbut, V. Juričić, and B. Roy, Phys. Rev. B **79**, 085116 (2009).

[26] G.W. Semenoff, Phys. Rev. Lett. **53**, 2449 (1984).

[27] F.D.M. Haldane, Phys. Rev. Lett. **61**, 2015 (1988).

[28] D.J. Thouless, M. Kohmoto, M.P. Nightingale, and M. den Nijs, Phys. Rev. Lett. **49**, 205 (1982).

[29] M. König, S. Wiedmann, C. Brüne, A. Roth, H. Buhmann, L. Molenkamp, X.-L. Qi, and S.-C. Zhang, Science **318**, 766 (2007).

[30] W. Beugeling, Ph.D. Thesis, Utrecht University, 2012.

[31] Z. Liu, G. Yu, H. Yao, L. Liu, L. Jiang, and Y. Zheng, New. J. Phys. **14**, 113007 (2012).

[32] J.J. Sakurai, *Modern Quantum Mechanics*, 2nd ed. (Addison Wesley, Reading, MA, 2010).

[33] M. Zhao, W. Dong, and A. Wang, Sci. Reports **3**, 3532 (2013).

[34] M. Zarea and N. Sandler, Phys. Rev. B **79**, 165442 (2009).

[35] R. van Gelderen and C. Morais Smith, Phys. Rev. B **81**, 125435 (2010).

[36] T. Fukui, Y. Hatsugai, and H. Suzuki, J. Phys. Soc. Jpn. **74**, 1674 (2005).